Optimization of MR Sensor Geometry Towards Picotesla Detection

Ricardo André Duarte Varela

Thesis to obtain the Master of Science Degree in

Engineering Physics

Supervisor: Prof. Susana Isabel Pinheiro Cardoso de Freitas

Examination Committee

Chairperson: Prof. Pedro Miguel Felix Brogueira
Supervisor: Prof. Susana Isabel Pinheiro Cardoso de Freitas
Member of the Committee: Dr. Ricardo Alexandre de Matos Antunes Ferreira

November 2015

"As armas e os Barões assinalados
Que da Ocidental praia Lusitana
Por mares nunca de antes navegados
Passaram ainda além da Taprobana,
Em perigos e guerras esforçados
Mais do que prometia a força humana,
E entre gente remota edificaram
Novo Reino, que tanto sublimaram;

E também as memórias gloriosas
Daqueles Reis que foram dilatando
A Fé, o Império, e as terras viciosas
De África e de Ásia andaram devastando,
E aqueles que por obras valerosas
Se vão da lei da Morte libertando,
Cantando espalharei por toda parte,
Se a tanto me ajudar o engenho e arte.

Cessem do sábio Grego e do Troiano
As navegações grandes que fizeram;
Cale-se de Alexandro e de Trajano
A fama das vitórias que tiveram;
Que eu canto o peito ilustre Lusitano,
A quem Neptuno e Marte obedeceram.
Cesse tudo o que a Musa antiga canta,
Que outro valor mais alto se alevanta."

Luís de Camões, Os Lusíadas (I, 1-3)

Acknowledgments

First for all, I would like to thank professor Susana Freitas for the amazing opportunity to work in this promising technique, using the INESC-MN facilities, and also for all the learning and mentorship that allowed me to accomplish this work and develop my engineer side.

To professor Luís Melo, from Instituto Superior Técnico, for his assistance in the AFM measurements performed in this work.

To Ana Silva and Diana Leitão, for all the help in all kind of problems, great advising, and solving my (many) doubts, a special ”thank you”.

To Natércia, whose amazing (permanent) good humour is truly contagious, helping in the good days and, more important, in the bad ones, thank you.

I thank INESC-MN process engineers, Fernando Silva, José Bernardo, and Virginia Soares, for the help on the clean room and teaching me how to use several machines.

To my dear INESC-MN colleagues, Ana Rita Soares, Anastasiia Moskaltsova, Andreia Barroso, Bernardo Pires, Carla Duarte, Fernando Franco, Filipe Cardoso, Gabriel Farinha, Joana Santos, João Valadeiro, Marília Silva, Miguel Neto, Raju Kumar, Sara Cardoso, Simon Knudde, and Tiago Monteiro, thank you all for the amazing environment, help and support!

A special thank to Gabriel Farinha, Andreia Barroso and Bernardo Pires, my partners in this battle (thesis!). Having someone passing by the same obstacles and problems helps to solve them and motivates to continue. Also, Miguel Neto, for all the advising and teaching, specially in the beginning, when the work and uncertainty are overwhelming, and of course for the ”philosophical friday afternoons”. To Rita Macedo, which, although only arrived in the last month of my work, was amazingly heedful and a great support in the hardest final moments of this thesis. Finally, to Sara Cardoso my dear desk friend (and amazing soccer player) for all the help during my work and review of this thesis.

To my dear physics friends, Andreia, Bárbara, Henrique, Lopes, Pedro, Zé, because more important than all the support during my work is, undoubtedly, the awesome five years that we passed together, a special ”Thank you!”.

Also, to Miguel and Sara, for the amazing dinners, friday nights, pool parties, and much much more, I thank you a lot!

Finally, but certainly not less important, I thank, from the bottom of my heart, to my mother, which, with its amazing effort, provided me the opportunity to accomplish this master course; also to my sister and brother-in-law for all the support in my life and to always believe in me!

Resumo

Actualmente, as *spinvalve* são um dos sensores magnetoresistivos mais utilizados. A lista de aplicações é extensa, abrangendo várias áreas científicas, sendo demarcada pelos limites de detecção destes sensores. As técnicas mais eficientes, que permitem melhorar esta característica, requerem a utilização de estruturas com áreas extensas.

O trabalho presente nesta tese destina-se a estudar uma nova técnica, que permite melhorar a detectividade destes sensores magnetoresistivos, sem requerer maiores áreas que as do próprio sensor. Esta técnica baseia-se na utilização de *spinvalves* conectadas em paralelo através de empacotamento vertical, invés da actual conexão paralela no plano, que envolve o aumento da área ocupada. As medições do ruído demonstram uma redução do ruído térmico com o número de *spinvalves* empacotadas M, em função de $1/\sqrt{M}$, tal como esperado teoricamente. Contudo, para o ruído 1/f, esta dependência não foi observada, tendo sido encontrada uma relação entre este ruído e a estabilidade magnética dos momentos magnéticos.

Os sistemas de *spinvalves* empacotadas revelaram ainda redução da sensibilidade, o que indica que existem acoplamentos magnéticos entre estas spinvalves, afectando negativamente a sua detectividade. Ainda assim, foram observadas melhorias na detectividade, visto que um sistema composto por quatro *spinvalves* empacotadas apresentou melhores níveis de detectividade, especificamente $7.6\,\mathrm{nT}/\sqrt{\mathrm{Hz}}$ a $30\,\mathrm{Hz}$ ($4.4\,\mathrm{nT}/\sqrt{\mathrm{Hz}}$ a $100\,\mathrm{Hz}$), comparativamente com os valores de detectividade obtidos para uma *spinvalve* individual, $12.3\,\mathrm{nT}/\sqrt{\mathrm{Hz}}$ a $30\,\mathrm{Hz}$ ($7.6\,\mathrm{nT}/\sqrt{\mathrm{Hz}}$ a $100\,\mathrm{Hz}$).

Esta influência foi investigada e, com base nas conclusões retiradas, são evidenciadas ideias para um futuro desenvolvimento desta técnica.

Palavras-chave: Spinvalve, ruído, detectividade, empacotamento

Abstract

Spinvalves are one of the most used magnetoresistive sensors nowadays. The range of applications is countless and is only limited by the detectivity performance of these sensors. The most efficient techniques, to improve sensors' detectivity, comprehend a trade-off between detectivity and the spatial footprint.

The work in this thesis aims to study a new technique, to improve detectivity without the loss in spatial resolution. It is based in the connection of spinvalve sensors in parallel by means of vertical packaging, instead of in-plane parallel connections. The results of the noise measurements demonstrated a reduction of the thermal noise as a function of the number of spinvalves packaged (M) as $1/\sqrt{M}$, as expected. The same dependency was not observed for 1/f noise, instead, a dependency with the magnetic stability of the magnetic moments was obtained.

SV packaged structures revealed loss in sensitivity, when compared with individual SV, indicating magnetic coupling effects between the SV elements, thus, negatively influencing the detectivity. Nevertheless, detectivity improvements were obtained, since packaged structures with four spinvalves presented better detectivity limits, specifically $7.6\,\mathrm{nT}/\sqrt{\mathrm{Hz}}$ at $30\,\mathrm{Hz}$ ($4.4\,\mathrm{nT}/\sqrt{\mathrm{Hz}}$ at $100\,\mathrm{Hz}$), compared to individual spinvalves with detectivity values of $12.3\,\mathrm{nT}/\sqrt{\mathrm{Hz}}$ at $30\,\mathrm{Hz}$ ($7.6\,\mathrm{nT}/\sqrt{\mathrm{Hz}}$ at $100\,\mathrm{Hz}$).

These sensitivity loss was investigated, and, based on that, ideas to future work on this technique are presented.

Keywords: spinvalve, noise, detectivity, packaging

Contents

List of Tables

List of Figures

Nomenclature

AFM - Antiferromagnetic

AP - Antiparallel

CIP - Current in plane

CPP - Current perpendicular to plane

DI - Deionized water

DOS - Density of states

DUT - Device under test

DWL - Direct write laser

D - Sensor detectivity

EA - Easy axis

FM - Ferromagnetic

GMR - Giant magnetoresistance

HA - Hard axis

HDMS - Hexamethyldisilane

H_c - Coercivity field

H_f - Fringe field

H - Magnetic field

IPA - Isopropyl alcohol

MR - Magnetoresistance

MTJ - Magnetic Tunnel Junction

M_r - Remanent magnetization

M_s - Saturation magnetization

M - Magnetization

NM - Non-magnetic

P - Parallel

R - Electrical resistance

SAF - Synthetic antiferromagnetic

SF - Synthetic ferrimagnet

SV - Spinvalve

S - Sensor sensitivity

UHV - Ultra high vaccum

Chapter 1

Introduction

1.1 Motivation

Nanotechnology is an area of recent research that has gained increasing interest due to its promising applications in our everyday lives and also for supporting the development of many other scientific fields. Among many other things, nanotechnology allows the creation of sensors, namely magnetoresistive (MR) sensors, which are used in a wide range of applications such as bacteria detection [1], hard drive read heads [2], magnetoresistive RAM [3], study and cure of certain diseases like cancer [4], DNA sequencing [5], and monitor and study some organs, with great emphasis on the brain [6].

Magnetoresistive sensors use the magnetoresistance characteristic of materials to sense and, consequently, measure magnetic fields. Magnetoresistance is described as the change in the resistance of a magnetic material by an applied magnetic field. There exist several sources for magnetoresistance, which originate different magnetoresistive sensors. Spinvalves (SV) and magnetic tunnel junctions (MTJ) are the most used magnetoresistive sensors nowadays [7]. Although the operation mechanism is based in the relative orientation of their ferromagnetic layers, the physical principle is different, thus, promoting different characteristics. Spinvalve are based in the scattering dependence on magnetization orientation, while MTJs are based on the spin-dependent tunnelling effect through an oxide barrier[8]. MTJs show higher sensitivity than spinvalves. However, the high noise levels of MTJs at low frequencies negatively influence the detectivity limits, which promotes SVs has reliable sensors [9].

Some important applications, such as the study of the human brain using magnetoencephalography (MEG), demand for high spatial resolutions and high detectivity levels (in the order of few fT) at low frequencies ($<10\,\mathrm{Hz}$), meaning high sensitivity capabilities and low noise characteristics on these sensors. Therefore, extended research is performed to improve these characteristics by means of: stack development [10–14], meander structures [15, 16], microelectromechanical systems (MEMS) integration [17–20], magnetic flux guides (MFG) [13, 21–23], and circuit configurations, such as sensor arrays or Wheatstone bridges [14, 24, 25]. Some examples of these strategies are represented in figure 1.1.

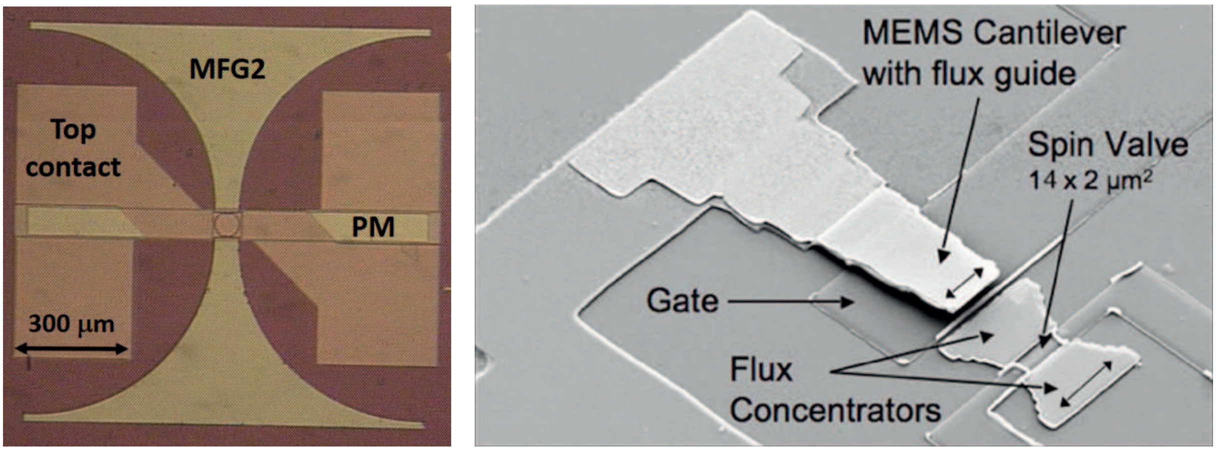

(a) Microscopic view of MFGs [26].

(b) Scanning electron microscopic view of MEMS cantilevers with flux guides on top [18].

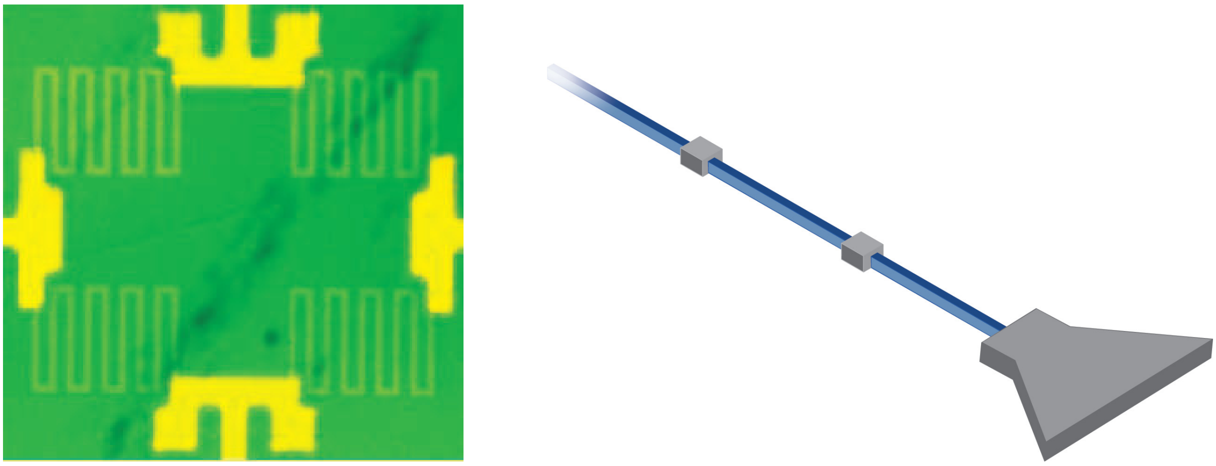

(c) In the left, microscopic view of meander structures in Wheatstone bridge configuration. In the right, meander structure's geometry scheme [15].

(d) Representation of spinvalves connected in series.

Figure 1.1: Examples of approachs used for MR sensors optimization.

1.2 Topic Overview

Noise is an important limitation element for magnetoresistve sensors, influencing the ultimate detectivity. Most application require the measurement of magnetic fields in a low frequency range, at which, the 1/f noise is dominant. Therefore, the detectivity levels for spinvalves in this low frequency range can be described as:

$$D_{SV} = \frac{\Delta H}{MR}\sqrt{\frac{\alpha_{Hooge}}{N_C f}} \tag{1.1}$$

where ΔH defines the linear range of MR sensors, MR the magnetoresistance value, α_{Hooge} is the Hooge constant, N_C is the number of charge carriers, and f is the measured field frequency. These parameters are the focus of the techniques mentioned to improve MR sensor's detectivity.

In 2001, Hitoshi Kanai *et al.* [11] demonstrated the use of nano oxide layers (NOL) to improve the GMR of spinvalves. These layers are placed between the pinned layer and the capping layer or between the free layer and the buffer layer, which confines the scattering process in middle layers where the

GMR effect prevails. These improved stacks demonstrated GMR ratios of 14% [27], a considerable improvement considering the GMR ratios of 8% for conventional SV stacks.

Another important technique consist in the use of magnetic flux guides, which consist in a magnetic structures that concentrates the magnetic field in the sensor's region [20]. Therefore, it promotes an increase in the sensitivity by decreasing the linear range (ΔH).

In 2007, André Guedes *et al.* [21], and, later in 2012, Diana Leitão *et al.* [13] presented the use of MFGs made of an amorphous alloy of CoZrNb, represented in figure 1.1 a), to improve the detectivity of spinvalve sensors. André Guedes showed the improvement of the detectivity limit, at $10\,\mathrm{Hz}$, from $47.4\,\mathrm{nT}/\sqrt{\mathrm{Hz}}$ to $2.2\,\mathrm{nT}/\sqrt{\mathrm{Hz}}$ by incorporating the MFG structure. Similar results were achieved by Diana Leitão, presenting an enhancement of the detectivity, at $10\,\mathrm{Hz}$, from $61.2\,\mathrm{nT}/\sqrt{\mathrm{Hz}}$ to $1.8\,\mathrm{nT}/\sqrt{\mathrm{Hz}}$. The drawback of this approach is the increase of spatial footprint, due to the large dimensions of MFG structures, in the order of $0.1\,\mathrm{mm}^2$.

MEMS technology, represented in figure 1.1 b), creates an ac modulated field from a static magnetic field, thus shifting the signal to be measured to a frequency range with lower noise levels [20]. This is achieved by placing MFGs on top of this MEMS structures actuated by an alternating voltage with a certain frequency f, which causes the cantilever to vibrate at a frequency $2f$, creating an ac field.

In line with the strategy to increase the N_C parameter, one can increase the effective volume of magnetic material of the sensing film. This can be done by increasing the thickness of the film or the sensor area. One approach to increase the sensor's area is arrays of sensors, which has proven to improve the detectivity capabilities of MR sensors.

In 2009, Guerrero *et al.* [28] demonstrated theoretically that series of N magnetic tunnel junction (MTJ) sensors decrease the overall 1/f noise of the system as $1/\sqrt{N}$, however, the thermal noise presents an increase with $\sqrt{N}$. In the same way, M MTJ sensors in parallel configuration was proven to decrease both noise types as $1/\sqrt{M}$. In this thesis, the same analysis is performed for spinvalves' noise, and the same result is achieved.

Since then, several groups [9, 29–40], following this strategy, reported the use of sensors in series or parallel configurations to improve their detectivity capacities. Some of these groups compared the results of the array with the individual sensors.

For example, Kosuke Fujiwara *et al.* [40] presented the use of an array of 100×100 MTJ sensors to reduce the noise spectral density approximately by one order of magnitude, from $10^{-13}\,\mathrm{V}^2/\mathrm{Hz}$ to $10^{-15}\,\mathrm{V}^2/\mathrm{Hz}$ at $10\,\mathrm{Hz}$.

Likewise, José Amaral reports in its work [29], the use of two arrays with 992 (16 in series and 62 in parallel, occupying an area of approximately $1\,\mathrm{mm}^2$) and 6200 (50 in series and 124 in parallel, occupying an area of approximately $5\,\mathrm{mm}^2$) spinvalve (SV) sensors that improved the detectivity limits at $30\,\mathrm{Hz}$ respectively to $3\,\mathrm{nT}/\sqrt{\mathrm{Hz}}$ and $1.3\,\mathrm{nT}/\sqrt{\mathrm{Hz}}$, compared to the detectivity of the individual SV sensor presented as $21\,\mathrm{nT}/\sqrt{\mathrm{Hz}}$, for the same frequency. Still in this work, is presented the use of 952 MTJ sensors in series that reach a detectivity of $0.84\,\mathrm{nT}/\sqrt{\mathrm{Hz}}$, while for a individual sensor it was obtained $1.51\,\mathrm{nT}/\sqrt{\mathrm{Hz}}$.

Filipe Cardoso *et al.* [36] reported the use of MTJ sensor in series, having ensitivity levels improved from $50.8\,\mathrm{mV/mT}$, for 6 MTJ sensors in series, to $84.5\,\mathrm{mV/mT}$, for 10 MTJ sensors.

1.3 Objectives

From the techniques presented in the previous section,the combined use of MFGs and array of sensors present the best detectivity improvements. However, both are based in a trade-off between detectivity enhancement and spatial footprint increase.

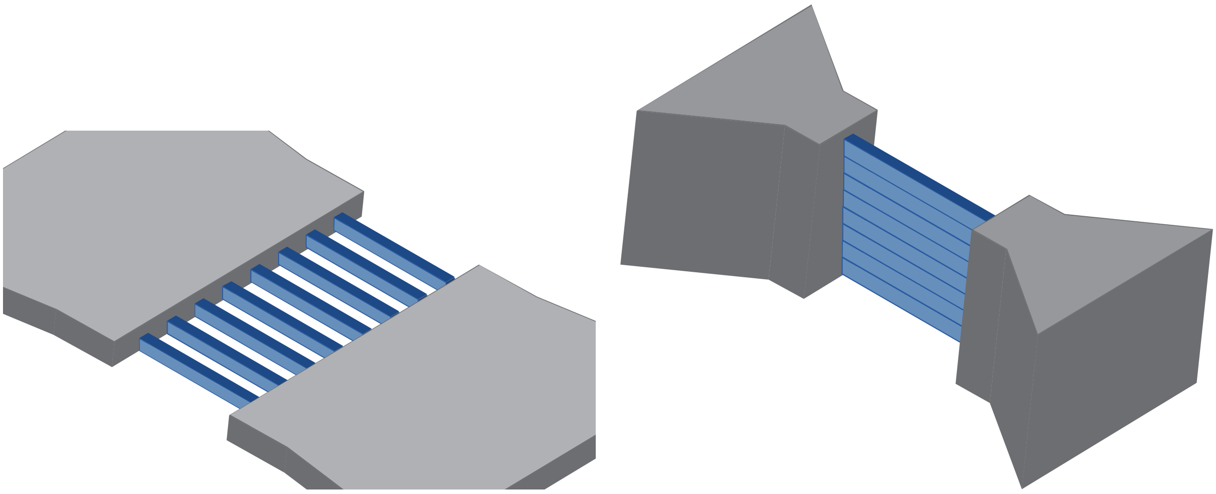

(a) Spinvalves in parallel configuration in-plane.

(b) Spinvalve in parallel configuration by vertical packaging.

Figure 1.2: Representation of two techniques to create spinvalves in parallel configuration. Figure a) represents the configuration used nowadays with the associated increase of spatial footprint. Figure b) represents the novel technique proposed and studied in this thesis.

The work in this thesis aims to take advantage of the parallel configuration strategy by vertical packaging, thus, obtaining spinvalves connected in parallel without the drawback of spatial resolution loss, as illustrated in figure 1.2. Another important advantage of this technique is the fact that, contrarily to in-plane arrays, it can be complemented with the MFGs approach.

In this thesis, the packaged structures are microfabricated and studied in terms of magnetic interaction, electrical contact, and noise and detectivity levels. The magnetic interactions study demands the use of a spacer insulator layer, used to vary the distance between the spinvalves in the package system, which, consequently, requires investigation to obtain the most reliable spacer material. The electrical contact study aims to verify if the metallization process ensures the electrical contact for the package system, which can be problematic considering the decrease in the available contact area. Lastly, with the measurements of the noise and detectivity levels, the performance of different structures can be assessed, and, therefore, validate success of this novel technique.

1.4 Thesis Outline

- **Chapter 2 - Theoretical Background**: In this chapter, the theoretical knowledge obtained and used in the course of this thesis is presented. First, a description of the different types of magnetic materials is performed, along with a explanation about the energy contributions present in a ferromagnetic material. This knowledge will be specially important in the understanding of linearization of a spinvalve sensor. Besides this, a historical and phenomenological explanation of spinvalve sensor is presented. Finally, it is analysed the noise types existent in spinvalves, along with a demonstration of detectivity enhancement using series and parallel arrays of sensors.

- **Chapter 3 - Experimental Methods**: This chapter gathers information about the experimental processes necessary to create the spinvalve sensor in this thesis. Along with each step, the machines used, and the physical process being their operation, are introduced. Moreover, a description of the characterization methods is presented.
- **Chapter 4 - Results**: Here, the experimental results obtained within this thesis are presented and discussed. These results include data from the spacer material studies, the electrical contact examination, and the measurements of the noise and detectivity levels. Finally, a discussion about the sensitivity variation in the packaged system is performed.
- **Chapter 5 - Conclusions**: In this final chapter, an overall discussion about this work is done, with conclusions and considerations on the results and suggestions obtained along with ideas for future work.

Chapter 2

Theoretical Background

2.1 Magnetic Materials

All the materials that exist in nature can be grouped in five different categories:

- **Diamagnetic**
- **Paramagnetic**
- **Ferromagnetic**
- **Ferrimagnetic**
- **Antiferromagnetic**

The magnetism of a material arrives mostly from electron spins and the way they interact with each other. Diamagnetic and paramagnetic materials are characterized by not having long-range interactions and, as consequence, not being magnetically ordered. On the contrary, ferromagnetic, ferrimagnetic, and antiferromagnetic materials are distinguished by having long-range interactions which make them magnetically ordered. However, antiferromagnetic materials tend to align in such a way that their net magnetic moment is approximately zero, so, along with the first two, they are normally referenced as nonmagnetic [41].

2.1.1 Diamagnetism and Paramagnetism

Diamagnetic and paramagnetic materials obey to the expression:

$$M = \chi H, \tag{2.1}$$

where, M and χ are, respectively, the magnetization and susceptibility of the material, and H is the applied field.

Although diamagnetism exists in all materials, it tends to be very weak. It arrives from atoms with all bands full, which means that there are no unpaired electrons and thereupon they are devoid of net

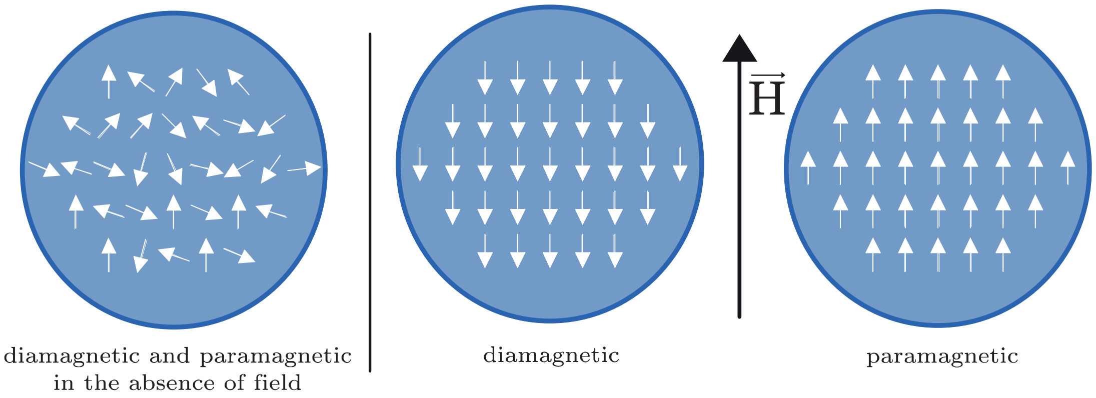

Figure 2.1: Behaviour of diamagnetic and paramagnetic materials in the presence or absence of a magnetic field. Adapted from [7].

magnetic moment. When a magnetic field is applied, a magnetization opposite to the field appears, which is represented as a negative susceptibility.

Paramagnetic materials, contrarily to diamagnetic ones, possess unpaired electrons, which means that some atoms inside these materials carry non-zero magnetic moment, as illustrated in figure 2.1. However, since this atoms don't interact, the random distribution of the atoms induces a null net moment. When a magnetic field is applied, paramagnetic materials tend to partially align with it, which is represented by a positive susceptibility.

2.1.2 Ferromagnetism

As in paramagnetic materials, atoms from ferromagnetic materials reveal unpaired electrons, thus exhibiting non-zero magnetic moment. However, opposite to paramagnetic material, ferromagnetic materials have strong interaction forces, which are a result of electronic exchange forces: a quantum mechanical effect that occurs due to the relative orientation of electrons spins. This interaction promotes parallel alignment between the atoms, producing high net magnetic moment, even in the absence of a magnetic field.

Above a certain temperature, called Curie temperature, the thermal energy surpasses the exchange energy, thus suppressing the interactions between atoms. Hence, it promotes a random configuration that causes a zero net magnetic moment, which means that the material starts behaving has a paramagnetic material.

Another important characteristic of ferromagnetic materials is hysteresis. When a magnetic field is applied to a ferromagnetic material, its atoms tend to align in the field's direction. If enough field is applied, all the atoms align with it, and the magnetization measured in its direction corresponds to the saturation magnetization of the material (M_s).

Nevertheless, when the field is removed, the magnetization does not necessarily returns to the same configuration. This occurs due to the presence of magnetic domains that require energy to be reoriented. Therefore, in the absence of field, the material can have different values of magnetization, called remanent magnetization (M_r), which causes the so called hysteresis loop shown in figure 2.2.

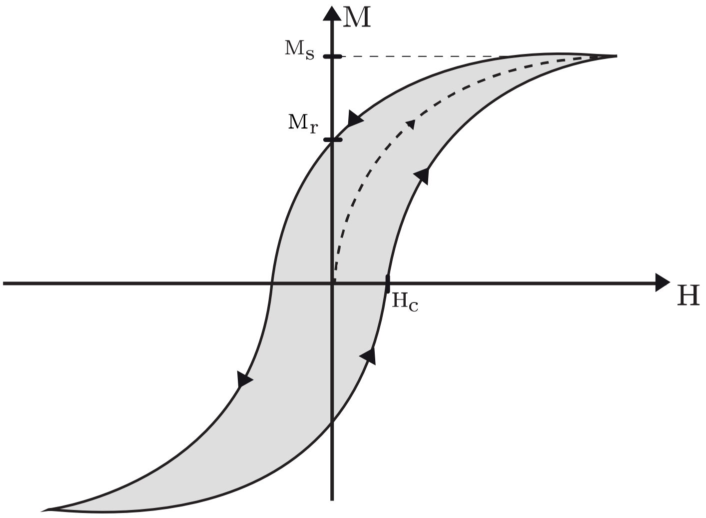

Figure 2.2: Histeresis loop representation. M_s represents the saturation magnetization, M_r the remanent magnetization and H_c the coercivity field.

Finally, the coercivity of a ferromagnetic material is the value of field (H_c) needed so that the magnetization component in that direction becomes zero.

2.1.3 Ferrimagnetism and Antiferromagnetism

As ferromagnetic materials, ferrimagnetic and antiferromagnetic materials are distinguished by their long range interactions between atoms. However, contrarily to ferromagnetic materials, these interactions promote antiparallel alignment. This occurs predominantly in ionic compounds in which the magnetic sublattices tend to acquire this antiparallel state. When the magnetic moment of sublattices is not equal, the net magnetic moment is non-zero, representing a ferrimagnetic material. On the contrary, if lattices' magnetic moment are equal, the net becomes zero and therefore corresponds to an antiferromagnetic material. These characteristics are represented in figure 2.3, where the magnetic moment alignment is illustrated for the three materials.

As ferromagnetic materials, below a certain temperature, called Néel Temperature, antiferromagnetic materials lose their antiparallel alignment, and thus start behaving like paramagnetic materials. Unlike ferromagnetic and ferrimagnetic materials, antiferromagnetic materials don't reveal hysteresis.

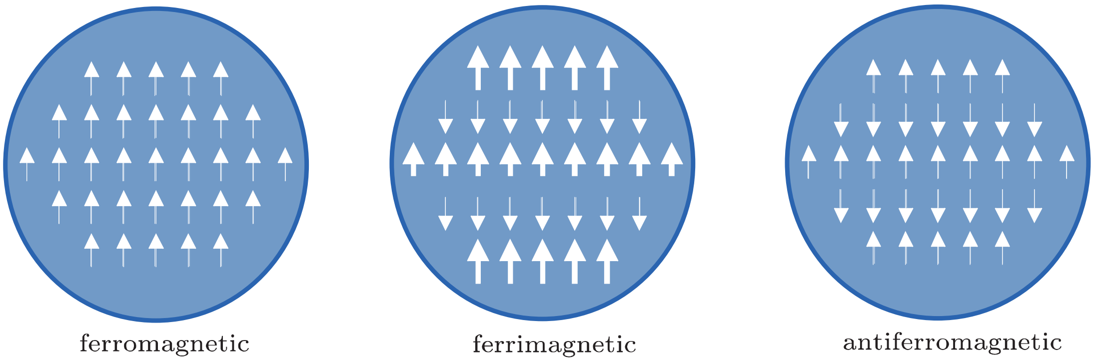

Figure 2.3: Magnetic moment alignment in ferromagnetic, ferrimagnetic and antiferromagnetic materials. Adapted from [7].

2.1.4 Micromagnetism in Ferromagnetic Materials

To study the behavior of spinvalves, is necessary to understand the behaviour of ferromagnetic layers. For this reason, is fundamental to present and analyze more advanced equations, which account for quantum mechanical mechanisms [42, 43].

The first approach is to simplify the ferromagnetic layer by considering it as a single domain with a magnetization equal to the net magnetic moment from all the atoms inside the volume V of the respective layer. This can be described as:

$$M(\mathbf{r}) = \begin{cases} M_s\mathbf{m}(\mathbf{r}) & \text{inside } V \\ 0 & \text{outside } V \end{cases}, \tag{2.2}$$

where M_s is the net magnetic moment magnitude and $\mathbf{m}(\mathbf{r})$ is its direction.

The second strategy consists in describing the energy terms that constitute the system. Since the atoms behave to minimize the total energy of the system, this approach can be used to determine the behaviour of individual ferromagnetic layers and also of composed system as spinvalves, as performed in section 2.2.2. Here, the terms considered are:

- **Zeeman Energy**: represents the effect of the applied magnetic field;
- **Anisotropic Energy**: describes the effect caused by the crystalline anisotropy of the material;
- **Exchange Energy**: defines the effect from the interaction of two dipoles;
- **Demagnetizing Energy**: resulted from the magnetic domains induced in the surfaces of a magnetized layer;
- **Néel Energy**: induced by the roughness in the ferromagnetic interfaces.

Zeeman Energy

Zeeman energy defines the interaction between the applied field and the magnetic moment of the atoms that constitute the ferromagnetic layer. It is the same energy that rotates a compass's needle due to the earth's magnetic field. Therefore, each atom is considered as a magnetic dipole with a magnetic moment (μ). When a magnetic field is applied to this atom, the energy of the system is be given by:

$$E_{atom} = -\boldsymbol{\mu}.\mathbf{H_a} = -\mu H_a \cos(\theta), \tag{2.3}$$

where $\mathbf{H_a}$ is the vector of the magnetic field applied and θ the angle between the magnetization of the atom and the direction of the applied field. It can be seen immediately that the energy is minimized when the moment of the atom is parallel to the applied field.

To get the total energy of the layer, it is necessary to determine the contribution of all the N atoms and thus:

$$E_{Zeeman} = -\sum_{i=1}^{N} e_{atom_i} = -\sum_{i=1}^{N} \boldsymbol{\mu_i}.\mathbf{H_a}. \tag{2.4}$$

Also, considering a large number of atoms ($N \to \infty$) inside a volume V, the continuum definition is expressed by:

$$E_{Zeeman} = -\int_V e_{atom} dV = -\mu_0 \int_V \mathbf{M}.\mathbf{H_a} dV. \tag{2.5}$$

Exchange Energy

As mentioned in section 2.1, the difference between, for example, paramagnetic and ferromagnetic materials is the interaction between their atoms. The atoms of paramagnetic materials have weak exchange interaction contrarily to ferromagnetic and antiferromagnetic materials, for which this interaction is much larger. The exchange interaction implies an exchange energy between the two atoms given by:

$$e_{exchange} = J_{ex_{ij}} \mathbf{S_i}.\mathbf{S_j}, \tag{2.6}$$

where $\mathbf{S_i}$ and $\mathbf{S_j}$ represent the spins of the atoms pair considered and J_{ex_i} is the exchange integral between the wave functions of atoms i and j, which can be assumed constant inside the material. This parameter is positive for ferromagnetic materials, which represents their parallel alignment propensity, and negative for antiferromagnetic, expressing the antiparallel alignment that characterize these materials.

The value of the total energy is then provided by:

$$E_{exchange} = J_{ex_{ij}} \sum_{i,j}^{N} \mathbf{S_i}.\mathbf{S_j}. \tag{2.7}$$

The continuum approach to this expression is rather complex and comprises different approaches and approximations [44–48]. First, it is considered the classical approach by defining the spin matrices as classical vectors, arriving to:

$$E_{exchange} = J_{ex} S^2 \sum_{i,j}^{N} \cos(\theta_{ij}) = 2 J_{ex} S^2 \sum_{i<j}^{N} \cos(\theta_{ij}), \tag{2.8}$$

where S is the magnitude of the spin, θ_{ij} the angle defined by the two neighbour atoms, and the factor 2 appears by considering the summation over non repeated pairs.

The next approximation arrives from the proposal that the angle between neighboured atoms is small, $\theta_{ij} \ll 1$, thus:

$$\cos(\theta_{ij}) \approx 1 - \frac{1}{2}\theta_{ij}^2. \tag{2.9}$$

Resulting for the non-constant term in equation 2.8:

$$E_{exchange} = J_{ex}S^2 \sum_{i<j}^{N} \theta_{ij}^2. \tag{2.10}$$

Now, for a small angle θ_{ij}^2:

$$|\theta_{ij}| \approx |\mathbf{m_i} - \mathbf{m_j}|, \tag{2.11}$$

where $\mathbf{m_{i,j}}$ is a unit vector parallel to the local spin direction.

Defining the Taylor series expansion around the lattice point of each atom ($\mathbf{r_i}$) it's obtained:

$$\mathbf{m_j} - \mathbf{m_i} = (\mathbf{r_j}.\boldsymbol{\nabla})\mathbf{m_j}. \tag{2.12}$$

Thus, from equation 2.10:

$$E_{exchange} = J_{ex}S^2 \sum_{i<j}^{N} \mathbf{r_j}.\boldsymbol{\nabla}\mathbf{m_j}^2 = J_{ex}S^2 \sum_{i<j}^{N}((\mathbf{r_j}.\boldsymbol{\nabla}m_{x_j})^2 + (\mathbf{r_j}.\boldsymbol{\nabla}m_{y_j})^2 + (\mathbf{r_j}.\boldsymbol{\nabla}m_{z_j})^2). \tag{2.13}$$

For a body-centered cubic lattice with lattice a:

$$E_{exchange} = A \sum_{k=x,y,z} (\boldsymbol{\nabla}m_k)^2, \tag{2.14}$$

where $A = a^2 J_{ex} S^2$.

In this last equation it is noticed that if the magnetization variation is large so will be the energy. Therefore, as mentioned before, this interaction introduces a preference for the alignment between the atoms.

Also, this form of interaction is more dominant inside a distance called Exchange length, represented by L_{ex} and expressed by:

$$L_{ex} = \sqrt{\frac{B}{K_m}}, \tag{2.15}$$

where K_m is a energy density given by:

$$K_m = \frac{1}{2}\mu_0 M_s^2, \tag{2.16}$$

and B is a material constant defined by:

$$B = J_{ex}S_2/a. \tag{2.17}$$

For a NiFe permalloy this distance is the order of nm.

Anisotropic Energy

The anisotropy effect arises from the interaction between the atoms and the crystallographic structure of the material. Thus, anisotropic energy describes the phenomenon at which the magnetic moments of the atoms in a crystalline material tend to align with a specific direction, designated by *Easy-axis* and expressed by the anisotropic vector K. Therefore, the easy-axis is the direction in the material that minimizes its energy. This preferential direction can arise from the crystalline structure of the material, the shape, the stress, among others. Usually, this direction is established by applying a magnetic field during the deposition process of the material.

The anisotropic energy is a function of the angles between the magnetization and all the axis of the crystalline structure. Nonetheless, the materials used in this study are most of the time characterized for having only one easy-axis. Thus, the anisotropic energy is described as the energy necessary to rotate the magnetization of the material from its easy-axis to its hard-axis, and is defined as [46]:

$$E_k = \sum_{n=1}^{\infty} K_n \sin^{2n}(\theta), \tag{2.18}$$

where θ is the angle between the magnetization and the easy axis and K_n is a constant. Notice that only even powers of $\sin(\theta)$ are included because magnetically a positive rotation relative to the easy-axis is equivalent to a negative rotation.

Experimental observations evidence that, for the materials under study in this thesis, a good representation of the anisotropic energy is given by the first two terms [46]. Based on this, the total anisotropic energy is described as:

$$E_k = \int_V \left(K_1 \sin^2(\theta) + K_2 \sin^4(\theta)\right) dV. \tag{2.19}$$

Magnetostatic Energy

Whenever a magnetization is present with a component normal to the surface, it promotes the arising of poles at the surface. This distribution creates a magnetic field that is opposite to the field that originated it, and thus called Demagnetizing field (H_D) (figure 2.4). A higher magnetization implies that more virtual magnetic charges arise in to the surface, which, in turn, creates a higher demagnetizing field.

Magnetostatic energy, also called demagnetizing energy, has an origin similar to the Zeeman energy previously described. While the last one describes the interaction between the magnetization and the applied field, magnetostatic energy describes the interaction of magnetization with the demagnetizing field, and so defined as:

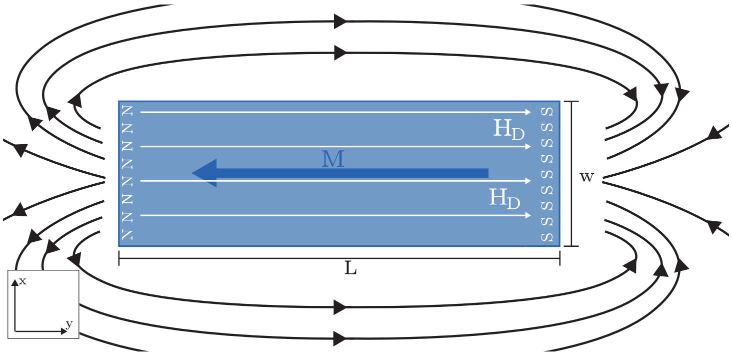

Figure 2.4: Demagnetizing field representation in a ferromagnetic material.

$$E_d = -\frac{\mu_0}{2}\int_V \mathbf{H_d}.\mathbf{M}dV, \tag{2.20}$$

where $\mathbf{H_d}$ is given by [49]:

$$H_d = -\mathbf{D}.\mathbf{M}, \tag{2.21}$$

where $\mathbf{D}$ is the demagnetizing matrix. This matrix depends on the shape of the material and its calculation is complex, which makes it one of the critical points related with micromagnetic and energy minimization studies [50].

The energy includes the $^1/_2$ multiply factor coming from the fact that the demagnetizing field was created by the magnetization and so it is an intrinsic energy term. The same occurs, for example, when calculating the energy of a charge distribution, where is considered $^1/_2$ term so that the energy between the same two charges is not counted twice.

The minimization of this energy implies the rotation of the magnetic dipoles at the surface which causes the material to create domains. This way, the magnetic charges from one domain cancel the charges form an adjacent domain.

In the limit, the material would break successively into smaller domains until the magnetization achieve zero value. Nevertheless, the exchange interaction described previously acts in an opposite way, since it promotes the alignment of the atoms inside the material. However, demagnetizing energy is a long-range effect whereas the exchange interaction is short-range, quantitatively given by the exchange length L_{ex}. This results in the formation of domains walls with thickness of order of L_{ex}.

To minimize the energy, this domain walls align in an antiparallel configuration. However, the change in spin between two adjacent layers with opposite magnetization cannot occur abruptly since the equation 2.7 expresses that the energy is minimized for small variations of magnetization's direction (θ).

For this reason, between these adjacent layers exists transition layers, where the magnetization variation is done through atomic layers, which are called *Bloch Walls*.

Considering a rectangle shape ferromagnetic layer, the demagnetizing field can have a x (H_{D_x}) and y (H_{D_y}) components, depending on the magnetization orientation, given by the following equations [51]:

$$H_{D_x} = 4\pi M_s \frac{t}{W} \cos(\theta) \tag{2.22}$$

$$H_{D_y} = 4\pi M_s \frac{t}{L} \sin(\theta) \tag{2.23}$$

where M_s is the magnetization of the ferromagnetic layer, t is the thickness, W and L are, respectively, the width and length of the layer, and θ is the angle between the magnetization and the x-axis.

Néel Energy

When thin films of ferromagnetic materials are deposited, its surface is not completely flat. Instead, it presents roughness on the surface with a topography usually referenced as "Orange-peel". When dealing with multiple ferromagnetic layers, this roughness have an important influence on their behaviour.

Considering a structure composed by two ferromagnetic layers with one nonmagnetic spacer in between, due to the roughness, their magnetic dipoles interact creating a magnetic field (figure 2.5). As explained before for the Zeeman energy and for the Demagnetizing field, any field interacts with the material's magnetization in the form of equation 2.5. Hence, in this case, Néel Energy is expressed as:

$$E_{Neel} = -\mu_0 \int_V \mathbf{M}.\mathbf{H_N} dV, \tag{2.24}$$

where H_N is the Néel field.

In 1962, Néel derived an expression for this field considering a sinusoidal roughness profile [52]:

$$H_N = \frac{\pi^2}{\sqrt{2}} \frac{h^2}{\lambda t_f} M_{PL} e^{-\frac{2\pi\sqrt{2}t_s}{\lambda}}, \tag{2.25}$$

where h and λ are the amplitude and the wavelength of the profile, t_f and t_s are the thicknesses of the free layer and the spacer, and M_{PL} is the magnetization of the pinned layer.

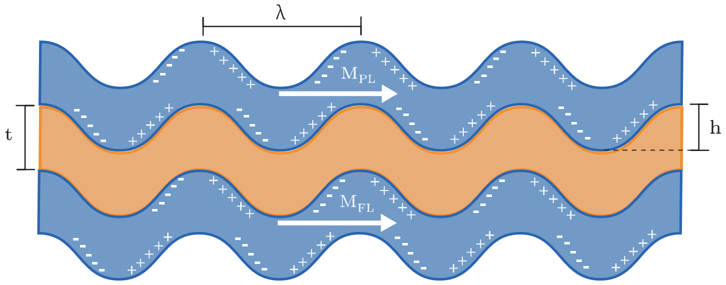

Figure 2.5: Néel Field origin in a FM/NM/FM structure with finite thickness. M_{PL} and M_{FL} are, respectively, the magnetizations of the pinned and free layers, h and λ are the amplitude and the wavelength of the sinusoidal profile, and t is the free layer's thickness. Adapted from [52].

2.2 Giant Magnetoresistance

2.2.1 Origins of GMR

The discover of Giant Magnetoresistance (GMR) was impelled by the development of thin films deposition processes, which allow to deposit almost monoatomic layers. This technique was used to create multilayered systems that revealed properties that were not observable in bulk materials. One interest system is a multilayer system of magnetic and nonmagnetic materials which effectively take advantage of the magnetoresistance property of the materials.

Magnetoresistance is the change of the resistance of a material by applying a magnetic field, which can occur due to different processes that define different types of magnetoresistance as: Anisotropic magnetoresistance (AMR), Giant magnetoresistance (GMR), Colossal magnetoresistance (CMR), Tunneling magnetoresistance (TMR), among others.

GMR was discovered by Baibich *et al.* in 1988 [53] by studying antiferromagnetically coupled Fe/Cr multilayers. Since then, GMR has been observed in other multilayer structures of the form of $(FM/NM)_n$ [54] where FM is a ferromagnetic material (Ni, Fe, Co, or their alloys) and NM is a nonmagnetic material, usually a noble metal (Cu, Ag, Au, Ru, among others).

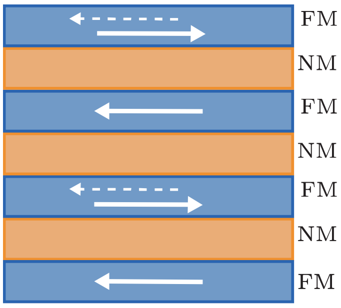

Figure 2.6: GMR multilayer representation. Solid lines represent the magnetizations' directions for antiferromagnetic coupling, while dashed lines represent ferromagnetic alignment.

GMR multilayers are composed by ferromagnetic layers separated by non magnetic layers, represented in figure 2.6. When two ferromagnetic materials are separated by a nonmagnetic one, they can reveal antiferromagnetic or ferromagnetic coupling, which means that the layers' magnetization is antiparallel or parallel aligned, respectively. This coupling is mediated by the electrons in the nonmagnetic layer and oscillates between ferromagnetic and antiferromagnetic as a function of the nonmagnetic layer's thickness. The oscillation is described by the Ruderman-Kittel-Kasuya-Yosida (RKKY) interaction.

As demonstrated in section 2.2.3, the resistance of this multilayer system changes with the relative orientation of the layers' magnetization due to spin scattering dependency on the layers' magnetization. The high resistance state occurs for an antiparallel alignment of the magnetizations, and the low resistance state is obtained for a parallel alignment. To be used as a magnetic field sensor, the ferromagnetic layers, which compose the GMR multilayer system, must be antiferromagnetically coupled [1] so that the

---

[1] Actually, it is possible to create a GMR sensor without antiferromagnetic coupling. By introducing two types of ferromagnetic materials with different coercivities, called soft and hard magnetic materials. This means that the field necessary to rotate each

magnetic field can rotate the magnetizations, changing the resistance state as represented in figure 2.7. However, the necessary field to rotate an antiferromagnetic coupled layer is extremely large (for the mentioned Fe/Cr system, this field is approximately $2\,\mathrm{T}$), which makes it infeasible for practical magnetic field sensors [55].

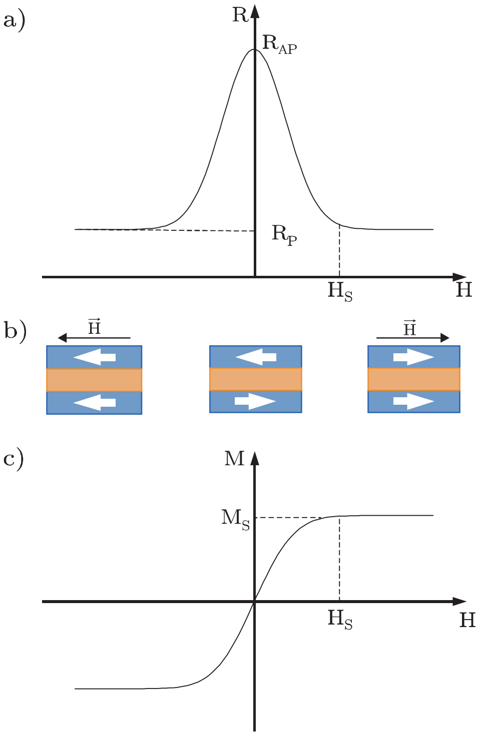

Figure 2.7: Schematic representation of the GMR effect. a) and c) represent the change in the resistance and magnetization of the system, respectively. b) represents the rotation of each layer's magnetization. H_s is the field at which the magnetization is maximum (M_s), which means that it is totally align with the field. R_{ap} and R_p express the resistance at antiparallel and parallel states, respectively. Adapted from [55].

This problem has been overcome by the development of noncoupled magnetic layers structures, which can be switched from an antiparallel to a parallel configuration with lower fields, and are called spinvalves.

2.2.2 Spinvalves

Spinvalve structure was first proposed in 1991 by Dieny *et al.* [56] and later developed by Heimi *et al.* It can be described by a four layered structure that consists in two ferromagnetic (FM) layers, one antiferromagnetic (AFM) and one nonmagnetic (NM). One of the ferromagnetic layers has its magnetization "pinned" (Pinned layer) by the exchange coupling with the antiferromagnetic layer (Pinning layer) adjacent to it. The other ferromagnetic layer (Free layer) is free to rotate since the thickness of the nonmagnetic layer (Spacer) is enough to make the coupling between the two ferromagnetic layer negligible [55]. This arrangement is represented in figure 2.8. Due to weak coupling between the ferromagnetic layers, these structures present better sensitivities than the GMR multilayer structures

---

magnetization differs, thus providing field ranges where antiparallel alignment of the magnetizations is achieved.

[55].

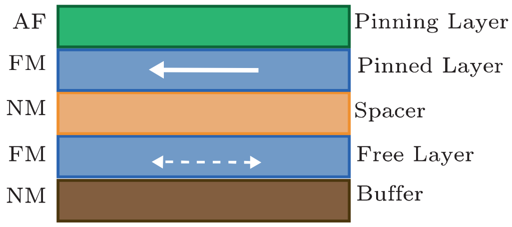

Figure 2.8: Spinvalve representation.

As for the GMR multilayer, the spinvalve's resistance will vary with the relative orientation of the magnetic layers. The maximum value of resistance is achieved when the free and pinned layers are antiparallel (R_{ap}) while the minimum value is obtained for a parallel state (R_p). Numerically, Magnetoresistance (MR) is characterized by:

$$MR = \frac{R_{ap} - R_p}{R_p}. \tag{2.26}$$

Spinvalve sensors can be used in two different configurations, related to the way the sensor is biased and consequently measured, represented in figure 2.9. The most used geometry is current-in-the-plane (CIP), where the biasing current is applied parallel to the layers. On the contrary, current-perpendicular-to-the-plane (CPP) configuration is less used since the resistance of the nanometric layers is very small which makes the measurements of the sensor more difficult.

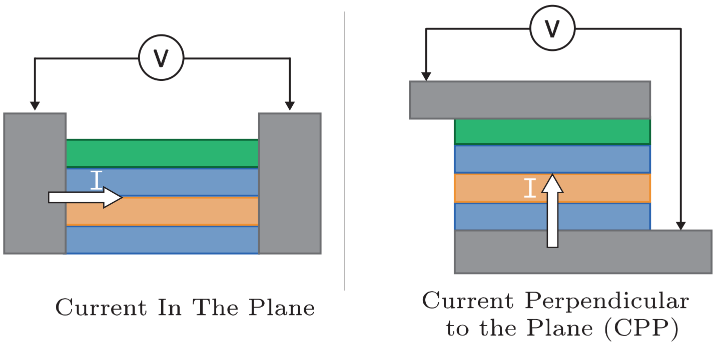

Figure 2.9: Representation of CIP and CPP configurations.

Interlayer Coupling

Figure 2.10 shows the standard $R(H)$ curve for a spinvalve sensor. It is observed a similar behaviour to the curve for a ferromagnetic material. However, a spinvalve sensor shows better linearity and also a shift of the curve, called fringe field (H_f).

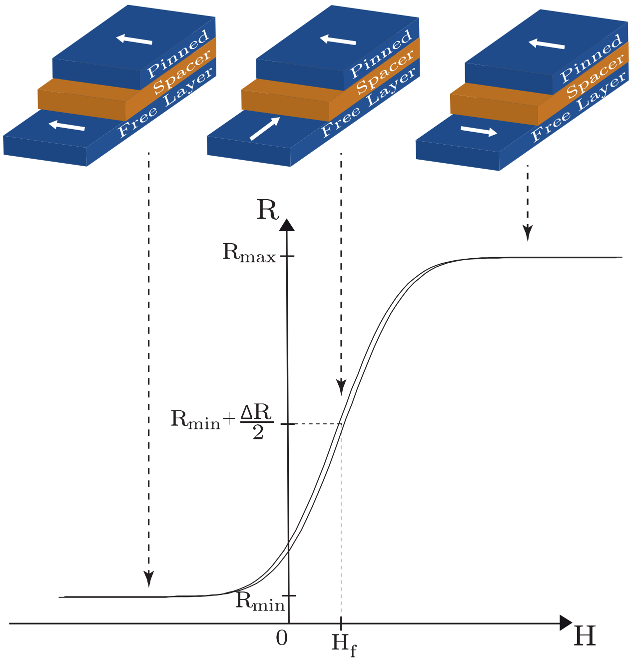

Figure 2.10: Representation of a magnetoresistive curve of a spinvalve sensor.

The shift occurs due to exchange coupling between the free and the pinned layers, although they are separated by the spacer, the coupling still occurs. The energy of the exchange coupling can be described by the following expression [57, 58]:

$$E_{ex} = -J_1 \frac{\mathbf{M_{PL}} \times \mathbf{M_{FL}}}{|\mathbf{M_{PL}}||\mathbf{M_{FL}}|} = - - J_1 \cos(\theta) \tag{2.27}$$

where M_{PL} and M_{FL} are the magnetizations of the pinned and free layers, respectively, and θ is the angle between these magnetizations. J_1 is the coupling coefficient whose signal indicates the coupling type.

The coupling is a cumulative effect of different mechanisms, being the most important the Néel coupling, the RKKY coupling, the magnetostatic field from the pinned layer, and direct coupling [52, 59].

Néel coupling, described in section 2.1.4, consists in an interaction of the magnetic dipoles of each layer due to the roughness that exists in every thin film.

Considering a sinusoidal profile for the roughness, Néel coupling is given by [60]:

$$J_{Neel} = \mu_0 \frac{\pi^2}{\sqrt{2}} \frac{h^2}{\lambda} (M_{PL} M_{FL}) \, e^{\frac{2\pi\sqrt{2}t}{\lambda}}, \tag{2.28}$$

where h and λ are the amplitude and wavelength of the sinusoidal profile. M_{PL} and M_{FL} are the magnetizations of the pinned and free layers, respectively, and t is the spacer thickness. Néel coupling is a ferromagnetic coupling, meaning that it induces a parallel alignment between the two magnetizations. Considering the magnetoresistive curve in figure 2.10, Néel coupling produces a shift to the right of that curve.

The **RKKY coupling** was previously mentioned as the mechanism that defines the antiferromagnetic/ferromagnetic coupling between two ferromagnetic layers separated by a nonmagnetic spacer. It occurs due and the quantum interference in the conduction electrons in the nonmagnetic layer. RKKY coupling is described as:

$$J_{RKKY} = \frac{J_0}{t^2} \sin\left(\frac{2\pi t}{\Lambda} + \varphi\right), \tag{2.29}$$

where J_0 is the RKKY coupling coefficient, t is the thickness of the spacer, and Λ and φ are the period and phase of oscillation, respectively.

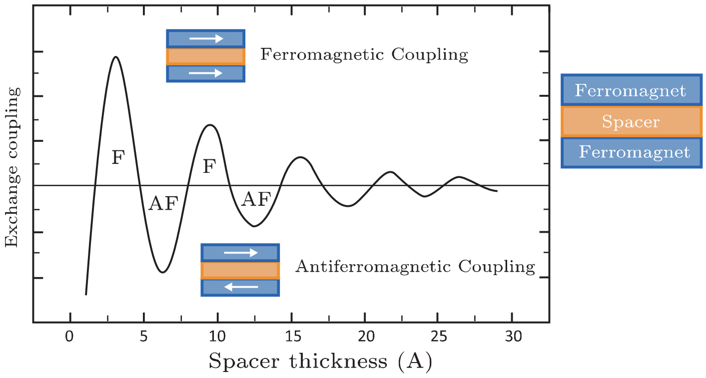

Figure 2.11: Representation of the oscillatory behaviour of RKKY coupling. Adapted from [61].

As observed in figure 2.12, in spinvalves, RKKY coupling is often neglegible when compared with the Néel coupling created by the roughness.

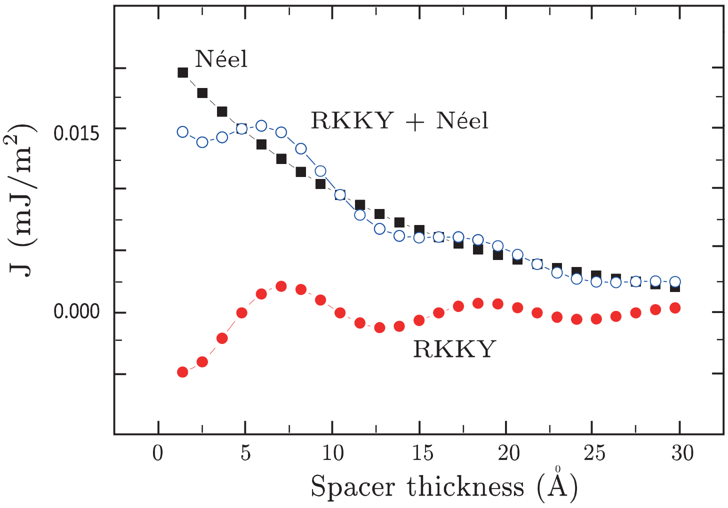

Figure 2.12: Simulated RKKY and Néel interlayer coupling from [58].

Another effect that causes the shift of the curve is the **demagnetizing field** from the pinned layer sensed by the free layer, which is only observed in patterned structures. The small dimensions (in the order of µm) increase the interactions between the virtual magnetic charges created in the surfaces of the sensor. This interaction generates a magnetic field opposite to the magnetization.

Considering that the magnetization of the pinned layer doesn't rotate, its demagnetizing field will be constant, creating a shift in the M(H) curve. Since the demagnetizing field from the pinned layer is sensed by the free layer in the opposite direction of the pinned layer's magnetization, it constitutes an antiferromagnetic coupling, inducing a shift to the left in the transfer curve presented in figure 2.10.

Finally, **direct coupling** can occur through pinholes in the nonmagnetic layer. These pinholes appear in thin layers due to roughness and also inter-difusion between the nonmagnetic and ferromagnetic layers. For the spacer's thickness range used in this thesis ($t > 20$ Å), this influence is not relevant.

Linearization

An ideal transfer curve of a sensor is defined by having no fringe field, no coercivity and also being linear.

As mentioned previously, the fringe field occurs due to interlayer coupling. For a patterned spinvalve, the more relevant mechanisms that contribute to the interlayer coupling are the Néel Coupling and the demagnetizing field from the pinned layer. Accordingly, the optimization strategy consists in changing the thickness of the spacer and the pinned layer. To reduce the exchange coupling is necessary to increase the spacer thickness to increase the distance between the layers, or reduce the thickness of the pinned layer to reduce its magnetization.

Linearity can be achieved in two ways. One consists in depositing the spinvalves with crossed anisotropies, meaning that the anisotropy of the free layer is rotated 90° relative to the pinned layer. Notice that the anisotropy is defined by the magnetic field that is applied during the deposition of the magnetic layers.

The second approach relies in defining a shape that will create an effect called Shape Anisotropy that simulates the crossed anisotropy configuration. If the spinvalve is patterned as a rectangle, with one of its sizes much bigger than the other, the demagnetizing field parallel to the smaller side is much stronger, since the two correspondent surfaces will be much closer, as given by equations 2.22 and 2.23. Consequently, the minimum energy is achieved when the magnetization is parallel to the larger size. This favoured direction corresponds to the shape anisotropy direction.

To understand how the anisotropies configurations influence the behaviour of the spinvalve sensor, an analysis of the free layer energy is performed [62–64]. The energy terms are based in the ones described in section 2.1.4 and also in the interlayer coupling explained in the previous section. Also, is used the mono-domain approach, meaning that each layer is considered to be defined by only one magnetic moment.

The following energy terms were assumed:

- **Zeeman Energy:** Describes the energy from the interaction between the applied magnetic field and the free layer's magnetization, as:

  $$E_{Zeeman} = -\mu_0 \mathbf{H} \cdot \mathbf{M_{free}} V = -\mu_0 H M_{free} \cos(\theta) V, \tag{2.30}$$

  where μ_0 is the vacuum permeability, H is the applied field, M_{free} is the magnetization of the free layer, θ is the angle between the magnetization and the applied field, and V is volume of the free layer.

- **Free Layer's Demagnetizing Energy:** Describes the energy from the interaction between the applied magnetic field and the demagnetizing field from the free layer, as:

  $$E_{Demag_{Free}} = -\frac{1}{2}\mu_0 \mathbf{H_{D_{free}}} \cdot \mathbf{M_{free}} V, \tag{2.31}$$

  where $H_{D_{free}}$ is the demagnetizing of the free layer. As mentioned before, this field is difficult for most geometries. Here, only the x component is considered, which is the most relevant considering the geometries of the problem, expressed as:

  $$\mathbf{H_{D_{free}}} = -N_{xx} M_{free} \cos(\theta)\mathbf{x}, \tag{2.32}$$

  where N_{xx} is the xx component of the demagnetizing matrix expressed in equation 2.21. Accordingly, the energy term is defined as:

  $$E_{Demag_{Free}} = \frac{1}{2}\mu_0 N_{xx} M_{free}^2 \cos^2(\theta) V, \tag{2.33}$$

- **Pinned Layer's Demagnetizing Energy:** Describes the energy from the interaction between the applied magnetic field and the demagnetizing field of the pinned layer sensed by the free layer, as:

  $$E_{Demag_{Pinned}} = -\mu_0 \mathbf{H_{D_{pinned}}} \cdot \mathbf{M_{free}} V = -\mu_0 H_{D_{pinned}} M_{free} \cos(\theta) V, \tag{2.34}$$

  where $H_{D_{pinned}}$ is the demagnetizing field of the pinned layer sensed by the free layer.

- **Néel Energy:** Describes the energy from the interlayer coupling between the free and pinned layers due to the roughness from the thin film, as:

  $$E_{Neel} = -\mu_0 \mathbf{H_N} \cdot \mathbf{M_{free}} V = -\mu_0 H M_{free} \cos(\theta) V, \tag{2.35}$$

  where H_N is the magnetic field created by the interaction of the magnetic dipoles from the free and pinned layers due to the surface roughness.

- **Crystalline Anisotropy Energy:** Describes the energy that results from rotating the magnetization away from the anisotropic direction. This can be seen as an energy coming from the interaction between the magnetization and an anisotropic field (H_k) that tries to rotate the magnetization back to the favoured crystalline axis. The energy terms depend on the anisotropic configuration as:

  $$E_{anisotropy} = \begin{cases} \frac{1}{2}\mu_0 H_k M_{free} \sin^2(\theta) V & \text{for parallel configuration} \\ \frac{1}{2}\mu_0 H_k M_{free} \cos^2(\theta) V & \text{for perpendicular configuration} \end{cases}, \tag{2.36}$$

For the parallel configuration (figure 2.13), the total energy density is then described by:

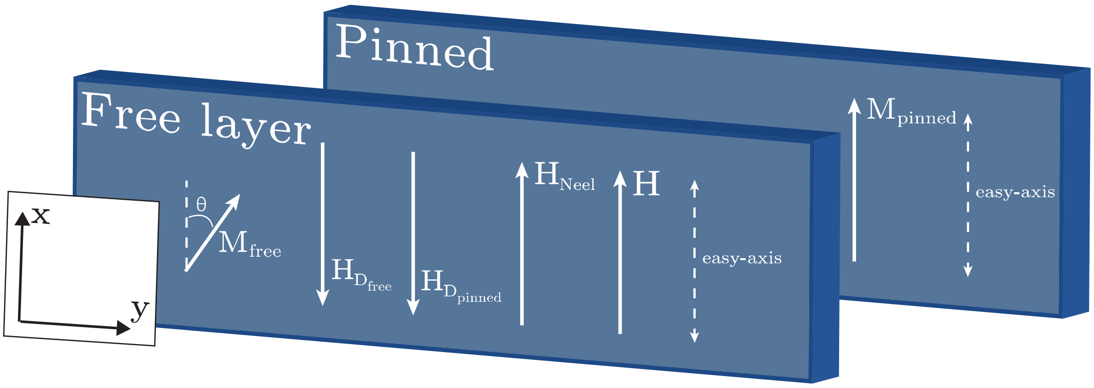

Figure 2.13: Schematic of the fields present in the free layer, for parallel anisotropies.

$$\frac{E_{total}}{V} = \varepsilon_{total} = \mu_0 M_{free}\left[\frac{1}{2}N_{xx}M_{free}\cos^2(\theta) + \frac{1}{2}H_k\sin^2(\theta) - \cos(\theta)\left(H - H_{D_{pinned}} + H_{Neel}\right)\right] \tag{2.37}$$

The minimization of a function is defined by the value at which the first derivative is null and the second is positive. Thus, for the energy of the free layer, the conditions for the first and second derivatives are expressed as:

$$\frac{\partial\varepsilon_{total}}{\partial\theta} = \mu_0 M_{free}\sin(\theta)\left[H - H_{D_{pinned}} + H_{Neel} + (H_k - N_{xx}M_{free})\cos(\theta)\right] = 0 \tag{2.38}$$

$$\frac{\partial^2\varepsilon_{total}}{\partial^2\theta} = \mu_0 M_{free}\left[\left(H - H_{D_{pinned}} + H_{Neel}\right)\cos(\theta) + (H_k - N_{xx}M_{free})\left(2\cos^2(\theta) - 1\right)\right] > 0 \tag{2.39}$$

Equation 2.38 have two possible solutions described as:

$$\sin(\theta) = 0 \Rightarrow \theta = 0 \vee \theta = \pi \tag{2.40}$$

$$\cos(\theta) = \frac{H - H_{D_{pinned}} + H_{Neel}}{N_{xx}M_{free} - H_k} \tag{2.41}$$

Considering the first solution, the condition obtained from the second derivative (equation 2.39) is then defined as:

$$\frac{\partial^2\varepsilon_{total}}{\partial^2\theta} > 0 \Rightarrow \begin{cases} H > H_{D_{pinned}} - H_{Neel} + (N_{xx}M_{free} - H_k) & \text{for } \theta = 0 \\ H < H_{D_{pinned}} - H_{Neel} - (N_{xx}M_{free} - H_k) & \text{for } \theta = \pi \end{cases}, \tag{2.42}$$

Only if $H_k > N_{xx}M_{free}$ the solution is complete, meaning that all values of H have a corresponding angle θ. In this case, only two values for the angle are possible: $\theta = 0$ and $\theta = \pi$. This behaviour is represented in figure 2.14 and indicates that for parallel anisotropy configuration, if the energy from the free layer's demagnetizing field is lower than the anisotropic energy, the sensor is not linear and presents a square response, instead.

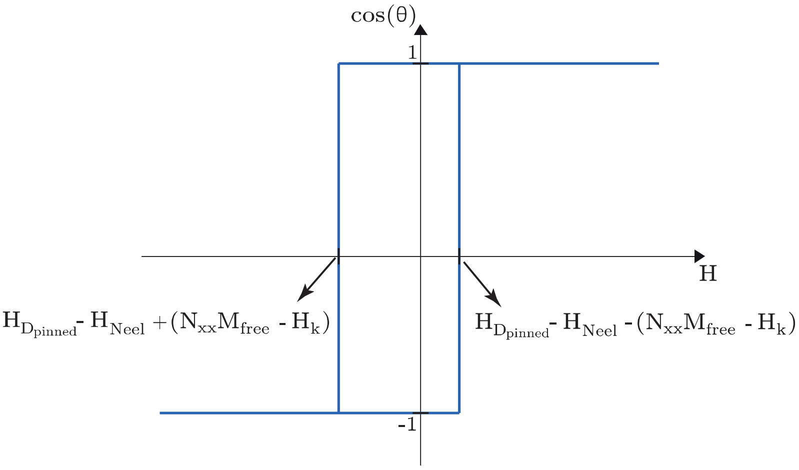

Figure 2.14: Square response representation for parallel anisotropies configuration.

Accordingly, if the demagnetizing field energy term is higher than the anisotropic energy term, described as $N_{xx}M_{free} > H_k$, the first solution is not complete thus is necessary to consider the second one. Replacing it in equation 2.39, the magnetic field range in which the solution is valid is obtained :

$$\begin{cases} H > H_{D_{pinned}} - H_{Neel} - (N_{xx}M_{free} - H_k) \\ H < H_{D_{pinned}} - H_{Neel} + (N_{xx}M_{free} - H_k) \end{cases}, \tag{2.43}$$

Thus, the response of the sensor is linear, as presented in figure 2.15. This indicates that even with parallel anisotropies, it is possible to obtain a linear response if the free layer's demagnetizing energy is larger than the anisotropic energy term, which is doable using a rectangular shape. Considering equation 2.41, the sensitivity is given by $\frac{1}{N_{xx}M_{free}-H_k}$ and the offset by $H_{D_{pinned}} - H_{Neel}$.

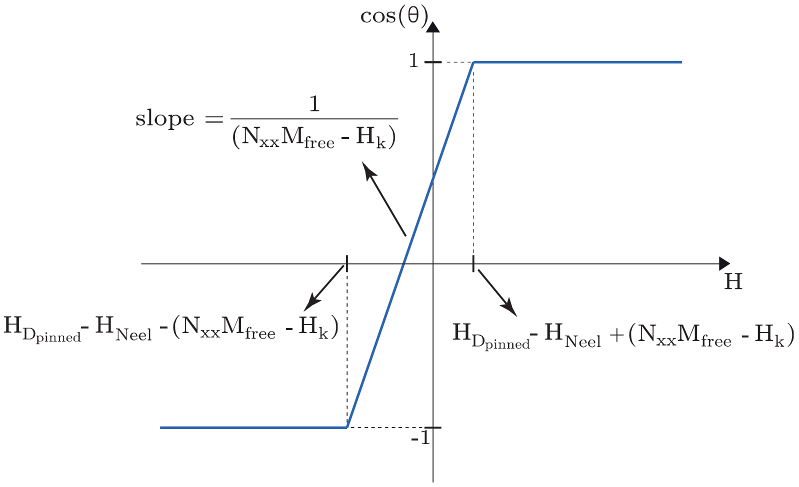

Figure 2.15: Linear response representation for parallel anisotropies configuration.

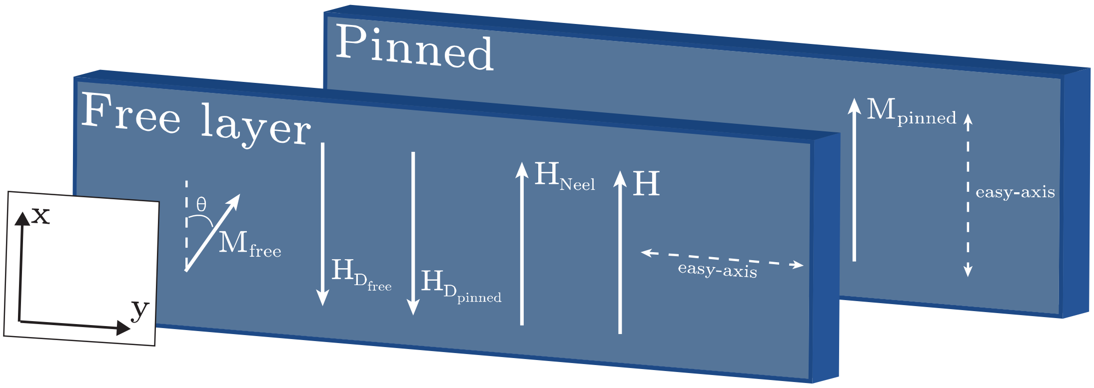

Figure 2.16: Schematic of the fields present in the free layer for crossed anisotropies.

Finally, considering now the crossed anisotropies configuration (figure 2.16), the expression for the total energy density is:

$$\begin{aligned}\frac{E_{total}}{V} = \varepsilon_{total} = \mu_0 M_{free}\Bigg[&\frac{1}{2}\cos^2(\theta)\left(N_{xx}M_{free} + H_k\right)\\ &- \cos(\theta)\left(H - H_{D_{pinned}} + H_{Neel}\right)\Bigg]\end{aligned} \tag{2.44}$$

Following the same procedure used for parallel configuration, the conditions for energy minimization are:

$$\frac{\partial \varepsilon_{total}}{\partial \theta} = \mu_0 M_{free}\sin(\theta)\Big[H - H_{D_{pinned}} + H_{Neel} - \left(H_k + N_{xx}M_{free}\right)\cos(\theta)\Big] = 0 \tag{2.45}$$

$$\frac{\partial^2 \varepsilon_{total}}{\partial^2 \theta} = \mu_0 M_{free}\Big[\left(H - H_{D_{pinned}} + H_{Neel}\right)\cos(\theta) - \left(H_k + N_{xx}M_{free}\right)\left(2\cos^2(\theta) - 1\right)\Big] > 0 \tag{2.46}$$

Again, two solutions are possible:

$$\sin(\theta) = 0 \Rightarrow \theta = 0 \vee \theta = \pi \tag{2.47}$$

$$\cos(\theta) = \frac{H - H_{D_{pinned}} + H_{Neel}}{N_{xx}M_{free} + H_k} \tag{2.48}$$

Starting with the first solution, the condition expressed by equation 2.46 gives:

$$\frac{\partial^2 \varepsilon_{total}}{\partial^2 \theta} > 0 \Rightarrow \begin{cases} H > H_{D_{pinned}} - H_{Neel} + \left(N_{xx}M_{free} + H_k\right) & \text{for } \theta = 0 \\ H < H_{D_{pinned}} - H_{Neel} - \left(N_{xx}M_{free} + H_k\right) & \text{for } \theta = \pi \end{cases}, \tag{2.49}$$

This result is similar to the one obtained for the parallel anisotropies. However, since $N_{xx}M_{free}+H_k$ is always positive, the solution is never complete, which means that the square response is not a solution for this configuration. Thus, the conclusion is that for crossed anisotropies configuration the sensor's response is always linear, as represented in figure 2.17. As defined for the previous configuration, the sensitivity is given by $\frac{1}{N_{xx}M_{free}+H_k}$ and the offset by $H_{D_{pinned}} - H_{Neel}$.

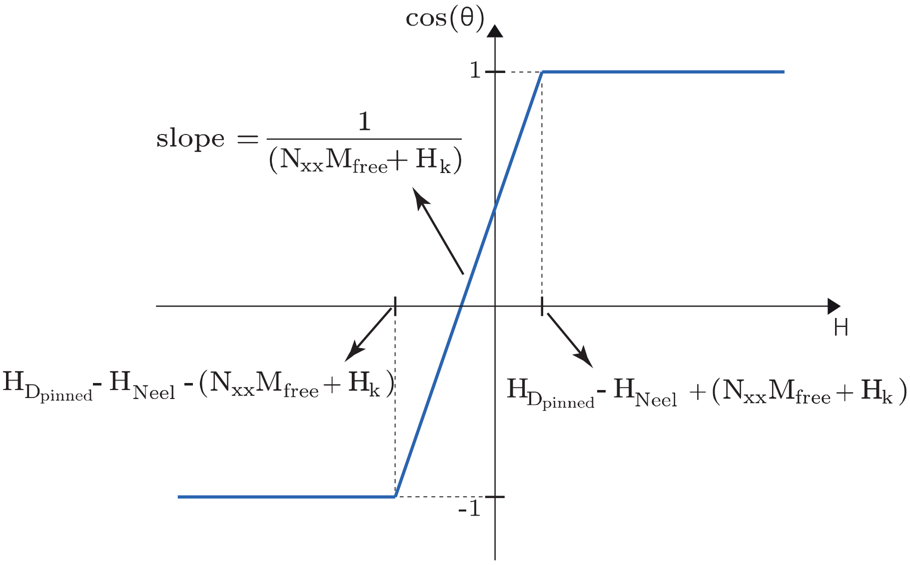

Figure 2.17: Linear response representation for crossed anisotropies configuration.

Spinvalve Improvements

Since it was first proposed in 1991, this structure has been enhanced in terms of MR amplitude and magnetic stability of the pinned layer.

Improvements in magnetic stability are related with higher pinning strength, achieved by using manganese (Mn) alloys, as $PtMn$ or $IrMn$, which provide a large bias field with a high blocking temperature, and also by the introduction of a Synthetic Antiferromagnetic Pinned Layer (SAF). SAF replaces the basic pinned layer by two ferromagnetic layers (typically with thicknesses around 15 Å to 30 Å) with a thin nonmagnetic layer between them, usually composed by ruthenium (Ru) with thicknesses from 5 Å to 10 Å. This structure creates stronger antiferromagnetic coupling between the ferromagnetic layers due to RKKY interaction, as previously mentioned for the antiferromagnetic coupling for GMR multilayer structures. Furthermore, the antiparallel alignment of the magnetization of the two ferromagnetic layers results in a reduced net magnetic moment compared to the single pinned layer, which, for patterning devices, also culminates in a reduced magnetostatic stray field from the pinned layer into the free layer.

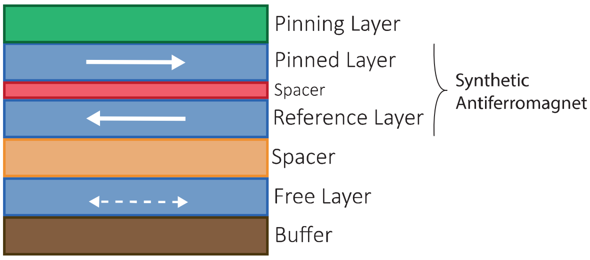

Figure 2.18: Spinvalve with SAF representation.

Besides, the GMR amplitude was improved by the addition of a interfacial layer between the free layer and the spacer (NiFe/Cu). This CoFe layer reduces the intermixing between NiFe and Cu, since Co is much less miscible in Cu than Ni. The intermixing is responsible for magnetic excitations around the interface, which generates spin-flip of the conduction electrons and consequently has a negative impact in the MR amplitude. Combining the two materials into the free layer (NiFe/CoFe), instead of simply replace NiFe for CoFe, is related to the fact that CoFe is a hard magnetic material, meaning that it needs higher magnetic fields to rotate its magnetization (higher coercivity) than a soft magnetic material (lower coercivity), as NiFe.

Another improvement accomplished in the spinvalves is the use of NiFeCr alloys or Ta as buffer layers. The importance of the buffer layers is that it defines the crystalline texture of the layers above it. Gehanno *et al.* [65] studied how the buffer layer influences the texture of the above layers and consequently the spinvalve's characteristics as the MR, coercivity, fringe field and exchange field. The results show that increasing the thickness of the tantalum layer promotes a (111) texture in the above layers and an increase in the grain size and consequently in the surface roughness. The first improves the MR, by decreasing the scattering defects and the magnetic softness of the free layer, meaning that it reduces the formation of domains that lead to higher coercivities. The grain size influences negatively the exchange field of the pinned layer, while the roughness enlarge the fringe field due to the Néel Coupling. Also, the roughness has been proposed has an enhancement of the MR due to a larger effective interface area which increases the density of scattering centers at the interface [66]. These results are shown in figure 2.19.

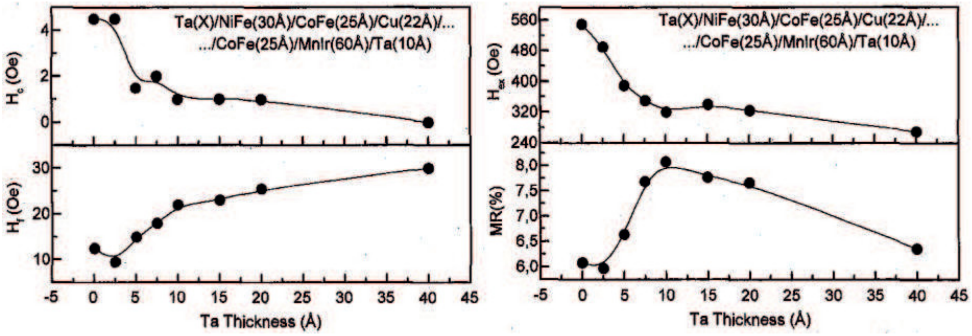

Figure 2.19: Results from Gehanno *et al.* [65], showing the influence of the buffer layer in the MR, coercivity, exchange field and fringe field of a spin valve composed by: Si / Al_2O_3(1500 Å) / Ta(x) / NiFe(30 Å) / CoFe(25 Å) / Cu(22 Å) / CoFe(25 Å) / MnIr(60 Å) / Ta(40 Å).

2.2.3 Mott Model

Mott Model allows to describe the GMR qualitatively. This model helps to understand why the antiparallel state implies a higher resistance than the parallel state. For that, it first proposes that the conduction of electrons with spin-up and spin-down is made in independent parallel channels [67]. This derives from the fact that in a metal, the probability of spin-flip is small, which means that the spin of electrons is mostly conserved during scattering. Consequently, the two spin channel are independent and parallel to each other.

Secondly, the scattering rates for each spin channel are different. The scattering of conduction electrons occurs mostly in the d-bands that are characterized for having different density of states (DOS) at the Fermi level, for each spin. Since the scattering depends on the DOS, the scattering of each channel will differ, being higher for the spin with higher DOS at Fermi level [57].

Finally, it is assumed that the scattering rate and consequently the resistance is higher (R_H) for electrons with spin antiparallel to the layer's magnetization and lower (R_L) otherwise.

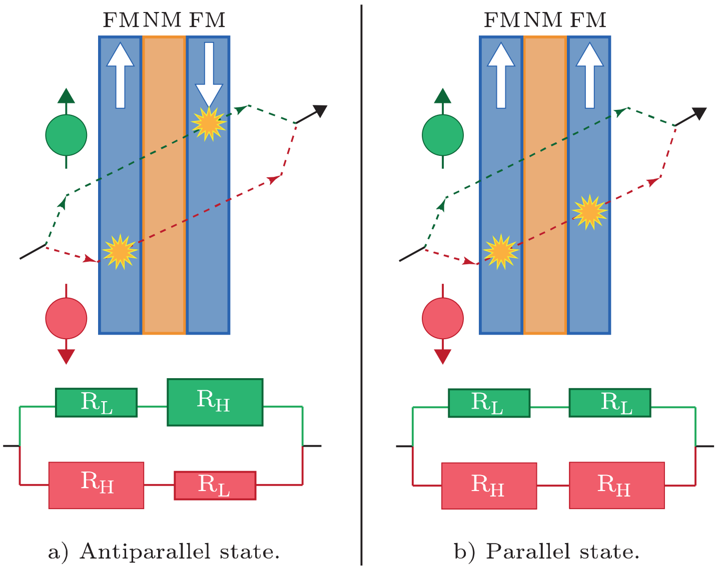

a) Antiparallel state.

b) Parallel state.

Figure 2.20: Mott model representation for antiparallel and parallel states for FM/NM/FM system. R_H represents high resistance due to high scatering between electrons with spin opposite to layer magnetization. R_L represents low resistance due to low scatering between electrons with spin parallel to layer magnetization. Adapted from [68].

With this defined, the model can be applied to the two possible states, as schemed in figure 2.20. First, when the layers' magnetizations are in an antiparallel state, both channels have the same scattering rate, since both have one layer with the same spin orientation and other with opposite direction (figure 2.20 a)). The resistance of this state is expressed by:

$$\begin{aligned} \frac{1}{R_{ap}} &= \frac{1}{R_H + R_L} + \frac{1}{R_H + R_L} \Leftrightarrow \\ \Leftrightarrow R_{ap} &= \frac{R_H + R_L}{2}. \end{aligned} \tag{2.50}$$

On the contrary, in the parallel state, one of the channels have a low scattering rate, since both layers have the same spin direction, while the other one have a high scattering rate, since both layers have magnetizations opposite to its spin (figure 2.20 b)).

$$\begin{aligned} \frac{1}{R_p} &= \frac{1}{R_H + R_H} + \frac{1}{R_L + R_L} \Leftrightarrow \\ \Leftrightarrow R_p &= \frac{2R_H R_L}{R_H + R_L}. \end{aligned} \tag{2.51}$$

Thus,

$$MR = \frac{R_{ap} - R_p}{R_p} = \frac{(R_H - R_L)^2}{4R_H R_L}. \tag{2.52}$$

From equations 2.50 and 2.51, it is observed that, as proposed initially, the resistance in the antiparallel state is higher than in the parallel state.

In equation 2.52, the resistance of the nonmagnetic layer is not considered, which is spin-independent and, thus, adds equally for both the mentioned states. If this contribution is considered, the high and low resistances are then defined as:

$$R_{H|L} = \rho_{NM} d_{NM} + \rho_{H|L} d_M, \tag{2.53}$$

where d_{NM} and d_M are the thicknesses of the nonmagnetic and magnetic layers respectively and ρ_{NM} and $\rho_{H|L}$ are the resistivities of the non-magnetic layer and the high/low resistivity obtained for antiparallel/parallel magnetization spin state, respectively.

Applying 2.53 to 2.52, MR is defined as:

$$MR = \frac{(\alpha - 1)^2}{4\left(\alpha + p\frac{d_{NM}}{d_M}\right)\left(1 + p\frac{d_{NM}}{d_M}\right)}, \tag{2.54}$$

where $\alpha = {}^{\rho_H}/_{\rho_L}$ and $p = {}^{\rho_{NM}}/_{\rho_H}$.

Its observed that MR highly depends on α, which means that MR increases with the spin asymmetry. Also, it decreases with the spacer thickness d_{NM}.

2.2.4 Noise

Noise is a physical phenomenon that describes fluctuations that exist in a system, which can occur in different areas such as acoustics, electronics, optics, statistical mechanics, among many others. In electronics, noise represents voltage or current fluctuation in all passive or active elements.

For sensors, noise is an important element since it limits the detection levels. A signal measured by a sensor must be higher than its noise level, otherwise only noise is measured.

To compare the performance of different magnetoresistive sensors, it is used a concept called detectivity, which quantifies the minimum magnetic field value that can be detected by the sensor. This is measured in ${}^{\mathrm{T}}/_{\sqrt{\mathrm{Hz}}}$ and is given by:

$$D = \frac{S}{{}^{\Delta V}/_{\Delta H}}, \tag{2.55}$$

where S defines the sensor noise voltage output in ${}^{\mathrm{V}}/_{\sqrt{\mathrm{Hz}}}$, and ${}^{\Delta V}/_{\Delta H}$ represents the sensitivity of the sensor or, in other words, the slope of the $V(H)$ curve.

The noise sources of these sensors are described through the following paragraphs.

Thermal Noise

In 1827, during observations of some small object suspended on water, Robert Brown realized that it performed a random motion, later called Brownian motion. Later in 1905, Albert Einstein explained, in precise detail, how this motion was caused by the random collisions with the water molecules due to fluctuations in their thermal energy [69].

The thermal noise was first measured by Johnson, at Bells Lab in 1928 [70]. Later, he explained his findings to Harry Nyquist, who also worked at Bells Lab, which derived for the first time an expression that was able to fit Johnson's measurements based on thermodynamics and statistical mechanics [71]. For this reason, thermal noise is also called Johnson-Nyquist noise [69].

It is the most common kind of noise observed in electronic devices. It arrives from the thermal random motion of the charge carriers, the electrons, due to collision with other electrons and also with impurities of the material. Therefore, it depends on the resistance of the material, since it quantifies these collisions, and also on the temperature, since this one is a measurement of the kinetic energy of the atoms in a material. The non-dependency on the electric current is explained by the fact that electrons' thermal velocity is much higher than electrons' drift velocity, around 10^3 higher.

Thus, thermal noise output is defined as:

$$S^2_{thermal} = 4k_B RT, \tag{2.56}$$

where k_B is the Boltzmann constant, R is the resistance of the sensor and T its temperature.

1/f Noise

1/f noise, also called flicker noise or pink noise, is the most controversial noise and less understood kind of noise. It was first observed in 1925, in a study about thermionic current in vacuum tubes [72]. After that, it has been observed in other situations like electric current, frequency of quartz crystal oscillators, pitch of music, rate of traffic flow, financial data, neuronal activity, hearth beat and many others. This increases the mysterious behind this type of noise present in all kinds of domains with apparently no relation between them. In GMR devices, this noise is often a drawback in performances of magnetoresistive sensors [54].

In 2003, a group led by Alexandre Baladin [73] helped to explain this phenomenon using graphene, allowing to atomically control the thickness of the material. This study demonstrated that this is a volume effect, instead of a surface effect, which, since then, was a heated debate among scientists.

In electronics, *1/f* noise is explained by electron trapping in crystal defects, since after it is released in a random way, following a probability that favours highest energies at low frequencies [29]. Consequently, and contrarily to thermal noise, *1/f* noise is current dependent. Typically, the *1/f* noise level decreases with an increase of the sensor volume which can be understood by an averaging effect [54].

The most universal expression for *1/f* noise is given by:

$$S^2_{1/f} = K\frac{I^a R^2}{f^b}, \tag{2.57}$$

where K is a constant for a specific device, I the bias current, R the resistance, a varies from 0.5 to 2 and, b is approximately 1, and f is the frequency. a depends on the interaction between conduction electrons and materials defects and b is related with *1/f* noise statistics.

For spinvalves, this expression can by more explicit:

$$S^2_{SV_{1/f}} = \frac{\alpha_H}{N_C}\frac{I^2R^2}{f}, \tag{2.58}$$

where N_c is the number of charge carriers and α_H is the *Hooge* constant that can be very different for different devices.

1/f noise can exhibit an electrical and a magnetic component, which are expressed as contributions to the *Hooge* constant previously defined:

$$\alpha_H = \alpha_{H_{electric}} + \alpha_{H_{magnetic}}. \tag{2.59}$$

In spinvalves, the electrical component is negligible when compared with the magnetic one. The magnetic component arrives from magnetic fluctuations in the free layer due to the thermal energy of the domains [74–76]. The fluctuations in the magnetization direction of each domain are then measured as a fluctuation in the resistance of the sensor and, consequently, in the voltage. Therefore, the magnetic 1/f noise depends on the stability of the domain's magnetization, which can be analysed from the energy study performed in section 2.2.2.

The energy equation 2.37 allows to plot the variation of the energy of the free layer with the relative orientation of the pinned and free layers' magnetizations, given by θ (figure 2.21 a)). It is observed that the energy increases when the absolute value of magnetization also increases. In addiction, the slope of $E(\theta)$ is small around $\theta = \pi/2$, which implies that a small change in the energy of the system, caused by the thermal fluctuations, produces a high fluctuation in the magnetization orientation of the layer. Therefore, the stability of the system, and consequently the 1/f magnetic noise, deteriorates around $\theta = \pi/2$.

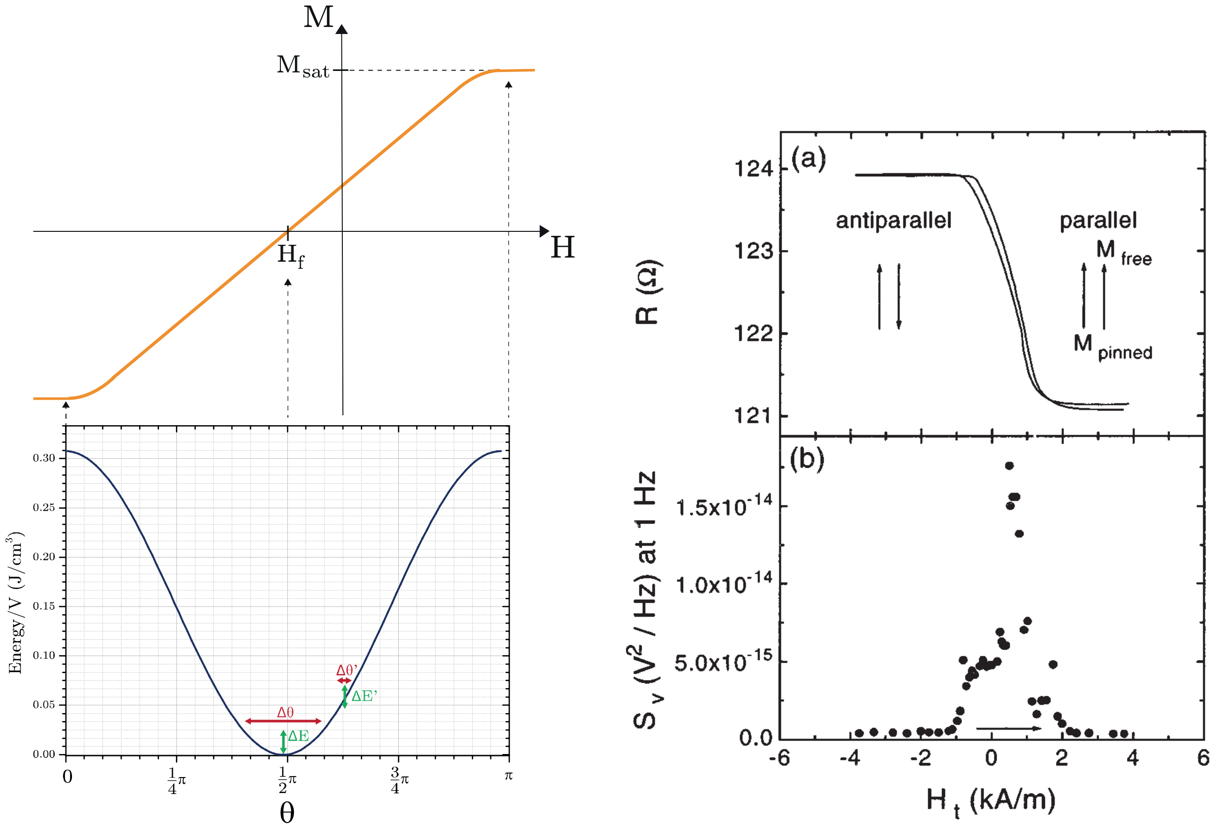

(a) Top - Magnetization Curve. Bottom - Variation of free layer's energy density with the angle θ.

(b) Top - Magnetization Curve. Bottom - Variation of the noise at 1Hz with the magnetic field applied H_t. From [76].

Figure 2.21: a) represents the energy density variation with the angle θ between the magnetization of the free and pinned layers. The energy density values were obtained considering equation 2.37 and $M_s = 7 \times 10^5 A/m$, $H_k = 1.98 \times 10^2 A/m$, $H_{Neel} = 1.86 \times 10^3 A/m$ and $M_{D_{pinned}} = 1.94 \times 10^3 A/m$ [77]. b) represents the noise dependency with the magnitude of the magnetic field applied, and consequently with the relative orientation of the pinned and free layers' magnetizations.

2.2.5 Detectivity - Series and Parallel Configurations

A resistor can be represented in two different ways related to the noise source. It can be represented as a noiseless resistor in series with a voltage noise source, or as a noiseless resistor in parallel with a current source, which represents Thévenin equivalent circuit or Norton equivalent circuit, respectively, represented in figure 2.22. The voltage noise source representation is more useful for the study of series configuration whereas the current noise source helps in the parallel configuration analysis.

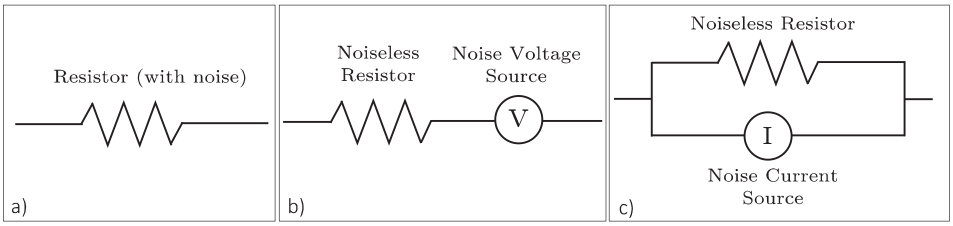

Figure 2.22: Real resistor (*a)*) representation with noise sources by Thévenin equivalent circuit (*b)*) and Norton equivalent circuit (*c)*).

Series Configuration

In the previous section, the total noise of a spinvalve sensors was defined as:

$$S_{SV}^2 = 4k_B rT + \frac{\alpha_H}{N_C}\frac{I^2r^2}{f}. \tag{2.60}$$

Now, N individual spinvalves in series with resistance r are considered [28]. If the SV are biased by a current I, the voltage across the series will be $V_{tot} = NrI = NV_{individual}$. In this way, the total noise is then N times the noise of an individual spinvalve:

$$S_{SV}^2 = N\left(4k_B rT + \frac{\alpha_H}{N_C}\frac{V_{tot}^2}{N^2 f}\right) = 4k_B RT + \frac{\alpha_H}{N_C}\frac{V_{tot}^2}{Nf}. \tag{2.61}$$

Thus, defining sensitivity as:

$$\frac{\Delta V}{\Delta H} = \frac{\Delta r}{r\Delta H}V_{tot} = \gamma V_{tot}, \tag{2.62}$$

$$\gamma = \frac{\Delta r}{r\Delta H},$$

where γ does not depend on the system configuration, only on the sensor proprieties.

As a result, the detectivity is expressed as:

$$D_{SV} = \frac{1}{\gamma}\sqrt{\left(\frac{4k_B NrT}{V_{tot}^2} + \frac{\alpha_H}{N_c Nf}\right)}. \tag{2.63}$$

It is possible to conclude that the thermal term of detectivity will increase with $\sqrt{N}$ while the *1/f* part will decrease with $\sqrt{N}$.

Parallel Configuration

In this section, M spinvalves in parallel configuration are considered [28]. As mentioned before, the best way to analyze this configuration is to think in terms of current noise sources, which, in this case, implies adding the M current noise sources. This sum corresponds to a division by M for the voltage noise output. The final expression for the noise output is given by:

$$S_{SV}^2 = \frac{1}{M}\left(4k_B rT + \frac{\alpha_H I^2 r^2}{N_C f}\right) = 4k_B r'T + \frac{\alpha_H I^2 r^2}{MN_C f}, \tag{2.64}$$

where r' is the equivalent resistance measured from the parallel configuration.

Since sensitivity is defined as:

$$\frac{\Delta V}{\Delta H} = \gamma r' I = \gamma V_{tot}, \tag{2.65}$$

the detectivity of the parallel configuration is given by:

$$D_{SV} = \frac{1}{\gamma}\sqrt{\left(\frac{4k_B rT}{MV_{tot}^2} + \frac{\alpha_H}{N_c M f}\right)}. \tag{2.66}$$

With this, the conclusion is that both noise terms of detectivity decrease with $\sqrt{M}$. The detectivity improvement by this configuration is the main keystone on this work.

Chapter 3

Experimental Methods

This chapter presents the fabrication process of the spinvalves used in this thesis and also the characterization methods that allowed to study their properties. Additionally, every step of the fabrication is described and analysed in detail, identifying the operating machinery used. These fabrication and characterization processes were performed in INESC-MN, Lisboa. INESC-MN operates a $250\,\mathrm{m}^2$ cleanroom composed by class 100 and class 10 areas. At the class 10 area are performed the coating and exposure process of the photoresist layer explained later.

3.1 Fabrication Methods

The fabrication of a spinvalve can be divided into 7 major stages:

- **Mask design**
- **Stack deposition**
- **Spinvalve definition**
- **Contact leads definition**
- **Contacts pads definition**
- **Annealing**
- **Dicing**
- **Wire bonding**

Figure 3.1 illustrates the fabrication process of packaged system, which will be detailed in the following sections.

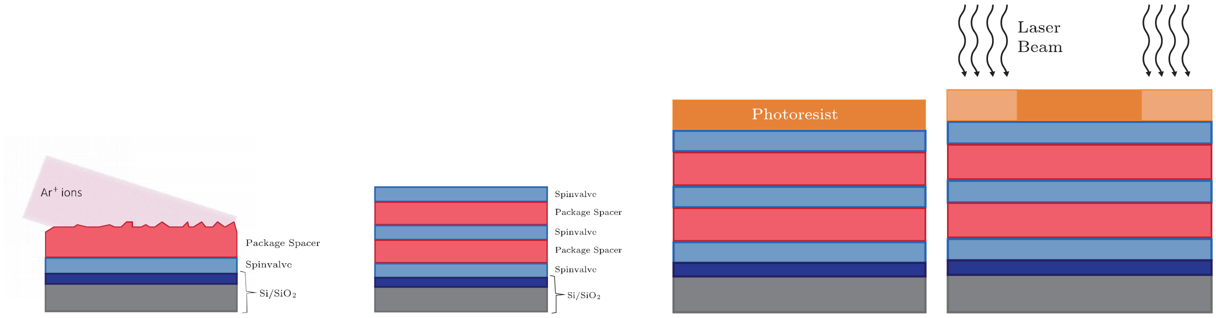

(a) Soft-etch performed, at Nordiko 3600, after each space layer deposition to reduce surface roughness

(b) Cross section of packaged system.

(c) Coated photoresist layer.

(d) 1st lithography to define sensor structure.

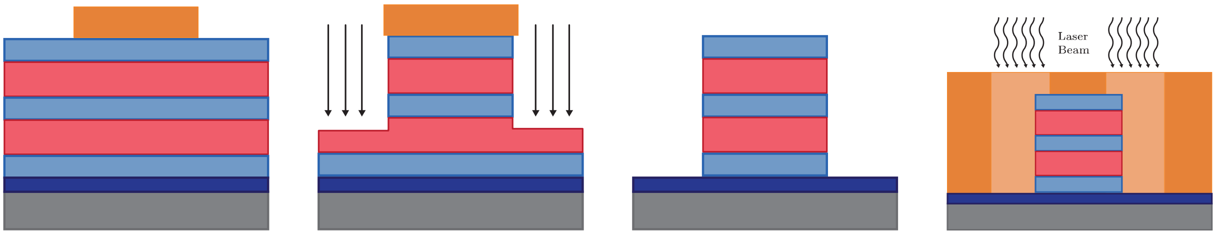

(e) Photoresist structure after development.

(f) Physical etch, performed at Nordiko 3600.

(g) Patterned packaged system.

(h) 2nd lithography to create cavities for contact lead deposition.

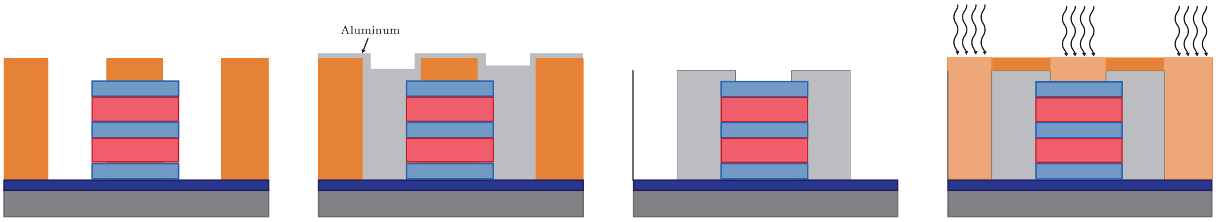

(i) Cavities after development.

(j) Aluminum deposited in Nordiko 7000.

(k) Contact leads structures after aluminum lift-off.

(l) 3rd lithography to define pads structures.

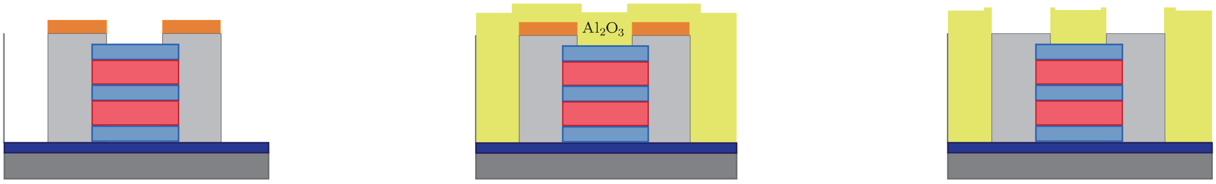

(m) Contact pads structures after development.

(n) Al$_2$O$_3$ deposited on UHV II.

(o) Contact pads after Al$_2$O$_3$ lift-off

Figure 3.1: Schemmatic of the fabrication process for packaged system.

3.1.1 Stack Deposition

For this thesis, several stacks of spinvalves were deposited. Here is presented the two stacks used in the main part, related to the noise and sensitivity study of vertical packaged spinvalves.

- **Nordiko 3000 Stack**

  SV1889: Ta 20 Å / NiFe 26 Å / CoFe 30 Å / Cu 27 Å / CoFe 30 Å / MnIr 75 Å / Ta 50 Å

- **Nordiko 3600 Stack**

  36SV2397: Ta 10 Å / NiFe 28 Å / CoFe 25 Å / Cu 24 Å / CoFe 23 Å / MnIr 70 Å / Ta 30 Å

SV1889 stack was used in the noise and detectivity study (section 4.3), while 36SV2397 was used in the aluminium nitride (AlN) thickness effect on the sensitivity study (section 4.4). The average values of MR, H_f and H_c for both stacks after patterning are represented in the next table:

Stack	**MR (%)**	**H_f (mT)**	**H_c (mT)**
SV1889	5.0	-0.08	0.03
36SV2397	5.4	0.37	0.12

Table 3.1: Average magnetic properties from the two stacks, SV1889 and 36SV2397.

The vertical packaging requires that AlN is deposited between each spinvalve level, which is accomplished using Nordiko 7000. To study different thicknesses of aluminium nitride in the vertical packaging, seven samples were microfabricated, one without AlN and six containing different AlN thicknesses: 100 Å, 200 Å, 300 Å, 700 Å, 900 Å, and 1100 Å.

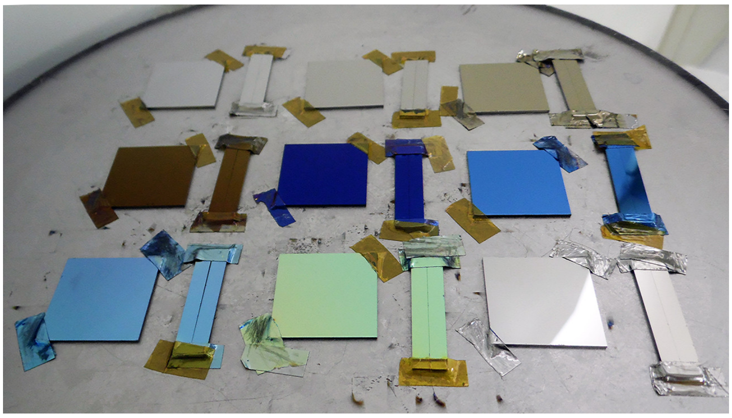

Figure 3.2: Sample aspect after deposited with different thicknesses of AlN.

Nordiko 3600 and Nordiko 3000

As already stated, the deposition of the spinvalves were performed in two different machines: Nordiko 3600 and Nordiko 3000, which are very similar and operate under the same physical process, called Ion Beam Deposition. The difference between these two is its size and components disposition, which defines the different operation voltages, currents and pressures of the process (table 3.2).

As the process name reveals, this process relies on an ion beam that is directed towards a target, made of one of the materials that constitute the stack. Ions, due to their kinetic energy, remove atoms from the target that, because of the components' arrangement, are deposited on the sample. Both machines have six targets, allowing to deposit the six different materials that assemble each stack.

As presented in figure 3.4 a), the ion beam arises from the Deposition Gun, which is composed by an antenna, two capacitors and grids (two grids in Nordiko 3000 and three in Nordiko 3600). To create the ion beam, xenon (Xe) is injected into the gun and a radio frequency (RF) wave is applied by the antenna, ionizing the gas, thus creating plasma. The capacitors purpose is to tune the plasma impedance in a

Parameters	**Nordiko 3600**	**Nordiko 3000**
Sub rotation (rpm)	30	15
RF Power (W)	150	110
Grid 1 Voltage (V)	1005	1022
Grid 2 Voltage (V)	-275	-300
Grid 3 Voltage (V)	-50	—
Gas Flow [Xe] (sccm)	4	2
Beam current (mA)	120	24
Field Strength (mT)	5	4

Table 3.2: Machines' operation parameters.

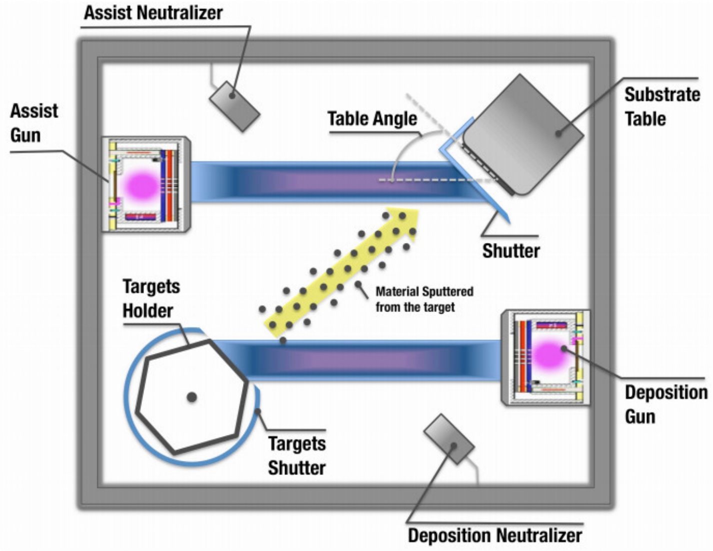

Figure 3.3: Schematic of the inside of a Ion beam System (Nordiko 3600 and Nordiko 3000). Adapted from [78].

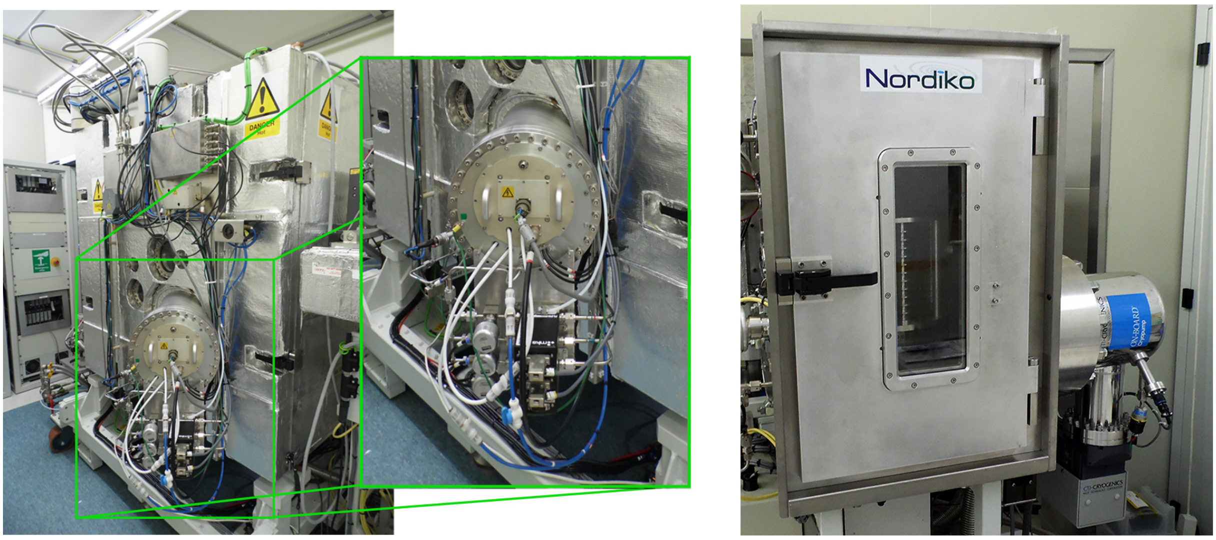

(a) Nordiko 3600 Deposition gun

(b) Nordiko 3600 LoadLock and Cryopump

Figure 3.4: Photographs of deposition gun and loadlock, with its cryopump, from Nordiko 3600.

way that it matches the system impedance, so that the RF power is totally absorbed by the plasma. This is translated in a reflected power closes or equal to zero, and a stable plasma is achieved.

After stability is obtained, the plasma is converted into an ion beam using the grids. Different voltages are applied to the grids, such that the outer grid has a voltage that is lower than the inner grid, creating an electrical field that boosts the positive ions out of the gun. The geometry of the grids is optimized to create a collimated ion beam. The flux of ions coming out of the gun corresponds to a current measured between the grids.

These current and voltages are very important in the deposition rate of the material to be deposited. Higher currents and voltages means that more ions with higher kinetic energy leave the gun and collide with the target removing its atoms, which is noticed as a higher deposition rate.

Both machines operate under a pressure of $1 \times 10^{-8}\,\mathrm{Torr}$, which reduces the contamination during the deposition process.

Nordiko 7000

Nordiko 7000 is an automated system constituted by four modules, one dealer chamber, with a robotic arm responsible by the transport of the wafers through the modules and the loadlock. The loadlock is pumped by a turbo pump that reaches pressures of $5 \times 10^{-6}\,\mathrm{Torr}$, while modules and dealer chamber are pumped by cryogenic pumps, achieving pressures of $5 \times 10^{-9}\,\mathrm{Torr}$.

The physical process behind the operation of this machine is called Magnetron Sputtering [79].

As Ion Beam Deposition, Magnetron Sputtering relies on plasma to deposit material. A gun injects gas into the module where the wafer is placed. Then, two RF power sources are used: one ionizes the gas while the other accelerates the ions towards the target. The ions are generated and pushed into the target, by a cathode placed below it, colliding and, thus, removing atoms that are deposited in the wafer. Below the target are also placed magnets that create a magnetic field that not only confines the plasma to a region close to the target, but also helps to trap free electrons. This trapping is important because otherwise these electrons would collide with the substrate creating overheat problems and also because it enhances their probability of ionizing a neutral atom by several orders of magnitude, increasing the deposition rate.

The four modules perform four distinct tasks:

- **Module 1**: Heating
- **Module 2**: Soft Sputtering Etch
- **Module 3**: TiW(N) Deposition
- **Module 4**: AlSiCu Deposition

In module 1, it is possible to rapidly heat the wafer to a temperature that reaches $500\,^{\circ}\mathrm{C}$. This is achieved with the wafer facing down to an array of lamps placed at the bottom part of the chamber. Hence, module 1 does not perform magnetron sputtering being this operation restricted to modules 2, 3 and 4.

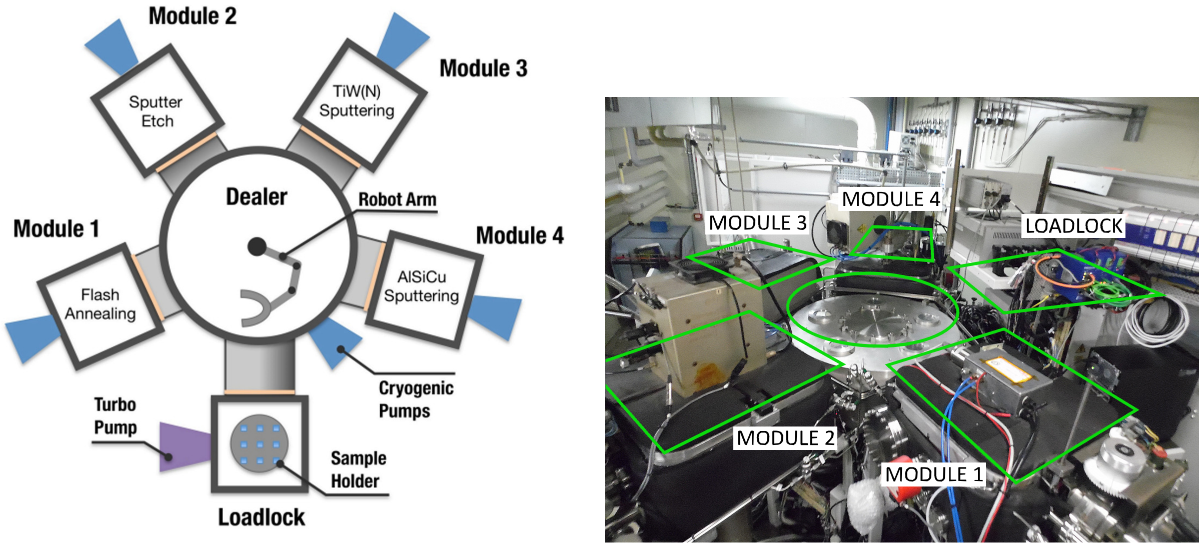

(a) Nordiko 7000 modules schematic. From [80].   (b) Nordiko 7000 modules photograph.

Figure 3.5: Nordiko 7000 modules schematic and photography.

In module 2, is performed soft sputtering etch, which consists in using the plasma to remove/etch atoms from the wafer rather than from a target. This soft etch is used to remove natural oxidation, ensuring good ohmic contact to the new material to be deposited.

Module 3 is used for reactive sputtering deposition of TiW(N). This is achieved by the process of magnetron sputtering, previously described, with a target composed by $Ti_{10}W_{90}$. In addition, a flow of N_2 is injected in the chamber, which provides nitrogen to be deposited along with TiW. TiW is a hard and dense material and is used after the metallization to protect the metal from physical and chemical damaging during the microfabrication process. For this reason, this process is called passivation.

Finally, Module 4 is responsible to create the contact leads in the sensors. These are made of aluminium, which is deposited by sputtering in a $Al_{98.5}Si_{1.0}Cu_{0.5}$ target. As in module 3, if N_2 is injected, during the deposition, the deposited material is AlN instead. This material has good insulator characteristics, being used as a spacer in the vertical packaging of spinvalves, Table 3.3 presents the parameters of module 4, for AlN deposition in Nordiko 7000.

	Ar/N_2 flow (sccm)	**Pressure (mTorr)**	**RF Power (kW)**	**Deposition Rate (Å/s)**
Module 4	10/10	2	1	4

Table 3.3: Nordiko 7000 operation parameters for aluminium nitride deposition.

3.1.2 Spinvalve Definition

After the stack is deposited, the desirable sensor's properties are achieved by patterning the sensors's structures. This step, called patterning, can be obtained by selectively depositing or removing material. Nonetheless, both techniques start with a photolithography process, which consists in using a laser to define structures on micrometer range size, on a material sensitive to light, thus called photoresist.

There are two types of photoresist: positive, which becomes soluble to the photoresist developer when exposed, and negative, which gets insoluble instead. At INESC-MN the mostly used photoresist is positive, meaning that the parts exposed are removed during development.

1st Lithography

The overall photolithography process can be divided into 3 steps:

- Spin-coating the substrate with photoresist;
- Photoresist exposure, with DWL 2.0 laser system;
- Development of the sample, removing the exposed areas.

Before the coating itself, the substrate needs to surpass a pre-treatment process, Vapor Prime, which improves the adhesion of the photoresist. This is performed in a vapor prime oven, which heats the sample until $130\,^{\circ}\mathrm{C}$ and applies an organosilicon compound, hexamethyldisilazane (HDMS), that turns the surface of the sample hydrophobic.

Subsequently, spin-coating is performed in a Sillicon Valley Group (SVG) system (figure 3.6), composed by two tracks: one responsible for the spin-coating (track 1) and the other for the later development (track 2). Spin-coating consists on dispensing photoresist in the center of the wafer and then spin it at 3200 rpm during 30 s to achieve a thickness 1.5 µm. This step finishes after soft baking the photoresist at $85\,^{\circ}\mathrm{C}$ during 1 min, which removes solvents and stress while promoting adhesion.

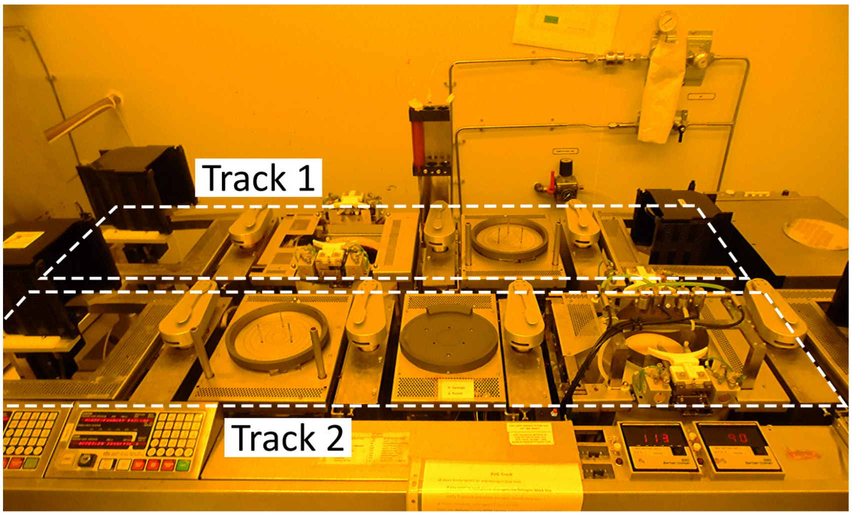

Figure 3.6: Sillicon Valley Group system.

The exposure is performed in DWL 2.0 system (figure 3.7), which uses a 440 nm NeAr laser that defines structures up to 0.8 µm (laser spot size) with a alignment precision of 0.1 µm (stage resolution) on 1.5 µm thick photoresist. Two parameters are available to tune the laser exposure, namely *Focus* and *Energy*. The *Focus* parameter controls the distance at which the laser beam is focused relatively to the camera focus. Since the camera is focused in the structures below the photoresist layer, a *Focus* value of -20 is used to focus the laser on the photoresist. The *Energy* parameter controls the percentage of laser's energy used in the exposure. The energy tune is important because low energies are not able to successfully break the polymer structures while high energies produce reflections in the substrate material that decrease the laser resolution and the sharpness of the structures. At INESC-MN, *Energy* parameter values range from 50 to 65 %, which corresponds to energies from 2.3×10^{-19} J to 2.9×10^{-19} J.

The mask, illustrated in figure 3.8 a), is created in AutoCAD software and then converted to *.lic* files which are recognized by the system of the DWL machine. This conversion divides the mask vertically in stripes, called lics, with a width of $200\,\mu\mathrm{m}$. During the exposure, the laser moves vertically performing one lic, then steps horizontally to the next lic and so on. The laser is actually divided into small pixels, which, during the exposure, are enabled/disabled in a sequence that creates the required structures. Additionally, the AutoCAD mask can be inverted or non-inverted. In inverted masks, the laser exposes the area outside the defined structures, while in non-inverted mask the opposite occurs. Thus, in the end, inverted masks create the structures as defined in AutoCAD, while in non-inverted masks those structures are defined as cavities in the photoresist layer.

Finally, the development is achieved by track 2, starting with a bake at $110\,^{\circ}\mathrm{C}$ during 1 minute, which helps to cease photoresist reactions. Then, wet development is performed by spreading an appropriate developer solution into the sample. This removes the exposed areas since they become unstable due to the laser (positive photoresist). Next, water is spread to stop the development and the wafer is dried by high speed spinning.

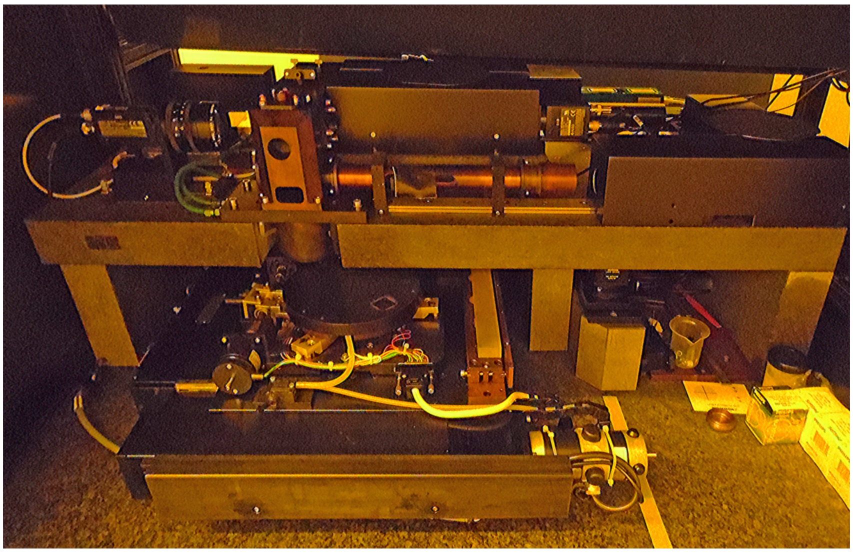

Figure 3.7: DWL 2.0 system.

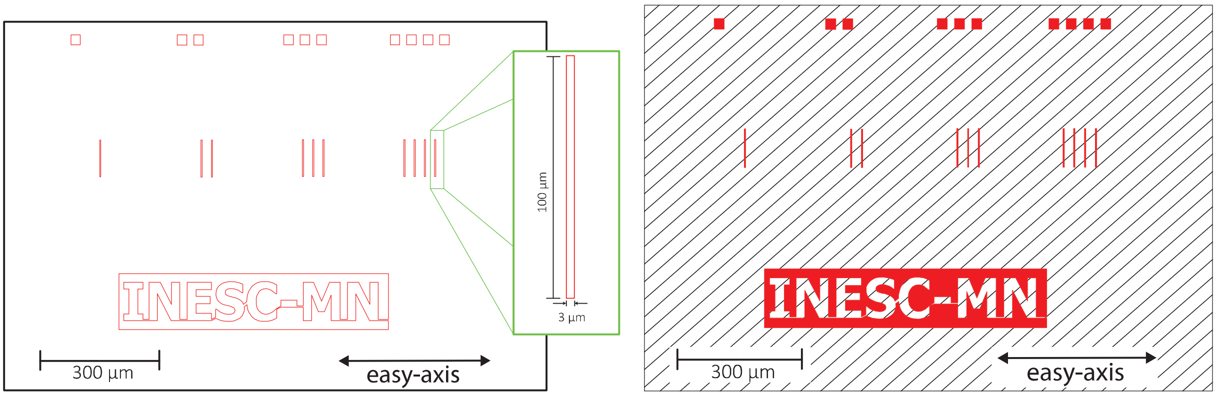

(a) Spinvalve definition AutoCAD mask.

(b) Laser's interpretation of an inverted mask. The solid blocks illustrate the photoresist structures obtained after development.

Figure 3.8: a) AutoCAD mask used to spinvalve definition. b) Representation of how the laser interprets the inverted mask, where the stripes represent the exposed zones.

Physical Etch

At this point, a a physical etch is performed for stack patterning. Physical etch consists in using the kinetic energy of ions to remove atoms from the unpatterned sample. This process is similar to the one described for the stack deposition and is called Ion Beam Milling.

Ion milling is performed in Nordiko 3600, which has an assist gun directed towards the sample, having a similar operation mode to the one described for the deposition gun. The assist gun uses argon (Ar) to create plasma and focus the argon ions into the sample. The parts not protected by the mask, created in the photolithography process, are removed by sputtering.

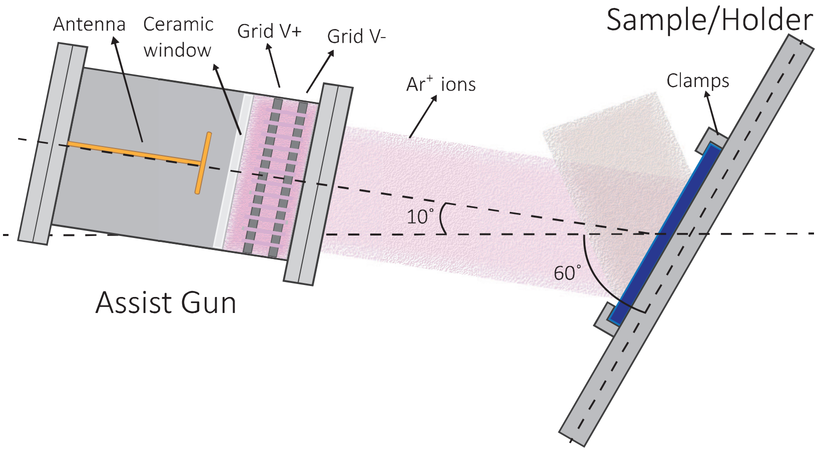

Figure 3.9: Scheme of assist gun from Nordiko 3600.

To avoid trenching and redeposition, physical etch is normally executed with the sample rotated at 60°, corresponding to 70° since the assist gun is tilted 10°. However, in special cases, where material redeposition must to be avoid, for example for MTJ patterning, an etching angle of 40° is used.

In the end of the process, the photoresist mask is removed by immersing it in a photoresist stripper: MicroStrip 3001. After the strip, the sample is rinsed with isopropyl alcohol (IPA) and deionized (DI) water. The defined structures are presented in figure 3.10.

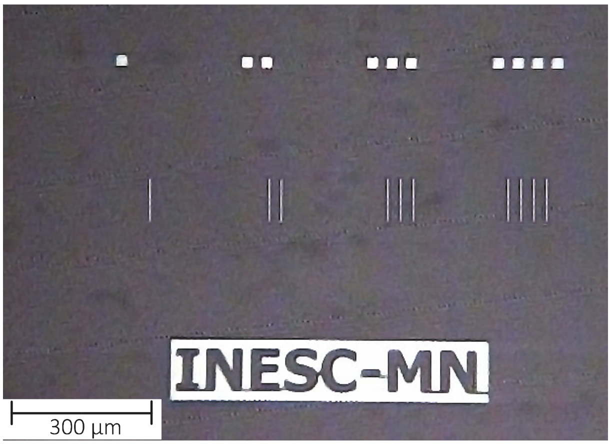

Figure 3.10: Spinvalve sensor defined in the first step.

Parameters	**Nordiko 3600 - Etch process**
Sub rotation (rpm)	30
RF Power (W)	192
Grid 1 Voltage (V)	735
Grid 2 Voltage (V)	-350
Gas Flow [Ar] (sccm)	10
Beam current (mA)	105
Etch Rate (Å/s)	1.05

Table 3.4: Nordiko 3600 etch parameters.

3.1.3 Contact Leads Definition

Contact leads definition process is similar to the one specified for the spinvalves. The major difference is in the process that patterns the contact lead structures.

2nd Lithography

The lithography process of contact leads definition is similar to the previous one. However, there are two differences related to the exposure.

The first, relates to the fact that it is used a non-inverted mask (figures 3.11 a) and b)) that creates cavities. The second difference is referred to the fact that the new exposure must be aligned with the previous defined layer. This alignment is achieved using the position of alignment crosses, which were exposed in the previous layer. These crosses have a specific position in the AutoCAD mask, which are used by the laser software to create an offset to the new layer.

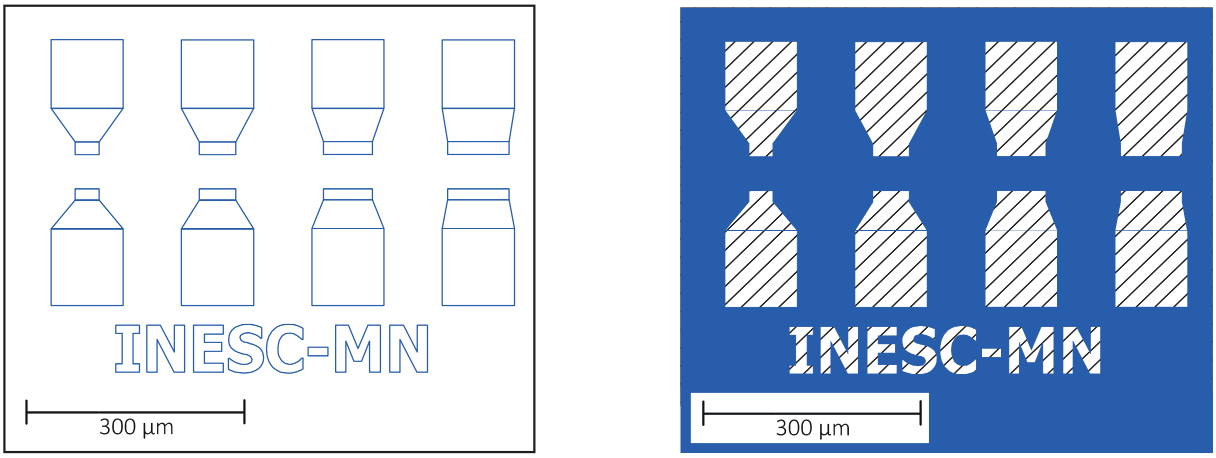

(a) Contact leads layer in AutoCAD mask.

(b) Laser's interpretation of a non-inverted mask.The solid blocks illustrate the photoresist structures obtained after development.

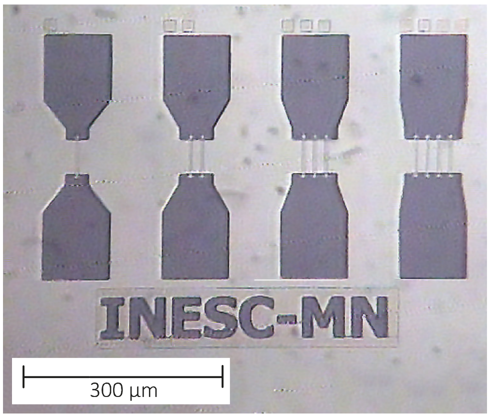

(c) Structures after development.

Figure 3.11: a) AutoCAD mask used for contact leads definition. b) Representation of how the laser interprets the non-inverted mask, where the stripes represent the exposed area. c) Structures obtained after development.

Metallization

After the development of the contact leads' mask, a metallization process is performed at Nordiko 7000. Metallization consists in a soft etch at Module 2, followed by AlSiCu deposition at Module 4 and finishes with TiW(N) at module 3, to protect the aluminum layer from physical and chemical damage.

	Ar/N_2 flow (sccm)	**Pressure (mTorr)**	**Power (W)**	**Deposition Rate ($Å/s$)**
Module 2	50/-	3	RF 40/60	-
Module 4	50/-	3	DC 2000	37.5
Module 3	50/10	3	DC 500	1.25

Table 3.5: Nordiko 7000 operation parameters for the Metalization process.

At the end of this process, sample is deposited with AlSiCu $3000\,Å$ + TiW $100\,Å$. The contact leads structures are obtained by a process called lift-off.

Lift-Off

To execute a lift-off, the sample is, once again, immerse in MicroStrip 3001 solution and placed in a hot bath, around $65\,^{\circ}\mathrm{C}$, with ultrasounds. Ultrasounds help to damage the top layer so that the Microstrip 3001 solution can reach the photoresist at the bottom and dissolve it while the high temperature helps the dissolution process. In the end, only the metallic layers deposited in the cavities remain (figure 3.12).

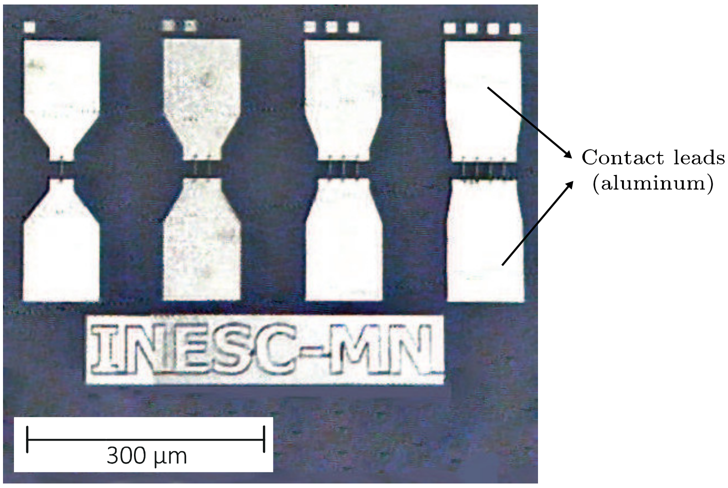

Figure 3.12: Contact leads defined after aluminium lift-off.

3.1.4 Contact Pad Definition

To protect both spinvalve and metallic layer from physical and chemical damage, an oxide layer of Al_2O_3 is deposited over the sample. However, to be able to measure the sensor afterwards, this layer needs to be patterned to open cavities in the pads region.

3rd Lithography

In this lithography step, an inverted mask is used, as previously for spinvalve definition. This means that the structures defined in AutoCAD remain after the development. These structures are squares that are placed over the contact leads, which, after Al_2O_3 deposition and lift-off, define cavities in those same places.

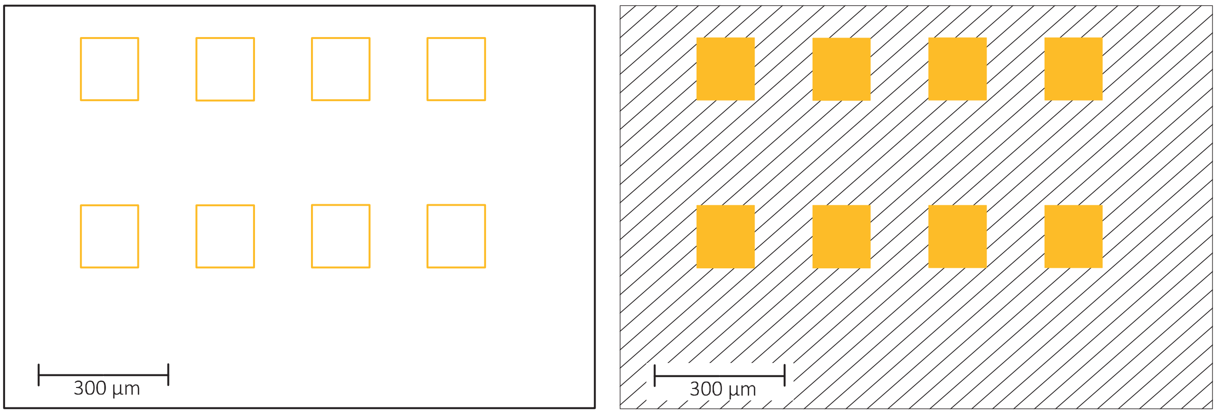

(a) Contacts layer in AutoCAD mask.

(b) Laser's interpretation of a inverted mask.The solid blocks illustrate the photoresist structures obtained after development.

Figure 3.13: a) AutoCAD mask used for contacts definition. b) Representation of how the laser interprets the inverted mask, where the stripes represent the exposed areas.

Aluminium Oxide Deposition

Aluminum oxide is deposited in UHV II machine. The physical process is identical to the one described for Nordiko 7000 – Magnetron RF Sputtering. The machine is composed by a single chamber, which means that to load/unload samples it must be totally vented. Thus, to achieve an optimal pressure of $3 \times 10^{-7}\,\mathrm{Torr}$, the machine must be pumped for $10\,\mathrm{h}$. In this machine, the target is made of ceramic Al_2O_3.

The patterned structures are protected with a $2000\,\text{Å}$ thick layer of Al_2O_3. With a deposition rate of $11\,\text{Å}/\mathrm{min}$, this takes approximately 3 hours to be completed.

Machine	**Ar flow (sccm)**	**Pressure (mTorr)**	**RF Power (W)**	**Deposition Rate** (Å/min)
UHV II	45	2.6	200	11

Table 3.6: UHV II operation parameters for the Al_2O_3 deposition.

Lift-Off

Finally, a lift-off is performed to remove the photoresist and open cavities to be able to measure the sensors. This lift-off is accomplished as for the contact leads definition. However, since Al_2O_3 is harder than aluminium, this step takes more time to be completed.

3.1.5 Annealing

Annealing is a thermal and magnetic process that allows to achieve the optimum proprieties of the sensors. It consists on heating the samples above the Néel Temperature, at which the antiferromagnetic layer becomes paramagnetic. Then, a magnetic field is applied, defining the new alignment direction for the magnetic moments when the sample is cooled down.

The top-pinned spinvalves with a MnIr pinned layer, used in this work, don't require annealing since the easy-axis of the pinned layer is defined during the deposition process. However, during the fabrication, some steps can destroy this configuration due to the high temperatures involved. In this thesis, overheating of the sample was observed in AlN and $Al_{98.5}Si_{1.0}Cu_{0.5}$ depositions, which could reach temperatures above the blocking temperature inside the machine. Also, this annealing setup ensures that all the spinvalves levels are totally aligned with each other.

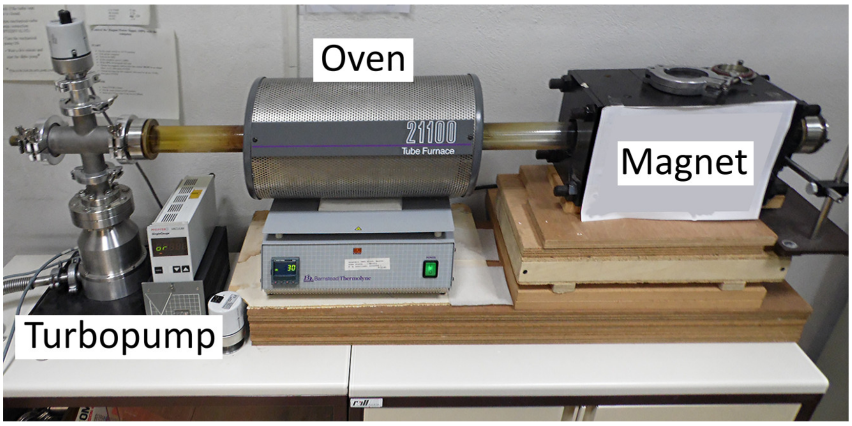

Figure 3.14: Annealing setup from INESC-MN.

The annealing is performed in a setup composed by a rough and turbo molecular pumps, a quartz tube, an oven, a permanent magnet and a metallic holder attached to a quart rod inside the tube (figure 3.14). After the samples are placed and closed inside the quartz tube, they are pulled into the furnace. Then, the rough pump is turned on to achieve a pressure close to 1×10^{-3} Torr. When this pressure is obtained, the turbo molecular pump is initiated to pump the system until a pressure close to 1×10^{-6} Torr. After this optimal pressure is achieved, the temperature increases at $5\,^{\circ}\mathrm{C}/\mathrm{min}$ until the desired temperature is achieved. In this work, it was defined to be $250\,^{\circ}\mathrm{C}$, which is higher than the blocking temperature for MnIr [81]. This is maintained during 20 minutes, and then the magnetic field is applied by pulling the samples into the permanent magnet. With the samples inside the magnet, the temperature naturally decreases until it meets the room temperature.

3.1.6 Dicing

Some characterization setups, as for example the noise setup, require that the sensor is integrated in a chip. For this reason, and also to be able to handle sensors individually, the sample needs to be precisely diced in individual dies. This dicing process is performed in the Disco DAD 321.

First, the sample is protected against dust particles created during the dicing. This is accomplished by coating the sample with photoresist. This $1.5\,\mu\mathrm{m}$ thick layer protects the structures below and is easily removed with acetone.

Disco DAD 321 requires to perform a SETUP step to calibrate the blade height with respect to the table. Then, the protected sample is mounted on a metallic frame using a $150\,\mu\mathrm{m}$ thick photosensitive self-adhesive tape. The frame is placed and centered fixed in the vacuum chuck by vacuum and magnets that attract the metallic frame.

The *Device Data* menu, allows to change some configurations of the cut that include: vertical and horizontal steps, work area shape and dimensions, blade height, blade rotation and dicing speed. Vertical and horizontal steps correspond to the die sizes. Work area shape can be *Round*, for 6 inch wafers, or *Squared*, for small samples. The work area size should be defined always larger than the real sample size to ensure that the blade starts the cutting laterally and not over the surface, which would damage the blade. Also, centering the sample in the chuck is important because the work area is defined from the center of the same. Blade height is defined as 0.09 mm which means that 60 µm of tape are diced, ensuring that the sample is fully cut. Finally, rotation speed is defined as 30 krpm while the cut speed varies with the substrate material. For glass 0.5 mm/s ensures a smooth cut without the shattering of the sample, while for silicon this can go up to 20 mm/s.

Dicing is performed in *Semi-Auto* mode, which means that the first cut is chosen by the user and then all the remaining cuts in that direction are made automatically considering the steps defined in *Device Data*. However, before dicing, the sample needs to be aligned, which is performed using the border of the dies (not the sample). Finally, the dicing process can start. After the first direction is concluded, the user rotates the sample 90° and chose the starting point for the next dicing sequence.

In the end, the sample is removed and placed under UV-radiation, helping to weaken the photosensitive glue.

Before the machine is turned off, a new setup should be performed to determine the amount of blade consumed during the dicing process. This is then used to determine the new blade diameter, which is fundamental for the next blade height calibration.

3.1.7 Wire Bonding

Wire bonding allows to integrate sensors on a chip by connecting the contacts of the sensors to the contacts of the chip with 45 µm thick aluminum wire. This process is performed in K&S 4526 Manual Bonding system, and uses the wedge bonding method, which consists on using force and ultrasonics vibrations to bond the wire to the surface.

Three paramaters are used to configure the bonding process, namely: *Power* (1.3 W to 2 W), *Time* (10 ms to 100 ms), and *Force* (10 g to 160 g).

The bonding *Power* parameter corresponds to the amount of ultrasonic vibration energy applied to the bond, during a certain time defined by the *Time* parameter. Finally, the force parameter configures the amount of force applied to the bond by the counterweights on the bonding head armature.

3.2 Characterization Methods

Characterization techniques are important not only after the fabrication process, which verifies if the sensor achieved the desired parameters, but also the whole process to control and monitor the proprieties and to ensure the progress during the fabrication. This section presents four relevant characterization techniques used in this work.

3.2.1 Profilometer

Profilometer was used to measure the topography of the samples, in a Dektak 3030ST, which has a thicknesses resolution of 200 Å.

A diamond-tipped stylus rides over the sample's topography, which causes it to move vertically. This vertical movement is translated into electrical signals by an LVDT (linear variable differential transformer) mechanically coupled to the stylus [82].

In this thesis, the profilometer was essentially used to measure thicknesses of thin films to determine the deposition rate of new targets (tantalum and nickel iron) and aluminium nitride along the whole process.

3.2.2 Atomic Force Microscopy

Another system able to measure the topography of samples is the Atomic Force Microscope (AFM). This microscopy technique is a high-resolution type of scanning probe microscope, with resolution of few angstrom, capable to measure the surface roughness of materials [83].

AFM system uses a cantilever with a tip with radius of curvature on the order of nanometers, which scans an area of the sample and uses the cantilever deflections, caused by mechanical forces, to measure its topography. In this case, these deflections are caused by van der Waals forces. This is achieved by using a laser that is reflected on the top surface of the cantilever to a matrix of photodiodes. When the cantilever deflects, the beam reflection angle also changes which can be converted into topographic characteristics of the sample.

Three modes can be used to measure the topography: Contact Mode, Tapping Mode and Non-contact Mode. The AFM measurements in this thesis were performed in Digital Instruments Dimension 3000 system in Tapping Mode, since it improves the resolutions.

In Contact Mode, the tip is dragged over the surface and the topography is measured directly by the cantilever deflection. This mode induce high lateral forces in the sample and on the tip. The Tapping Mode solves this issue by oscillating the tip with a high frequency (order of kHz) over the surface, using a piezoelectric crystal, which corresponds to the resonance frequency of the tip. The interaction forces between the surface and the tip change the amplitude of oscillation, which is converted to determine the surface topography. The Non-contact Mode is similar to the Tapping Mode, however, the tip never touches the surface. Instead, it hovers from 50 Å to 150 Å above the sample. Thus, the deflection is caused by van der Waals forces.

3.2.3 Magnetotransport

Magnetotransport characterization allows to study how the electrical resistance of the magnetoresistive sensors changes with the application of a magnetic field. This field is usually applied in the easy-axis direction of the pinned layer.

Two different setups are available at INESC-MN. The first, illustrated in figure 3.15 a), measures magnetotransport curves within a magnetic field range of 400 Oe, while the second, shown in figure 3.15 b), is limited to 140 Oe.

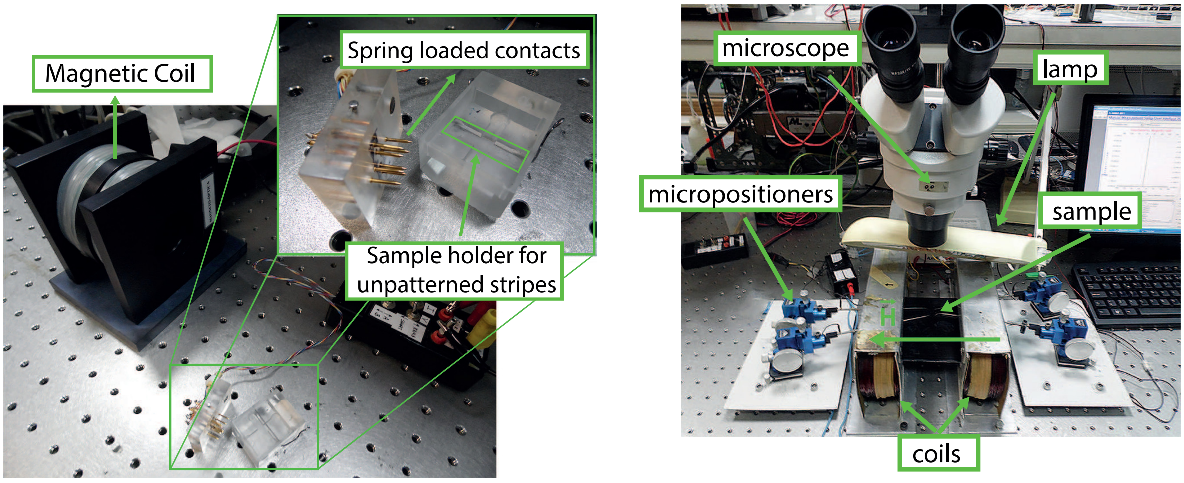

(a) 400 Oe Magnetotransport setup

(b) 140 Oe Magnetotransport setup

Figure 3.15: 400Oe and 140Oe magnetotransport setups at INESC-MN.

The 400 Oe setup is limited to test the R(H) curve to unpatterned sensors. It is composed by a Helmholtz coil, a measurement container, two current sources and one voltmeter. The container comprises a bottom part, where sample stripes can be placed in one of two perpendicular directions, enabling measurements with the field parallel to the easy-axis or to the hard-axis; and a top part that incorporate 8 probes (four for each direction), which uses a four probe method to measure the resistance of the sample. In this method, the two outer probes apply a current to the sample, while the two inner probes are used to measure the voltage drop. This four probe method is used because it allows more accurate measurements than the two probe method, since it eliminates unwanted voltage drop caused by contact resistance between probes and the sample. The Helmholtz coil is powered by a current source that can deliver a DC current up to 4 A . The measurements are performed by introducing the container in the center of the Helmholtz coil, where the magnetic field is screened from −400 Oe to 400 Oe. This range is useful to measure the exchange field of spinvalves without SAF, which presents values lower than 400 Oe.

The 140 Oe Setup is composed by two Helmholtz coils, four micropositioners and use the same current sources and voltmeter as the previous setup. The sample is placed between the two coils, which ensures that a magnetic field from −140 Oe to 140 Oe is applied to the sample. The micropositioners grant a resolution of approximately 10 µm and are equipped with tungsten needles that supply current to the sensor's contact pads and measure the voltage difference.

Both setups are connected to a computer through GPIB bus that allows to a software to control the measurements sequence. In each step, magnetic field is set to a specific value, and then the voltage is measured, to calculate the resistance and GMR ratio.

3.2.4 Noise

The noise characterization of a sensor is achieved by supplying a current to the sensor and measure the voltage fluctuations. This signal is then converted using a Fast Fourier Transform (FFT) algorithm to obtain the Frequency Domain of the signal, which gives information about the voltage level for each frequency within the range.

This characterization is performed at a noise setup that was developed at INESC-MN and is composed by: a primary shielded box (figure 3.16 a)), one amplifier with its power supply, a second shielded box, a voltmeter and a spectrum analyzer (figure 3.16 b)).

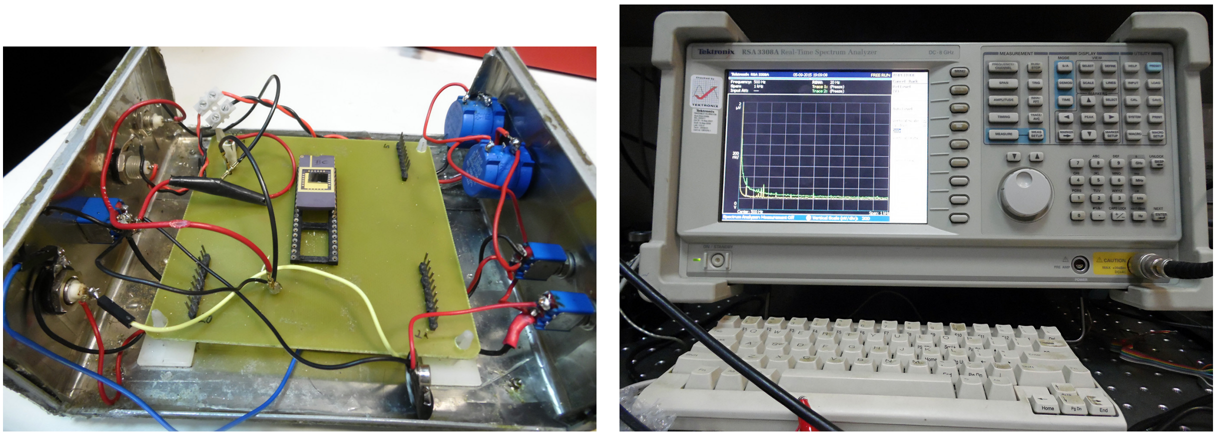

(a)

(b)

Figure 3.16: a) Primary Shielded box b) Tektronik RSA3308A spectrum .

The primary box contains the circuit that biases the sensor and extract the output voltage. A chip socket with 40 connectors allows to insert the chip integrated with the sensors and choose which one to measure. Two potentiometers connected in series with the sensor allow to adjust the voltage and current supplied to the sensor by varying its resistance. One potentiometer has a range of $0\,\mathrm{k\Omega}$ to $100\,\mathrm{k\Omega}$ and is used for rougher adjustments while the other has a range of $0\,\mathrm{k\Omega}$ to $10\,\mathrm{k\Omega}$ and is used for finer tuning. A $9\,\mathrm{V}$ battery supplies the sensor and the two potentiometers. Finally, three switches allow to: turn ON/OFF the power supply, short circuit the sensor to protect from current peaks (mainly caused by a power supply state change), and introduce an amperemeter to the circuit or, in certain cases (where the resistance of the sensor is on the order of the potentiometers' resistance), introduce a large resistance.

Since the goal is to measure voltage fluctuations in the sensor, it is necessary to use a low noise linear amplifier. In the measurements performed in this thesis, it was used a Stanford Research Systems (SNR) SIM910 amplifier, which have a maximum gain of 40 dB, corresponding to an amplification of the signal 100 times, an input resistance of $100\,\mathrm{M\Omega}$ and an intrinsic noise level of $4\,\mathrm{nV}/\sqrt{\mathrm{Hz}}$.

To acquire the signal from the amplifier, it was used a Tektronix RSA3308A real time spectrum analyzer with a frequency range from DC to $8\,\mathrm{GHz}$ and a noise level of $90\,\mathrm{nV}/\sqrt{\mathrm{Hz}}$. This high noise level from the spectrum analyzer motivates the use of the amplifier, so that the noise of the sensor can overcome the noise from the spectrum analyzer.

For each sensor, four measurements are necessary. The first two are calibrations performed with no bias on the sensor performed with different frequency ranges: 0 kHz to 1 kHz (with a resolution bandwidth of 2 and 100 averages) and 0 kHz to 100 kHz (with a resolution bandwidth of 200 and 1000 averages). The last two measurements are executed with the sensor biased and within the same ranges defined previously.

The calibration allows to measure the intrinsic noise level of potentiometers and the amplifier, which is then used to remove this contribution from the biased measurement. For a better comprehension, the circuit in figure 3.17 is analysed based in the work of Ricardo Ferreira [78]. This scheme represents the noise circuit with the addition of voltage sources that represent the intrinsic noise of each component. Specifically, the noise sources are V_{dut}, V_p and V_{amp}, corresponding to noise voltage from the sensor (Device Under Test), potentiometers and amplifier, respectively.

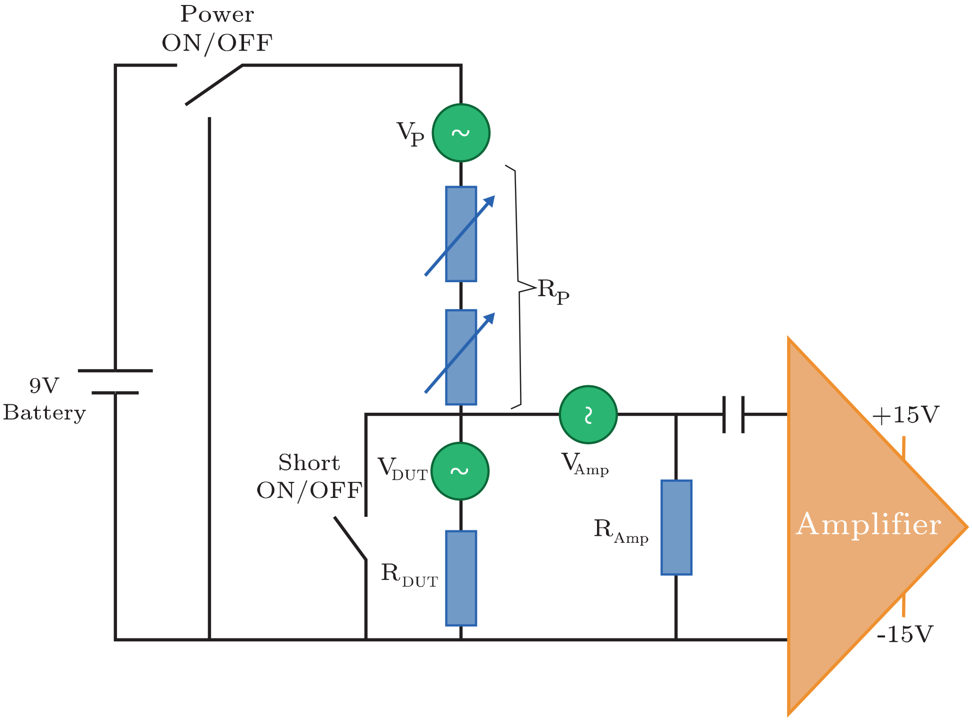

Figure 3.17: Schematic representation of noise setup used in this thesis. Adapted from [26].

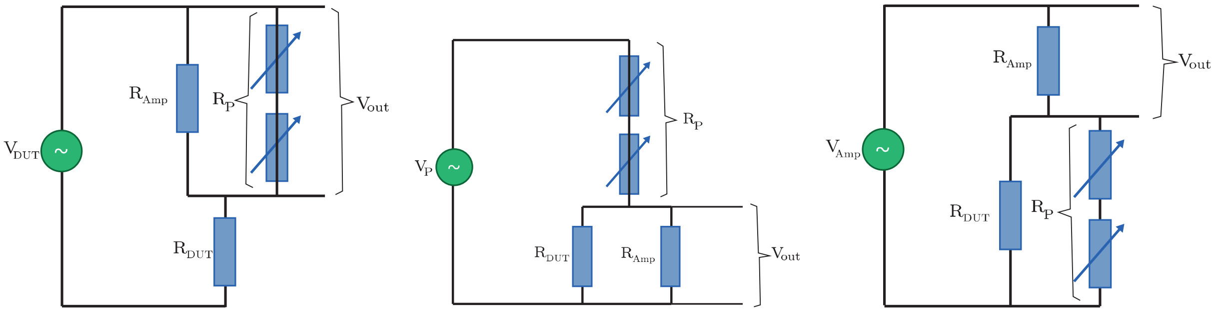

(a) V_{DUT} source (b) V_P source (c) V_{AMP} source

Figure 3.18: Circuits representation for each voltage source considered for Superposition theorem.

Considering the superposition theorem (figure 3.18), an expression relating the output measured in the amplifier entrance with all the voltage noise sources can be obtained [26, 78].

$$
\begin{aligned}
V_{out}^2 &= V_{DUT}^2 \left(\frac{R_p \parallel R_{amp}}{R_{DUT} + R_p \parallel R_{amp}} \right)^2 \\
&\quad + V_p^2 \left(\frac{R_{DUT} \parallel R_{amp}}{R_p + R_{DUT} \parallel R_{amp}} \right)^2 \\
&\quad + V_{amp}^2 \left(\frac{R_{amp}}{R_{amp} + R_p \parallel R_{DUT}} \right)^2 .
\end{aligned}
\tag{3.1}
$$

As mentioned, it is necessary a calibration measurement where no voltage is applied to the sensor, which means that $I = 0\,\mathrm{A}$ and so the noise from the sensor comes only from its thermal term (equation 2.60). So $V_{DUT} = V_{th}$, giving:

$$
\begin{aligned}
V_{out}^2|_{I=0} \equiv V_0^2 &= V_{th}^2 \left(\frac{R_p \parallel R_{amp}}{R_{DUT} + R_p \parallel R_{amp}} \right)^2 \\
&\quad + V_p^2 \left(\frac{R_{DUT} \parallel R_{amp}}{R_p + R_{DUT} \parallel R_{amp}} \right)^2 \\
&\quad + V_{amp}^2 \left(\frac{R_{amp}}{R_{amp} + R_p \parallel R_{DUT}} \right)^2 .
\end{aligned}
\tag{3.2}
$$

Combining both equations, V_{out}^2 can be defined as:

$$
V_{out}^2 = V_0^2 - V_{th}^2 \left(\frac{R_p \parallel R_{amp}}{R_{DUT} + R_p \parallel R_{amp}} \right)^2 + V_{DUT}^2 \left(\frac{R_p \parallel R_{amp}}{R_{DUT} + R_p \parallel R_{amp}} \right)^2 . \tag{3.3}
$$

This equation reveals that with the thermal term, which can be retrieved from equation 2.56, and the calibration measurements, the total noise from the sensor (V_{DUT}) can be obtained.

Chapter 4

Results

The first step in this work was the optimization of a SV top-pinned stack. The influence of each layer in the spinvalve's characteristics, specifically MR, coercivity and fringe field, was studied by depositing stacks with different layer's thicknesses. However, due to problems in Nordiko 3600's deposition gun, this work was not completed. Therefore, the targets in Nordiko 3000 were changed to enable deposition of SV stacks. Nevertheless, this work developed the knowledge about spinvalve operation and magnetic characteristics.

To change the space between the packaged spinvalves and, therefore, the magnetic interactions, different reliable materials, requiring good insulator characteristics and low surface roughness, were studied.

One of the main concerns about packaged spinvalves is the reduced area available for the metallization process. Therefore, a study was performed concerning the electrical properties of systems with varied number of packaged spinvalves.

An AutoCAD mask was created, attending the required studies for the noise measurements, and each layer was presented in previous chapter, in figures 3.8, 3.11, and 3.13. The mask is composed by singular and in-plane parallel connected spinvalves, to compare the improvement obtained from parallel packaged spinvalves and parallel in-plane spinvalves.

After executing the microfabrication process described in 3.1, magnetotransport and noise measurements were performed to investigate the performance of packaged spinvalves.

Finally, the elements that influence the sensitivity in the packaged system were explored, which lead to important conclusions and ideas for a continued work.

4.1 Spacer material

The first step in this thesis consists in finding the optimal material to use as a spacer. The characteristics that define the ideal material are the low surface roughness and being an insulator. Roughness has a major impact on spinvalves since it influences the texture of the deposited thin films, which, as explained in section 2.2.2, affects several properties of spinvalves as MR, coercivity, exchange field and fringe field.

Lastly, having an insulator spacer means that the current is confined in the spinvalve sensor contributing to the scattering and thus for an effective magnetoresistance effect.

At INESC-MN, three different insulator thin films can be deposited: aluminium oxide (Al_2O_3), silicon nitride (Si_3N_4) and aluminium nitride (AlN). As mentioned in chapter 3, Al_2O_3 is deposited in UHV II, Si_3N_4 is deposited in Electrotech, and AlN in Nordiko 7000. Both materials are widely used in electronics for their goods properties as insulators and thermal and corrosion resistance. The lack of a load chamber in UHV II turns Al_2O_3 an impractical choice for the work, due to the long time (10 hours) needed to achieve the optimum pressure for the process.

As explained in section 2.2.2, the buffer, where the spinvalve stack is deposited, influences the crystalline growth and therefore the magnetic properties of the spinvalve. Hence, to study how these two materials influence the magnetotransport properties of a spinvalve, two groups of samples were deposited and measured, and are illustrated in figure 4.1.

(a) Spinvalve stack on top of a Si_3N_4 layer.

(b) Spinvalve stack on top of a AlN layer.

Figure 4.1: Representation of the samples used to study the effect of different spacer materials on spinvalve properties.

The first group allows to study the influence of Si_3N_4 and consists in three samples with the same stack deposited on top of different substrates. One sample is the reference sample, having the spinvalve stack deposited directly in the Si/SiO_2 (thermal oxide) sample, and the other two are composed by the same stack deposited on top of 1500 Å and 2500 Å of Si_3N_4. The results are represented in figure 4.2 and table 4.1.

The approach is similar for the AlN group. It consists in three samples with 1200 Å of AlN deposited with a RF power of 0.3 kW, 0.5 kW and 1 kW. The results are represented in figure 4.3 and table 4.2.

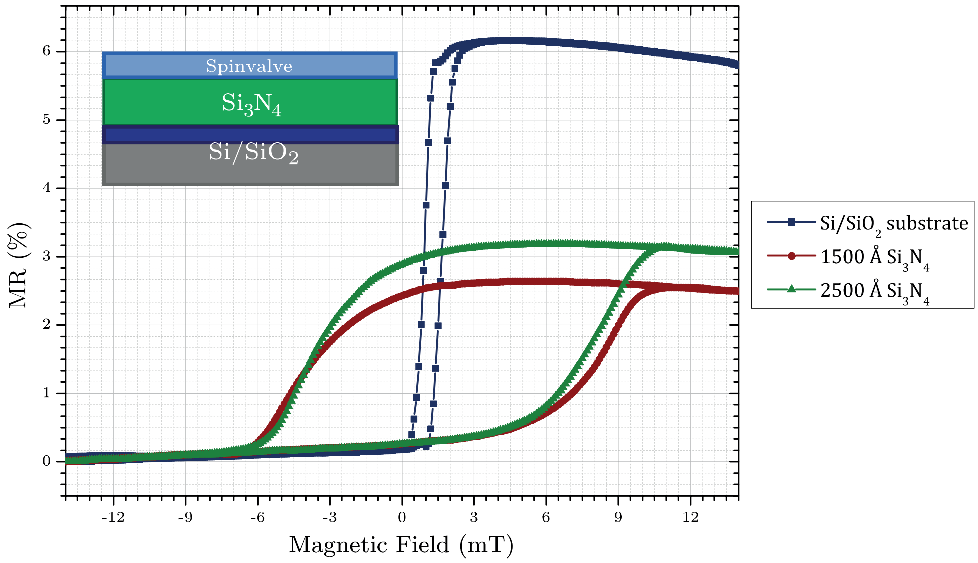

Figure 4.2: Magnetotransport curves for the Si_3N_4 substrates study.

Substrate	**MR (%)**	**$\mu_0 H_f$ (mT)**	**$\mu_0 H_c$ (mT)**
Si/SiO_2 substrate	6.2	1.3	0.4
1500 Å **Si_3N_4**	2.6	1.9	5.9
2500 Å **Si_3N_4**	3.2	2.0	5.6

Table 4.1: Magnetic properties values for the Si_3N_4 study.

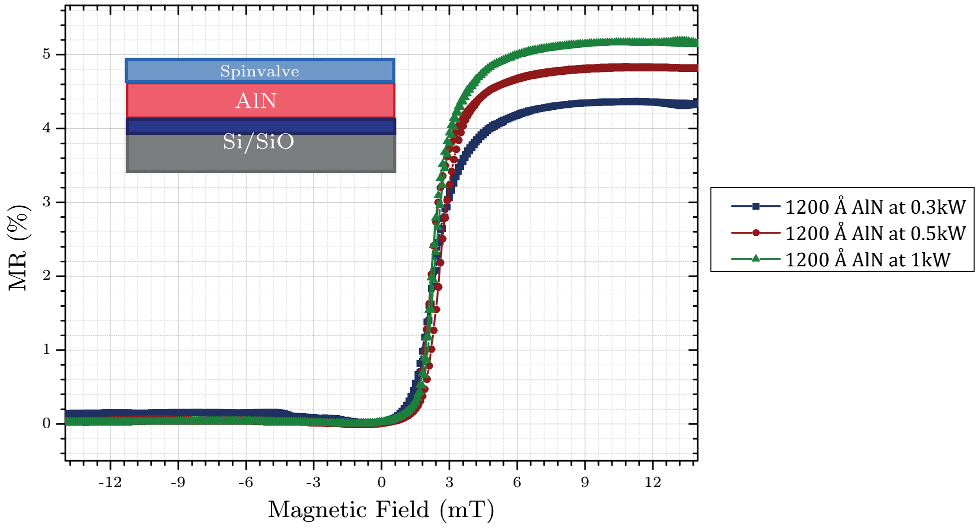

Figure 4.3: Magnetotransport curves for the AlN substrates study.

These results reveal that the Si_3N_4 substrate has a negative influence in the magnetic properties of the spinvalve. The magnetoresistance for the stacks deposited in the Si_3N_4 buffer is nearly half of the reference stack and the coercivity become one order of magnitude higher. This is expected because PECVD deposition creates highly columnar growth, which has a direct impact on SV films. Contrastingly, the stacks deposited on top of AlN buffer not only maintained their coercivity and fringe field properties

Substrate	**MR (%)**	**$\mu_0 H_f$ (mT)**	**$\mu_0 H_c$ (mT)**
1200 Å **AlN at 0.3kW**	4.4	2.4	0.05
1200 Å **AlN at 0.5kW**	4.8	2.5	0.18
1200 Å **AlN at 1kW**	5.2	2.4	0.07

Table 4.2: Magnetic properties values for the AlN study.

but also show an improvement in the MR with increasing the RF power of the AlN deposition from 4.4% (0.3 kW) to 5.2% (1 kW).

Based on these results, the material chosen to be used as spacer material was the Aluminium Nitride.

However, before starting to microfabricate packaged spinvalves, was investigated spacer's thickness influence in the spinvalve stack. This study was conducted by depositing two packaged spinvalve systems with a AlN spacer, as illustrated in figure 4.4, with 4 different thicknesses: 100 Å, 300 Å, 500 Å and 700 Å.

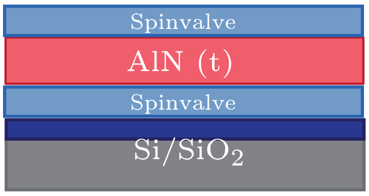

Figure 4.4: Representation of the packaged system deposited to study the spacer's thickness effect, by using different thickness (t) of AlN.

In figure 4.5, is observed that with the increase of the spacer's thickness a step starts to emerge in the magnetotransport curve. The origin of this step is a attributed to the roughness of the AlN spacer, which increases the Néel coupling and consequently shifts the curve of the spinvalve on top of it. Therefore, when the number of spinvalves packaged increase, the cumulative aspect of roughness have a negative influence in the magnetotransport curve of the packaged system. Thus, this effect needs to be ameliorate forthwith. To accomplish this, an etch at Nordiko 3600 was performed. This etch, which is different from the one described at section 3.1.2, was executed with an angle of 30° and during 90 s, being usually called soft-etch. Due to its small angle and short time, this type of etch is not used to pattern structures but instead is mainly used as a cleaner or smoothing process of samples's surfaces.

To investigate the outcome of this process, two samples were deposited with 800 Å of AlN, performing a soft-etch in one. Then, the roughness of these samples was measured in AFM and these results are presented in figure 4.6.

The AFM measurements confirmed that the soft etch successfully improved the roughness of the AlN film, reducing the root mean square (RMS) of the profile's height from 1.6 nm to 0.29 nm. Furthermore, this result is praised considering that the roughness of a silicon wafer with thermal oxidated SiO$_2$ extends from 0.1 nm to 0.3 nm [84–86].

To further validate this result, one spinvalve stack was deposited on top of three different substrates: Si/SiO$_2$ and 800 Å of AlN with and without soft-etch. The results are presented in figure 4.7 and table 4.3

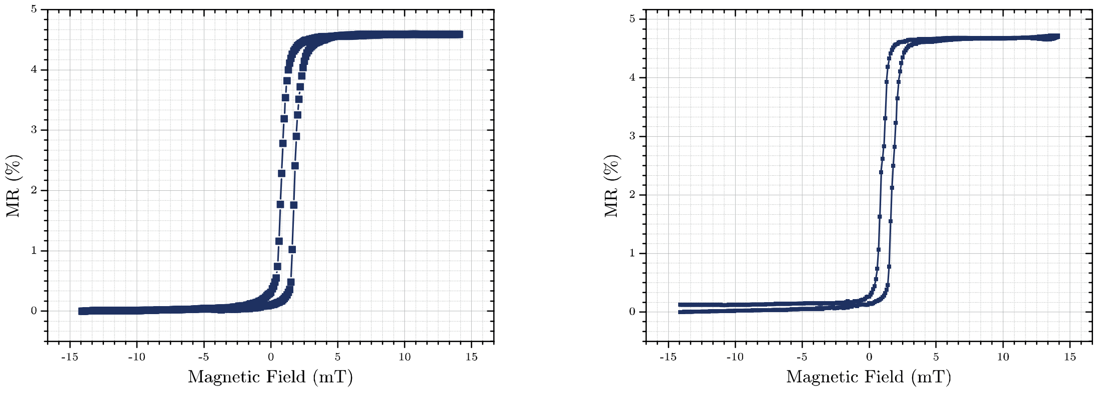

(a) 100 Å (b) 300 Å

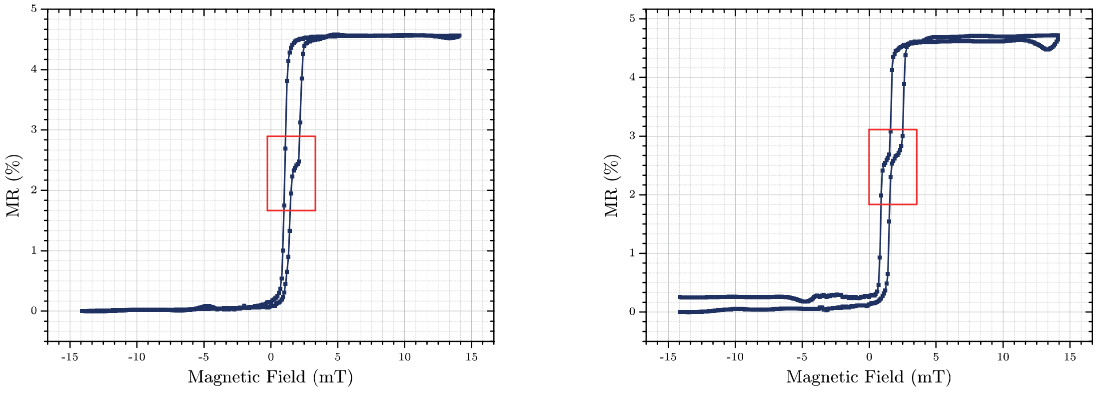

(c) 500 Å (d) 700 Å

Figure 4.5: Magnetotransfer curves of two spinvalve stacks packaged with different AlN thicknesses.

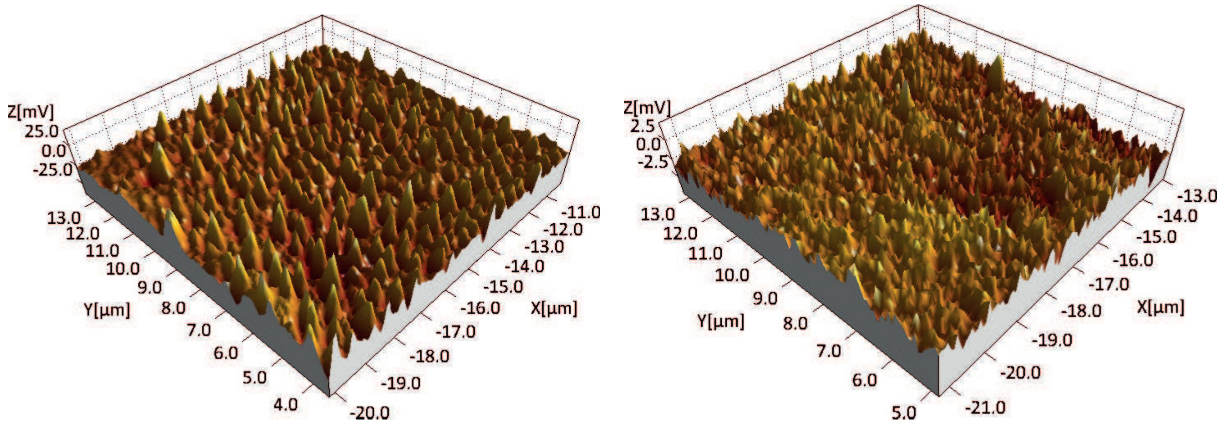

(a) Sample without soft-etch. The roughness is 1.6 nm (b) Sample with soft-etch. The roughness is 0.29 nm

Figure 4.6: Topographic profile obtained from AFM measurements for 800 Å thick AlN films. The roughness was measured using the *Rq* parameter, which represents the root mean square of the profile's height, on *SPIP 6.4.2* software. Notice that the *z* scale from the sample without soft-etch (a)) is ten times bigger than the scale from the sample with soft-etch (b)).

and shows that the shift of the curve for the sample with 800 Å of AlN soft-etched is approximately equal to the sample composed by Si/SiO$_2$, thus validating the soft-etch smoothing approach.

Substrate	**MR (%)**	**$\mu_0 H_f$ (mT)**	**$\mu_0 H_c$ (mT)**
Si/SiO$_2$ substrate	4.5	1.86	0.45
800 Å **AlN without soft-etch**	4.8	2.94	0.56
800 Å **AlN with soft-etch**	4.6	1.88	0.39

Table 4.3: Magnetic properties values for samples used in the soft-etch study.

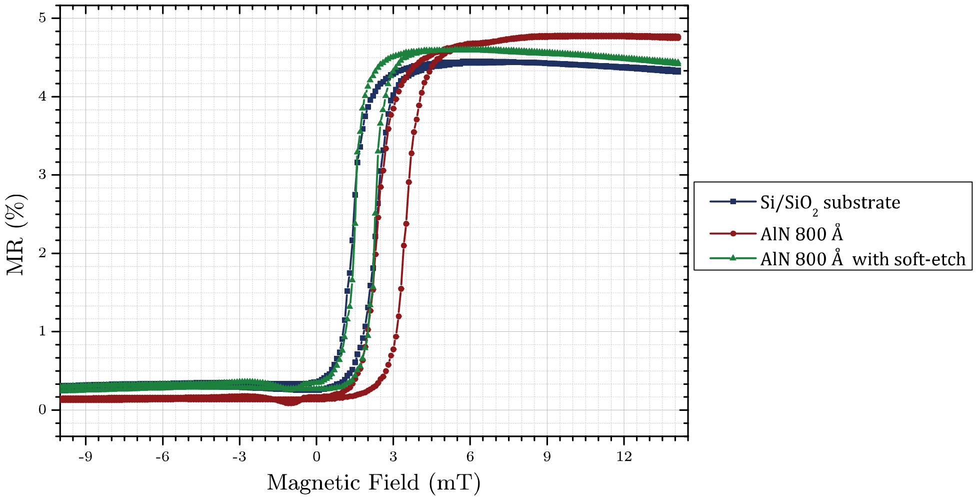

Figure 4.7: Magnetotransport curves for the three samples used for the soft-etch study.

4.2 Electrical Contact

Before performing noise measurements, it is necessary to ensure the electrical contact between the spinvalves that compose the vertical package.

When a single spinvalve is microfabricated, the metallization process deposits aluminium on the top and on the sides of the spinvalve. However, with vertical packaging this does not occur since the top surface is unavailable, as illustrated in figure 4.8.

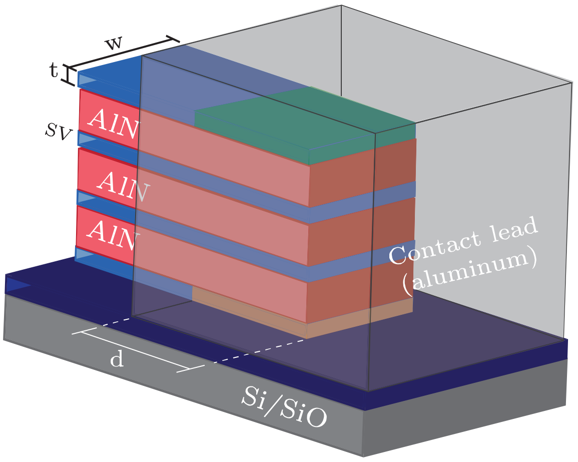

Figure 4.8: Representation of the contact areas for singular and packaged spinvalves. t represents the thickness of the spinvalve, w the width, and d the spinvalve length covered by the contact lead. The green area represents the available area on singular SVs, while the orange one represents it for package SVs.

This fact can be an issue because, not only, the top surface has higher probability of Aluminium atoms' deposition on it, but also because its area is approximately 50 times bigger than the side area (considering that the thickness of the spinvalve is 250 Å, the width is 3 µm and the length of spinvalve covered by the aluminium is 10 µm, the total contact area for a singular SV is 30.575 µm^2 while for a SV on a packaged system is is 0.575 µm^2). To test if side area is enough to assure the electrical contact between all the levels of the spinvalve package, their electrical resistance are compared.

In a parallel configuration, where all elements are equal, the total resistance (R_t) decreases with $\frac{1}{M}$, where M is the number of elements. Therefore, if the electrical contact is being ensured by the side area, then, the same $R_t \propto \frac{1}{M}$ behaviour should be observed in the packaged spinvalves. Thus, the resistance of six samples with different number of packaged spinvalves was measured and the results are presented in figure 4.9.

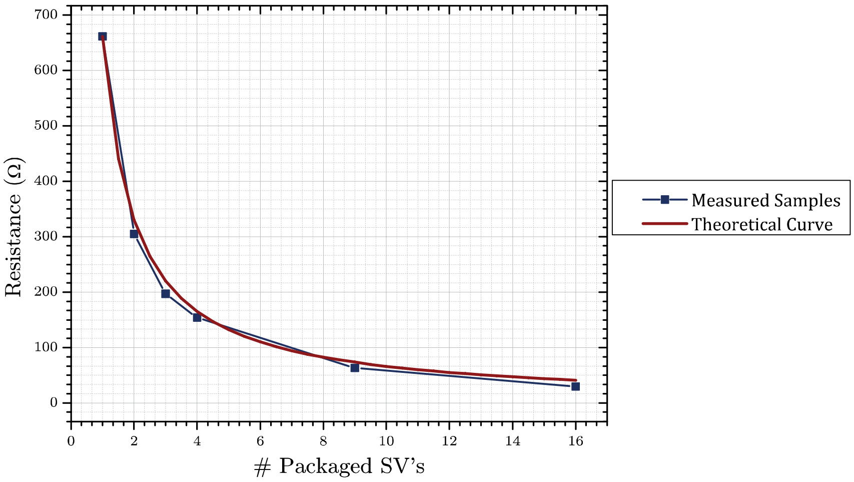

Figure 4.9: Representation of the resistance variaton with the number of packaged spinvalves. Notice that the theoretical curve was plotted by considering the experimental resistance for one spinvalve as the theoretical resistance.

The results evince a good agreement between the theoretical and experimental values, revealing that, in spite of being a small area, the side area is enough to allow the electrical contact between the various levels that compose the packaged system.

4.3 Noise and Detectivity

To study the effects of the spinvalve's vertical packing in the noise and detectivity, three samples were microfabricated. The first consists in a individual stack (SV1889) that is be used as reference (sample R) and the other two consist in four spinvalve stacks (SV1889) packed, one without spacer (sample NS) and the other with 700 Å of AlN (sample S).

The noise was measured in five different structures. The first three consist in an individual spinvalve structure in each sample mentioned above (structures R1, NS1 and S1) and the other two consist in parallel structures (in the plane) for the reference sample (structure R4) and for the sample without spacer (sample NS4). These structures are represented in figure 4.10.

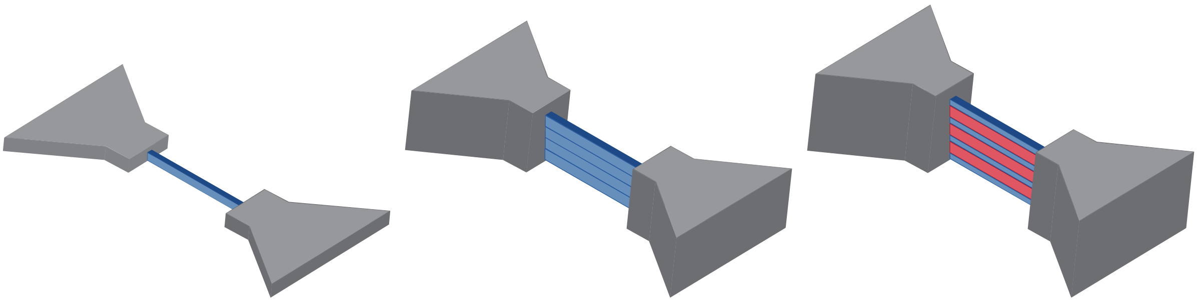

(a) R1 structure, representing an singular spinvalve. Blue represents a spinvalve.

(b) NS1 structure, representing a packaged system with four spinvalve, without spacer.

(c) S1 structure, representing a packaged system with four spinvalve, with 700 Å of AlN.

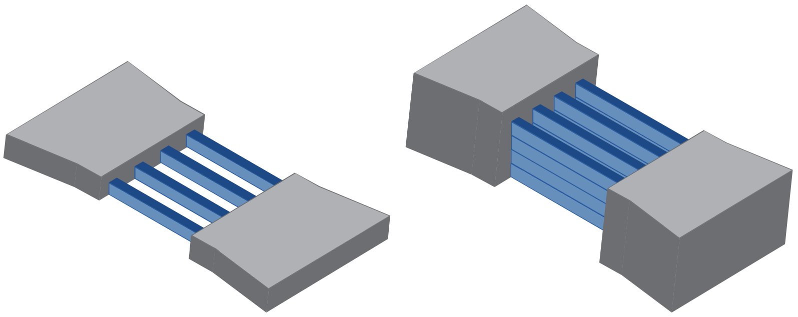

(d) R4 structure, representing four spinvalves at in-plane parallel configuration.

(e) NS4 structure, representing four packaged spinvalves systems, composed by four spinvalves, at in-plane parallel configuration.

Figure 4.10: Representation of the five sensor's structures measured in the noise setup.

Noise measurements were performed with the structures biased by 600 mV and the results are presented in figure 4.11.

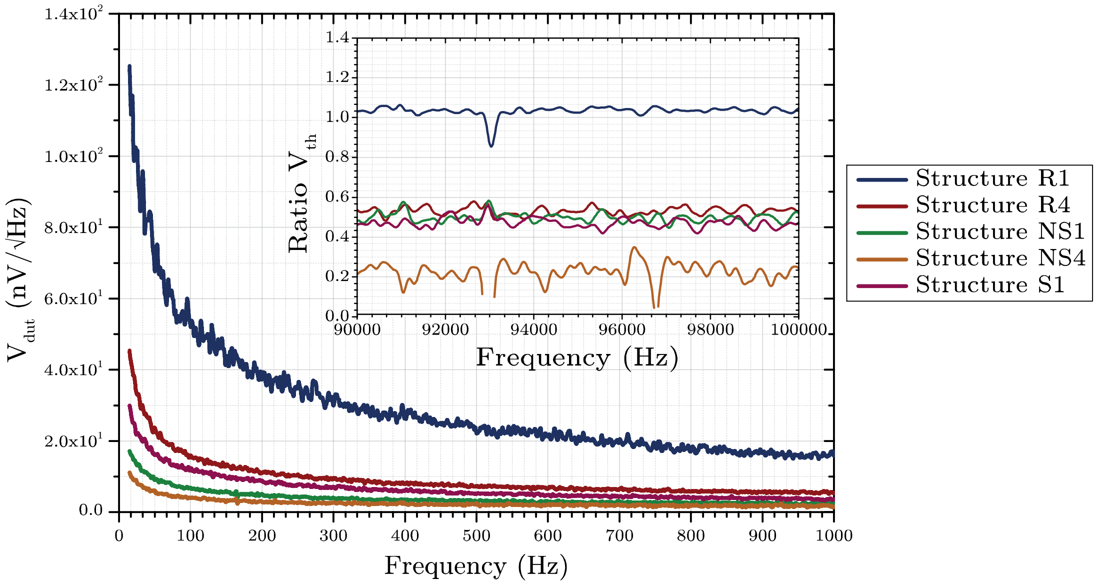

Figure 4.11: Noise spectrum for the five structures measured. The inner graphic represents the ratio between the experimental noise and the theoretical thermal noise of one spinvalve, given by equation 2.56; in the range of frequencies represented, the 1/f noise is neglegible.

Structure	M	$\frac{1}{\sqrt{M}}$	$S^{theo}_{thermal}(nV/\sqrt{Hz})$	$S^{exp}_{thermal}(nV/\sqrt{Hz})$	Thermal ratio	$\alpha_{Hooge}/N_c(10^{-13})$
R1	1	1.00	3.0	3.1	1.00	7.0
R4	4	0.50		1.6	0.53	3.1
NS1	4	0.50		1.5	0.50	0.5
NS4	16	0.25		0.8	0.23	0.8
S1	4	0.50		1.4	0.47	1.5

Table 4.4: Thermal ratios for the five structures studied, where **M** represents the number of spinvalves in each structure. The α_{Hooge}/N_c parameter was obtained by fitting the noise spectrum curve using equation 2.60.

	Noise $(nV/\sqrt{Hz})$				
Frequency (Hz)	**R1**	**R4**	**NS1**	**NS4**	**S1**
30	85	30	12	7.6	21
100	52	16	6.8	4.0	12
10000	4.6	2.2	1.6	1.0	1.6

Table 4.5: Detectivity values for three frequencies for the five structures.

Table 4.4 represents the experimental thermal ratios, obtained by dividing the experimental thermal noise by the theoretical thermal noise calculated from equation 2.56, and also the theoretical ratio given by $\frac{1}{\sqrt{M}}$, where M is the number of spinvalves in each structure. These experimental results are consisted compared to the ones theoretically expected. The structure with only one spinvalve (*R1*) presents a higher noise than the others, and has a value similar to the one calculated. The structures with 4 spinvalves (*R4*, *NS1* and *NS4*) show similar experimental noise values and in agreement to the theoretically expected, with a relative error of approximately 6%. Finally, the structure with 16 spinvalves (*NS4*) also reveal a good fit with the theoretical values, with a relative error of 8%. These results demonstrate that the spinvalve stacks' packaging successfully reduces the noise of the structure, and in the same away as the horizontal parallel configuration.

Notice that, at the low frequency range, all the curves have different slopes, which, recalling equation 2.64, should not occur. Since all the structures were biased with the same voltage (600 mV), the only parameter that distinguish them is the number of spinvalves in the packaged system M. However, as described at section 2.2.4, the magnetic component of the Hooge constant depends on the stability of the magnetic moments of the magnetic layer. It was also demonstrated that this stability is improved for configurations away from $\theta = \frac{\pi}{2}$, which is related with the offset field of the sample. Figure 4.12 presents the relation between the ${}^{\alpha_{Hooge}}/_{N_c}$ parameter and the H_f. As expected, higher absolute values of the offset field are related with lower Hooge constants, which implies higher stabilities, as predicted before.

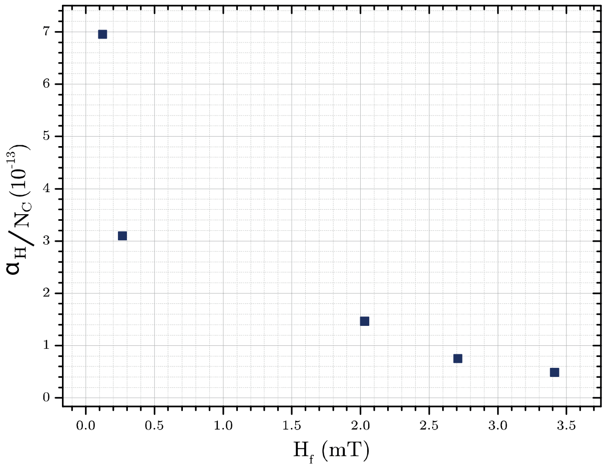

Figure 4.12: Relation between the ${}^{\alpha_{Hooge}}/_{N_c}$ parameter and the offset field H_f.

However, these results do not indicate a better performance of the sensor. As discussed before in section 2.2.4, performance is measured by the minimum amount of detected field, which is expressed by the detectivity, defined in equation 2.55 as the ratio between the noise, expressed in ${}^{V}/_{\sqrt{Hz}}$, and the sensitivity, expressed in ${}^{V}/_{T}$. On its side, the sensitivity for each structure was measured from their magnetotransport curves and are presented in table 4.6, along with other magnetic properties: MR, R_{min}, H_f an H_c.

Structure	**MR (%)**	**R_{min} (Ω)**	**μ_0H_f (mT)**	**μ_0H_c (mT)**	**Sensitivity (${}^{\%}/_{mT}$)**	**Sensitivity (${}^{mV}/_{mT}$)**
R1	5.0	536	-0.1	0.3	1.2	6.9
R4	4.8	140	-0.3	0.4	1.2	7.1
NS1	4.8	132	-3.4	0.2	0.3	2.0
NS4	4.6	32	-2.7	0.2	0.3	1.9
S1	5.0	117	-2.0	0.3	0.4	2.7

Table 4.6: Magnetic properties obtained from the magnetotransport curves for the 5 structures under study.

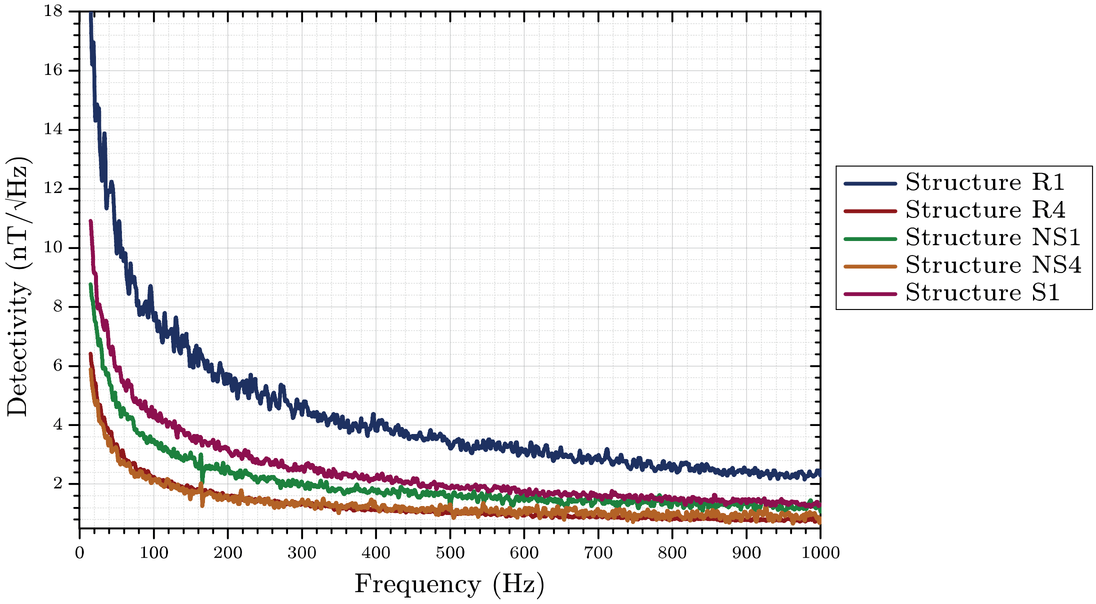

Figure 4.13: Detectivity spectrum for the five structures measured obtained from the noise spectrum and the sensitivity values presented in table 4.6.

	Detectivitiy ($nT/\sqrt{Hz}$)				
Frequency (Hz)	**R1**	**R4**	**NS1**	**NS4**	**S1**
30	12.3	4.2	6.3	4.0	7.6
100	7.6	2.2	3.5	2.1	4.4
10000	0.7	0.3	0.8	0.5	0.6

Table 4.7: Detectivity values for three frequencies for the five structures.

The detectivity spectrum obtained shows that, between the 3 structures that only include one spin-valve patterned structure (R1, NS1 and S1), R1 evidences the worst detectivity levels, while NS1 and S1 present similar performance values. However, analysing the results for the structures containing in-plane parallel sensors R4 ($M = 4$) and NS4 ($M = 16$) both reveal similar detectivity levels, which seems to contradict the $D \propto {}^{1}\!/\!\sqrt{M}$ relation, explained in the detectivity equation 2.66. This unconformity derives from the fact that the factor γ, declared in that equation and expressing the sensitivity of the sensor in ${}^{\%}\!/\!_{mT}$, is not constant between these structures and consequently describes a relation as $D \propto {}^{1}\!/\!_{\gamma\sqrt{M}}$. This difference in the sensitivities is presented in table 4.6 and is studied in the next section.

4.4 Sensitivity

To further understand the decrease of the sensitivity, four samples were microfabricated with different number of spinvalves (SV1889) packaged. These samples are designated as $L1$, $L2$, $L3$, and $L4$ and correspond respectively to a packaged system with 1, 2, 3, and 4 spinvalves separated, once more, by 700 Å of AlN. The magnetic transport curves were measured and the results are displayed in figure 4.14, and the data presented in table 4.8.

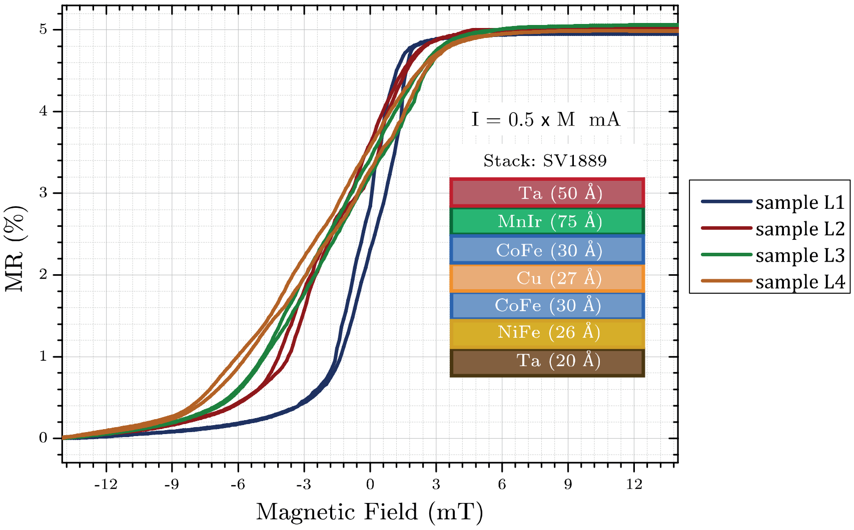

Figure 4.14: Magnetic transport curves for the four samples L1, L2, L3 and L4.

Structure	**MR (%)**	**$\mu_0 H_f$ (mT)**	**$\mu_0 H_c$ (mT)**	**Sensitivity ($^{\%}/_{mT}$)**
L1	4.9	0.01	0.45	1.2
L2	4.9	-1.55	0.18	0.6
L3	5.0	-1.67	0.24	0.5
L4	5.0	-2.03	0.29	0.4

Table 4.8: Magnetic properties obtained from the magnetotransport curves for the 4 samples.

As analysed in the previous section and seen in figure 4.14, sensitivity decrease occurs in the packaged spinvalves, being a drawback that affects the final performance of the sensor in terms of the minimum detectable field. To understand the origin of this effect, it is examined the elements that influence the sensitivity of a spinvalve sensor and extrapolate it to the packaged system.

Recalling the minimization energy approached in section 2.2.2, the sensitivity is given by $\frac{1}{N_{xx}M_{free}-H_k}$, where $N_{xx}M_{free}$ defines the demagnetizing field of the free layer and H_k the anisotropic field.

For a packaged spinvalve system, each free layer senses the demagnetizing from the other free layers. Notice that the anisotropic field contribution is not considered because it is an internal field component. This field can be seen as a virtual field that is intended to describe the interaction between the crystalline structure and the magnetic moments within, thus, having no external influence.

The external fields are sensed by each free layer in the same direction as their owns, meaning that the effective demagnetizing (H_{free}^{eff}) field on the free layer i is given by:

$$H_{free_i}^{eff} = H_{free_i} + \sum_{j \neq i}^{M} H_{free_j}, \tag{4.1}$$

where M is the number of spinvalves in the system, $H_{free} = N_{xx}M_{free}$, and H_{free_j} is the magnitude of the demagnetizing field from the free layer k sensed in the free layer i.

Thus, the sensitivity S is expressed as:

$$S_i = \frac{1}{(H_{free_i} - H_{k_i}) + \sum_{j\neq i}^{M} H_{free_j}}. \tag{4.2}$$

Since $H_{free} > 0$, $\sum_{j\neq i}^{M} H_{free_j} > 0$, and thus the denominator of equation 4.2 increases when increasing the number of spinvalves (M) in the system. Consequently, its sensitivity decreases as demonstrated by the experimental results.

However, from the results obtained for the 4 samples, it is observed an increase in the shift of the curve with the increase of the number of the packaged spinvalves. The previous analysis does not explain this behaviour, and thus further development must be done.

Once more, considering the conclusions obtained in section 2.2.2, the shift for a spinvalve sensor is given by $H_{D_{pinned}} - H_{Neel}$, where $H_{D_{pinned}}$ and H_{Neel} are the demagnetizing field from the pinned layer and the field from the Néel coupling sensed by the free layer. Moreover, for a packaged system another contribution to the shift arises from the magnetic field created by the current biasing each spinvalve, and afterwards, sensed by the other spinvalves.

To study the influence of the bias current on the system, a patterned structure with two packaged spinvalves and 700 Å thick AlN spacer was biased and measured with 0.03 mA and 3 mA and these results are presented in figures 4.15 and table 4.9.

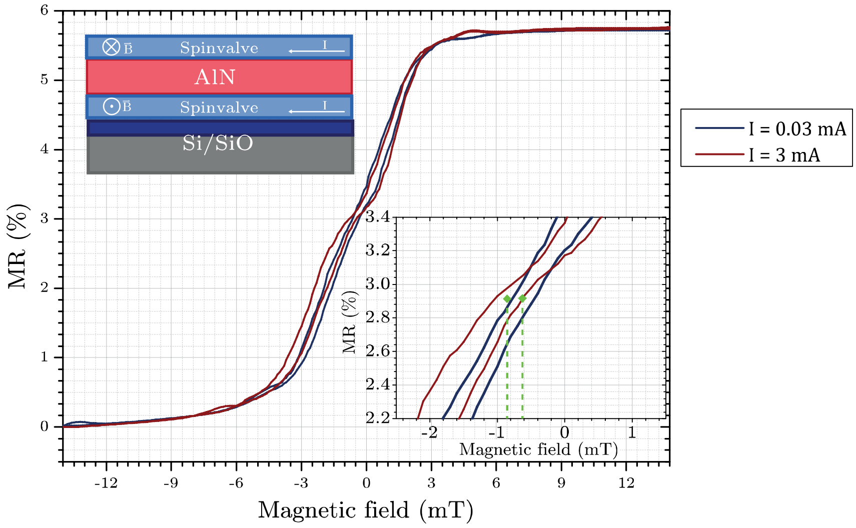

Figure 4.15: Magnetic transport curves for the two packaged sample biased with 0.03 mA and 3 mA.

Bias Current (mA)	**MR (%)**	**μ$_0$H$_f$ (mT)**	**μ$_0$H$_c$ (mT)**	**Sensitivity** ($\%/_{mT}$)
0.03	5.8	-0.68	0.16	0.79
3	5.8	-0.90	0.21	0.68

Table 4.9: Magnetic properties for the two packaged SV sample biased with 0.03 mA and 3 mA.

As expected, since the magnetic field is proportional to its current source, increasing the current originated a higher shift in the magnetotransport curve of the packaged system, from -0.68 mT to -0.90 mT. This shift was calculated theoretically using Ampere's law and the distance between the free layers and the copper layers, which can be considered to conduct the majority of the bias current, thus being responsible by the created magnetic field. Using this procedure the shift obtained is 0.27 mT similar to the obtained experimental value of 0.22 mT. Also, a decrease in the sensitivity, from 0.79 %/mT to 0.68 %/mT is observed, which is explained by the relative shift of each stack in the package, since the magnetic field created by the bias current is sensed in opposite directions by each SV that belongs to the package system. However, this variation is minimal considering that was used a current 100 times larger. Thus, the conclusion is that for a distance of 700 Å, given by the spacer, the field created by the current passing in each spinvalve is negligible. Therefore, the investigation is now focused in the demagnetizing field of the pinned layer and the Néel coupling field.

The offset field for a single spinvalve is then defined as $H_f = H_{Neel} - H_{D_{pinned}}$ and so, to ensure a centered curve, a fine tuning between the Néel coupling, caused by the surface roughness, and the demagnetizing field is essential.

For a packaged system, this tuning is much more complex because each spinvalve senses the demagnetizing field from the others. In addiction to this, each spinvalve senses different total demagnetizing fields according to their position in the stack. For example, an inner spinvalve senses a total demagnetizing field that is approximately twice the field sensed by the an outer spinvalve. Also, the Néel coupling field of each spinvalve is different due to the roughness cumulative effect explained further on. The difference in the Néel coupling field and total demagnetizing fields, created by each spinvalve, implies different shifts, producing a final curve with a lower sensitivity.

This issue is further explained in figure 4.16, which represents two R(H) curves with different offsets (H_{f1} and H_{f2}) and the resulting curve from a packaged system composed by spinvalves with those R(H) characteristics. The sensitivity loss is explained by an increase of the linear range ($\Delta H_{package}$) on the packaged system's R(H) curve.

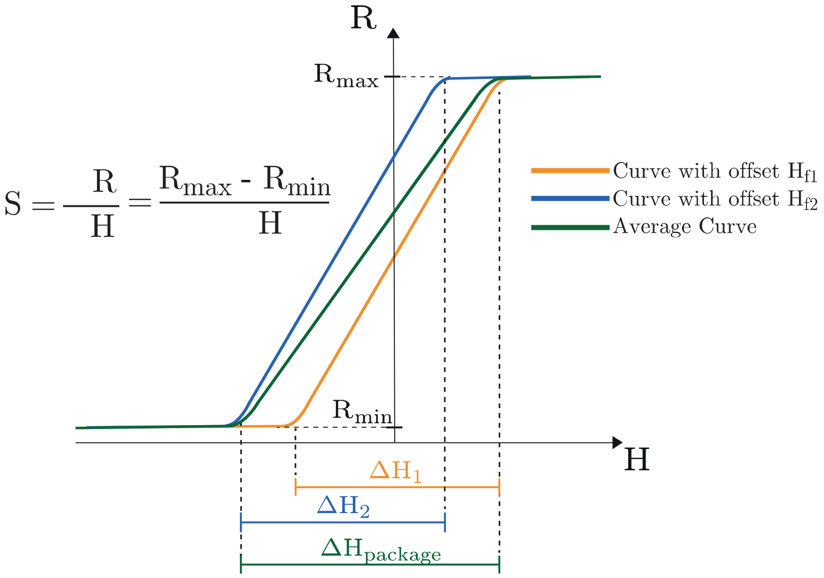

Figure 4.16: Simulated magnetotransport curves to demonstrate the lost in sensitivity due to spinvalves with different offsets in the packaged system.

The solution for this problem is to increase the distance between the spinvalves by increasing the thickness of the spacer.

To test this solution, seven samples were microfabricated, six of them consisting in four spinvalves packaged with different spacer's thickness and the other consisting in a individual stack.

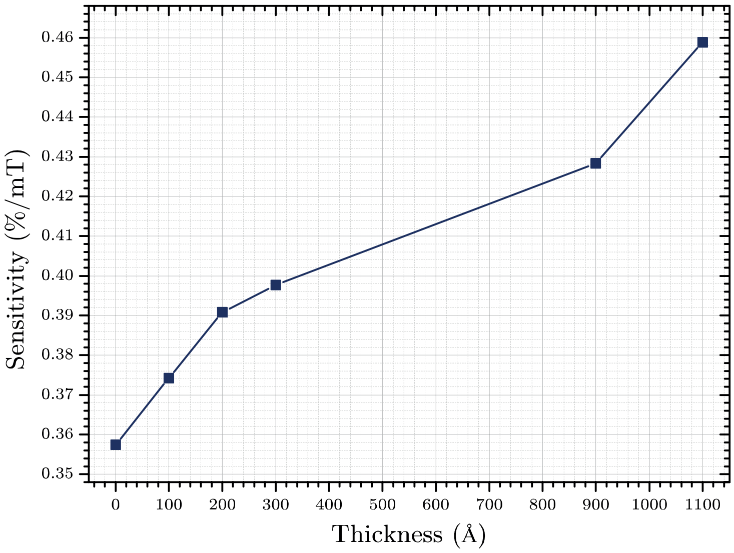

Figure 4.17: Variation of the sensitivity with the thickness of the spacer layer (AlN).

AlN thickness (Å)	**MR (%)**	**μ_0H_f (mT)**	**μ_0H_c (mT)**	**Sensitivity ($\%/_{mT}$)**
0	5.7	1.9	0.18	0.36
100	6.0	1.7	0.11	0.37
200	5.9	1.9	0.24	0.39
300	6.2	1.5	0.06	0.40
900	5.9	1.7	0.09	0.43
1100	5.8	1.4	0.10	0.46

Table 4.10: Magnetic properties dependency on the spacer layer (AlN) thickness.

Sample	**MR (%)**	**μ_0H_f (mT)**	**μ_0H_c (mT)**	**Sensitivity ($\%/_{mT}$)**
Singel SV	5.3	0.2	0.18	1.01

Table 4.11: Magnetic properties for a single SV.

The results confirm the previous conclusions, since the the sensitivity is increasing when increasing the thickness of the spacer. The larger separation diminishes the contributions of the external demagnetizing fields from the free and pinned layers, which reduces the shift and also improves the individual sensitivity, as explained previously. Table 4.11 presents the sensitivity of one single spinvalve equal to $1.01\,\%/\mathrm{mT}$. Extrapolating the results from table 4.10, considering a linear variation, it would be necessary a spacer with a thickness of $7000\,$Å to recover the sensitivity of the individual spinvalve.

These results comprehend another effect related to the increase of the Néel coupling field due to the increase of the roughness with the thickness of the spacer layer. These effect is represented in figure

4.18 and was measured from the offset field of the MR curve of the unpatterned packaged structures mentioned previously because, in these conditions, the demagnetizing fields are negligible.

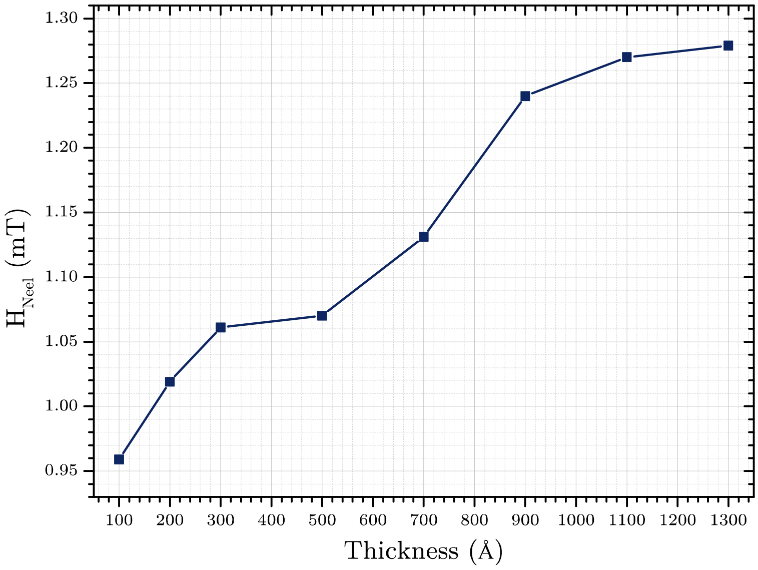

Figure 4.18: Variation of Néel coupling field with the thickness of the spacer layer.

Finally, in a package system, each spinvalve senses different Néel coupling fields because the amplitude of the roughness profile of the AlN increases with the number of levels in the packaged system. However, this effect is delimited by the limit of the roughness of a layer deposited by Magnetron Sputtering. This limit is related with the process and conditions used, has demonstrated by F. Martin *et al.* [87]. Figure 4.19 presents the variation of the roughness with the thickness of AlN deposited by Magnetron Sputtering, which converges to a value around 2 nm for 20 000 Å [87]. This thickness is approximately 28 times higher than the oxide spacer used in this work (700 Å), and, thus, would require a packaged system with 28 spinvalves. Also, in the same figure are presented the AFM measurements performed in this thesis. The roughness measured for the sample with soft-etch is approximately half of the one obtained by F. Martin, meaning that the roughness convergence is achieved for film thicker than 20 000 Å. Contrarily, it is observed that the roughness of AlN without soft-etch is close to roughness limit, thus, even thinner films allow to a fast convergence.

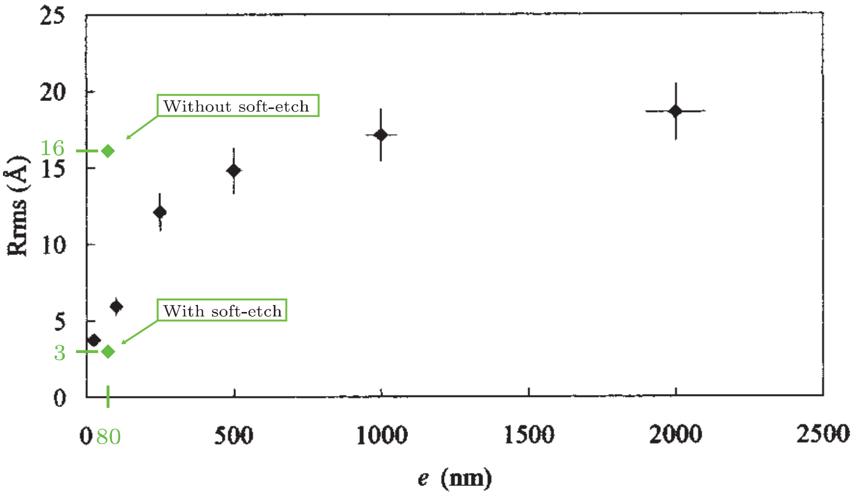

Figure 4.19: Rms roughness as a function of AlN thin-film thickness. From [87].

To further demonstrate this effect, three samples, N1, N2, and N3, were deposited with 1, 2, and 3 packaged spinvalves, as illustrated in figure 4.20. Between the spinvalves at N2 and N3, 700 Å of AlN were deposited, without performing soft-etch. This allows to visualize the convergence effect of the packaged system by the different Néel coupling values obtained. The samples were measured unpatterned to ensure that only the Néel coupling is present.

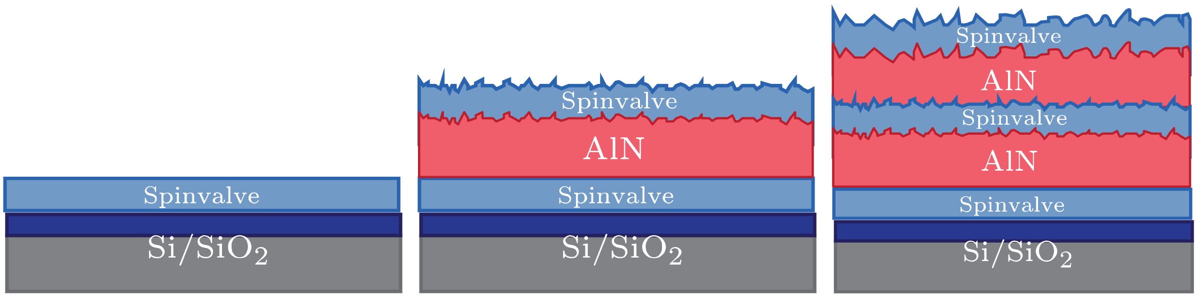

(a) Sample L1.

(b) Sample L2.

(c) Sample L3.

Figure 4.20: Representation of the samples used to study the roughness limit from Néel field measurement.

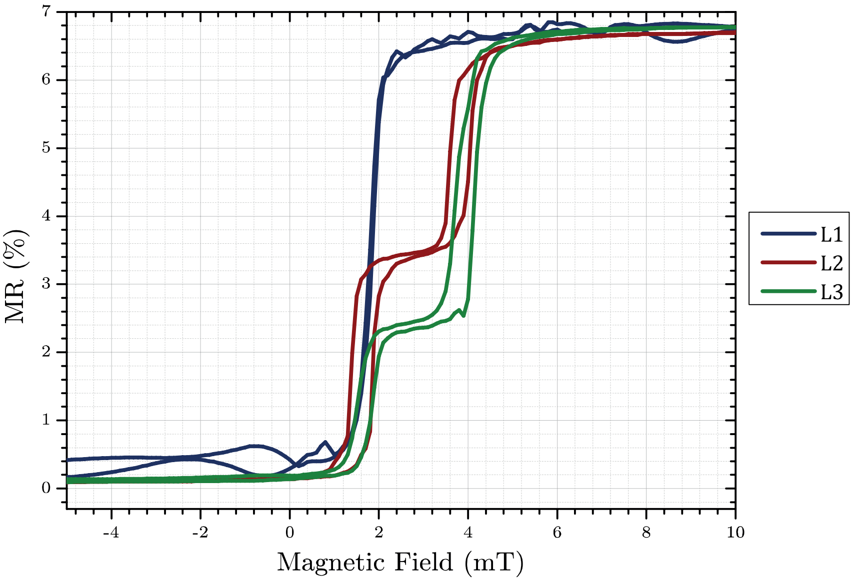

Figure 4.21: Magnetotransport curves for unpatterned N1, N2, and N3 samples.

The results (figure 4.21) shows that the curve from sample N2 presents a step, in the middle of the curve. This is explained by the fact that one of the spinvalves is deposited in a low roughness Si/SiO$_2$ substrate, while the other is deposited in a higher roughness AlN substrate (700 Å), with an expected roughness of 1.6 nm. Thus, the relative offset, created by the different Néel couplings, creates that step. However, using the same principle, a two-step curve should be obtained for sample N3. This results is not observed, instead only one step is present but, this time, at approximately one third of the curve. This can be explained by the fact that the two spinvalves deposited on top of the high roughness AlN layer have equal Néel coupling components, which is an effect of the roughness limit for the AlN deposited by Magnetron Sputtering.

Chapter 5

Conclusions

The goal of this work was to develop a process that uses spinvalves in parallel configuration to decrease its noise levels, without extinguish its main characteristic of having low spatial footprint, and consequently high spatial resolution. The strategy consisted in using the vertical dimension to create these parallel structures as a spinvalve packaged system.

The methodology consisted in optimizing the SV architecture, by using a proper spacer material, with low roughness, to separate the SVs vertically, and then a study of the characteristics of these structures, specifically the noise levels and detectivity capabilities.

One of the main concerns was regarding the electrical contacts, since in these packaged systems the available contact area is almost 50 times smaller than for individual SVs. Nevertheless, resistance measurements, performed for structures with different number of packaged spinvalves, revealed total agreement with the theory, which validates the magnetron sputtering deposition process as a reliable contact performing process.

The noise measurements also validate the strategy by showing full agreement with the theoretical predictions, with the noise levels decreasing with $^1/_{\sqrt{M}}$. The magnetotransport curves of $M = 4$ SV structures revealed loss in sensitivity, when compared with individual SV, indicating magnetic coupling effects between the SV elements, which could not be surpassed by the AlN spacer thickness used (800 Å)

Individual packaged structure with 4 spinvalves performs better than an individual spinvalve, since the first showed detectivity levels of 7.6 nT/$\sqrt{\text{Hz}}$ at 30 Hz (4.4 nT/$\sqrt{\text{Hz}}$ at 100 Hz), compared to the last with detectivity of 12.3 nT/$\sqrt{\text{Hz}}$ at 30 Hz (7.6 nT/$\sqrt{\text{Hz}}$ at 100 Hz). These results validate that, for the same spatial footprint, the packaged system presents an improved performance.

Notwithstanding, the detectivity level of a 4 packaged spinvalve system is worst than a in-plane parallel system with 4 spinvalve sensors, which presented detectivity values of 4.2 nT/$\sqrt{\text{Hz}}$ at 30 Hz (2.2 nT/$\sqrt{\text{Hz}}$ at 100 Hz). This shows that the improvement efficiency of the in-plane configuration is higher than the vertical packaging, due to the sensitivity loss in the last.

The main causes of this deficiency in the packaged system were studied and, for the spinvalve stack used, it was predicted that increasing the spacer's thickness to 7000 Å would recover the sensitivity levels of the individual spinvalve, by reducing the magnetic interactions between the spinvalves.

This conclusion limits the practical use of this strategy compared to the in-plane configuration. First, the patterning requires long etch times, which implies that small variations in the etch rate would induce large etch thicknesses, thus requiring a mass spectrometer for precise control of the etch process. Furthermore, as mentioned in section 3.1.2, the etch is performed at $70°$ to improve the removal of etch particles. For large structures, with spacer thickness in the order of 1000 Å, this angle produces a disproportion between the top and bottom spinvalves, with differences in the dimensions up to micrometer size.

Nevertheless, to surpass this obstacle, some strategies may be carried out in a continued work. These rely in the use of spinvalves with a synthetic-ferrimagnet free layer (SF) [88, 89] and synthetic-antiferromagnet pinned layer (SAF), which are characterized by a smaller effective magnetization. The effect would be a decrease of the offset bias of SVs, due to the reduction of the demagnetizing field component from the pinned layer. Another consequence would be the improvement of sensitivity, by decreasing the free layer's demagnetizing field component. Moreover, for vertical packaged system, these improved spinvalves would diminish the magnetic interaction between them, thus attenuating the sensitivity reduction, and also, requiring smaller spacer thicknesses. Therefore, reducing the total deposition time, and the thickness to be etched.

Therefore, the results obtained in this thesis are the starting point in the development of a process that can have an important contribution to the improvement of magnetoresistive sensors' noise level reduction.

Bibliography

[1] A. C. Fernandes, C. M. Duarte, F. a. Cardoso, R. Bexiga, S. Cardoso, and P. P. Freitas. Lab-on-chip cytometry based on magnetoresistive sensors for bacteria detection in milk. *Sensors (Basel, Switzerland)*, 14(8):15496–524, 2014. doi: 10.3390/s140815496. URL `http://www.pubmedcentral.nih.gov/articlerender.fcgi?artid=4179045&tool=pmcentrez&rendertype=abstract`.

[2] C. Tsang, R. Fontana, T. Lin, D. Heim, V. Speriosu, B. Gurney, and M. Williams. Design, fabrication and testing of spin-valve read heads for high density recording. *IEEE Transactions on Magnetics*, 30(6):3801–3806, 1994. doi: 10.1109/20.333909. URL `http://dx.doi.org/10.1109/20.333909`.

[3] D. Tang, P. Wang, V. Speriosu, S. Le, and K. Kung. Spin-valve RAM cell. *IEEE Transactions on Magnetics*, 31(6):1941–0069, 1995. doi: 10.1109/20.490329. URL `http://dx.doi.org/10.1109/20.490329`.

[4] S. Setua, M. Ouberai, S. G. Piccirillo, C. Watts, and M. Welland. Cisplatin-tethered gold nanospheres for multimodal chemo-radiotherapy of glioblastoma. *Nanoscale*, 6(18):10865–73, 2014. doi: 10.1039/c4nr03693j. URL `http://www.ncbi.nlm.nih.gov/pubmed/25117686`.

[5] S. K. Min, W. Y. Kim, Y. Cho, and K. S. Kim. Fast DNA sequencing with a graphene-based nanochannel device. 6(3):162–5, 2011. doi: 10.1038/nnano.2010.283. URL `http://www.ncbi.nlm.nih.gov/pubmed/21297626`.

[6] J. Pedro and A. Amaral. *Measuring Neuronal Activity with High Sensitivity Magnetoresistive Sensors*. PhD thesis, Instituto Superior Técnico, 2014.

[7] D. D. Tang and Y.-J. Lee. *Magnetic Memory - Fundamentals and Technology*, chapter 2 and 4. Cambridge University Press, 2010.

[8] P. P. Freitas, R. Ferreira, S. Cardoso, and F. Cardoso. Magnetoresistive sensors. *Journal of Physics: Condensed Matter*, 19(16):165221, 2007. doi: 10.1088/0953-8984/19/16/165221. URL `http://stacks.iop.org/0953-8984/19/i=16/a=165221`.

[9] P. P. Freitas, S. Cardoso, R. Ferreira, V. C. Martins, A. Guedes, F. A. Cardoso, J. Loureiro, R. Macedo, R. C. Chaves, and J. Amaral. Optimization and Integration of Magnetoresistive Sensors. *SPIN*, 1(1):71–91, 2011. ISSN 2010-3247. doi: 10.1142/S2010324711000070. URL `http://dx.doi.org/10.1142/S2010324711000070`.

[10] C. Tsang, R. E. Fontana, T. Lin, D. E. Heim, V. S. Speriosu, B. Gurney, M. L. Williams, et al. Design, fabrication and testing of spin-valve read heads for high density recording. *IEEE Transactions on Magnetics*, 30(6):3801–3806, 1994. doi: 10.1109/20.333909. URL `http://dx.doi.org/10.1109/20.333909`.

[11] H. Kanai, K. Noma, and J. Hong. Advanced spin-valve GMR head. *Fujitsu scientific and technical journal*, 37(6):174–182, 2001. doi: 10.1103/PhysRev.32.110.

[12] J. Hong, J. Kane, J. Hashimoto, M. Yamagishi, K. Noma, and H. Kanai. Spin-valve head with specularly reflective oxide layers for over 100 Gb/in 2. *IEEE Transactions on Magnetics*, 38(1): 15–19, 2002. doi: 10.1109/TMAG.2002.988904. URL `http://dx.doi.org/10.1109/TMAG.2002.988904`.

[13] D. C. Leitao, L. Gameiro, A. V. Silva, S. Cardoso, and P. P. Freitas. Field detection in spin valve sensors using CoFeB/Ru synthetic-antiferromagnetic multilayers as magnetic flux concentrators. *IEEE Transactions on Magnetics*, 48(11):3847–3850, 2012. doi: 10.1109/TMAG.2012.2195302. URL `http://dx.doi.org/10.1109/TMAG.2012.2195302`.

[14] A. Johnson. *Spin Valve Systems for Angle Sensor Applications*. PhD thesis, Technischen Universität Darmstadt, 2004.

[15] O. Ueberschar, M. J. Almeida, P. Matthes, M. Muller, R. Ecke, R. Ruckriem, J. Schuster, H. Exner, and S. E. Schulz. Optimized Monolithic 2-D Spin-Valve Sensor for High-Sensitivity Compass Applications. *Magnetics, IEEE Transactions on*, 51(1):1–4, 2015. doi: 10.1109/TMAG.2014.2358802. URL `http://dx.doi.org/10.1109/TMAG.2014.2358802`.

[16] R. Schäfer, D. Chumakov, O. De Haas, L. Schultz, W. Maass, K.-U. Barholz, and R. Mattheis. Magnetization processes in spin-valve meanders for sensor applications. *Magnetics, IEEE Transactions on*, 39(4):2089–2097, 2003. doi: 10.1109/TMAG.2003.812787. URL `http://dx.doi.org/10.1109/TMAG.2003.812787`.

[17] A. S. Edelstein and G. A. Fischer. Minimizing 1/f noise in magnetic sensors using a microelectromechanical system flux concentrator. *Journal of applied physics*, 91(10):7795–7797, 2002. doi: 10.1063/1.1451901. URL `http://dx.doi.org/10.1063/1.1451901`.

[18] A. Guedes, S. Patil, S. Cardoso, V. Chu, J. Conde, and P. Freitas. Hybrid magnetoresistive/microelectromechanical devices for static field modulation and sensor 1/f noise cancellation. *Journal of applied physics*, 103(7):7E924, 2008. doi: 10.1063/1.2837661. URL `http://dx.doi.org/10.1063/1.2837661`.

[19] H. Li, J. Gaspar, P. Freitas, V. Chu, and J. Conde. MEMS microbridge vibration monitoring using spin-valve sensors. *IEEE Transactions on Magnetics*, 38(5):3371–3373, 2002. doi: 10.1109/TMAG.2002.802288. URL `http://dx.doi.org/10.1109/TMAG.2002.802288`.

[20] A. Edelstein, G. A. Fischer, J. E. Burnette, W. E. Egelhoff, and S. F. Cheng. 2009 IEEE Sensors - Achieving 1/f noise reduction with the MEMS flux concentrator. 2009. doi: 10.1109/icsens.2009.5398411. URL `http://dx.doi.org/10.1109/icsens.2009.5398411`.

[21] A. Guedes, J. Almeida, S. Cardoso, R. Ferreira, and P. Freitas. Improving magnetic field detection limits of spin valve sensors using magnetic flux guide concentrators. *IEEE Transactions on Magnetics*, 43(6):2376–2378, 2007. doi: 10.1109/TMAG.2007.893119. URL `http://dx.doi.org/10.1109/TMAG.2007.893119`.

[22] J. P. Valadeiro, J. Amaral, D. C. Leitao, R. Ferreira, S. Freitas Cardoso, and P. J. Freitas. Strategies for pTesla Field Detection Using Magnetoresistive Sensors With a Soft Pinned Sensing Layer. *IEEE Transactions on Magnetics*, 51(1):1–4, 2015. doi: 10.1109/TMAG.2014.2352115. URL `http://dx.doi.org/10.1109/TMAG.2014.2352115`.

[23] N. Oliveira. 3D Magnetic Flux Concentrators with improved efficiency for Magnetoresistive Sensors. Master's thesis, Instituto Superior Técnico, 2010.

[24] Z. Qian, D. Wang, J. M. Daughton, M. Tondra, C. Nordman, and A. Popple. Linear spin-valve bridge sensing devices. *IEEE Transactions on Magnetics*, 40(4):2643–2645, 2004. doi: 10.1109/TMAG.2004.830212. URL `http://dx.doi.org/10.1109/TMAG.2004.830212`.

[25] Z. Qian, D. Wang, J. M. Daughton, M. Tondra, C. Nordman, and A. Popple. Cubells-Beltrán, María Dolores and Reig, Candid and Muñoz, Diego Ramírez and De Freitas, Susana Isabel Pinheiro Cardoso and De Freitas, Paulo Jorge Peixeiro. *Sensors Journal, IEEE*, 9(12):1756–1762, 2009. doi: 10.1109/TMAG.2004.830212. URL `http://dx.doi.org/10.1109/TMAG.2004.830212`.

[26] J. Valadeiro. Magnetoresistive sensors with pico-Tesla sensitivities. Master's thesis, Instituto Superior Técnico, 2014.

[27] H. Li. *Spin valve read elements and sensors*. PhD thesis, Instituto Superior Técnico, 2004.

[28] R. Guerrero, M. Pannetier-Lecoeur, C. Fermon, S. Cardoso, R. Ferreira, and P. P. Freitas. Low frequency noise in arrays of magnetic tunnel junctions connected in series and parallel. *Journal of Applied Physics*, 105(11):113922, 2009. ISSN 00218979. doi: 10.1063/1.3139284. URL `http://scitation.aip.org/content/aip/journal/jap/105/11/10.1063/1.3139284`.

[29] J. Amaral. *Measuring Neuronal Activity with High Sensitivity Magnetoresistive Sensors*. PhD thesis, Instituto Superior Técnico, 2014.

[30] E. Paz, S. Serrano-Guisan, R. Ferreira, and P. P. Freitas. Room temperature direct detection of low frequency magnetic fields in the 100 pT/Hz0.5 range using large arrays of magnetic tunnel junctions. *Journal of The Electrochemical Society*, 115(17):17E501, 2014. ISSN 0021-8979. doi: 10.1063/1.4859036. URL `http://dx.doi.org/10.1063/1.4859036`.

[31] S. Liou, X. Yin, S. Russek, R. Heindl, F. Da Silva, J. Moreland, D. Pappas, L. Yuan, and J. Shen. Picotesla Magnetic Sensors for Low-Frequency Applications. *IEEE Transactions on Magnetics*, 47

(10):3740–3743, 2011. ISSN 0018-9464. doi: 10.1109/tmag.2011.2157997. URL `http://dx.doi.org/10.1109/tmag.2011.2157997`.

[32] M. Tondra, J. M. Daughton, D. Wang, R. S. Beech, A. Fink, and J. A. Taylor. The Evolution of (001) Si/SiO2 Interface Roughness during Thermal Oxidation. *Journal of Applied Physics*, 83(11):6688, 1998. ISSN 0021-8979. doi: 10.1063/1.367861. URL `http://dx.doi.org/10.1063/1.367861`.

[33] V.-S. Luong, C.-H. Chang, J.-T. Jeng, C.-C. Lu, J.-H. Hsu, and C.-R. Chang. The Evolution of (001) Si/SiO2 Interface Roughness during Thermal Oxidation. *IEEE Transactions on Magnetics*, 50(11): 1–4, 2014. ISSN 0018-9464. doi: 10.1109/TMAG.2014.2329058. URL `http://dx.doi.org/10.1109/TMAG.2014.2329058`.

[34] A. Lopes, S. Cardoso, R. Ferreira, E. Paz, F. L. Deepak, J. Sanchez, D. Ramirez, S. I. Ravelo, and P. P. Freitas. MgO Magnetic Tunnel Junction Electrical Current Sensor With Integrated Ru Thermal Sensor. *IEEE Transactions on Magnetics*, 49(7):3866–3869, 2013. ISSN 0018-9464. doi: 10.1109/TMAG.2013.2246550. URL `http://dx.doi.org/10.1109/TMAG.2013.2246550`.

[35] Z. Lei, G. Li, W. Egelhoff, P. Lai, and P. Pong. Review of Noise Sources in Magnetic Tunnel Junction Sensors. *IEEE Transactions on Magnetics*, 47(3):602–612, 2011. ISSN 0018-9464. doi: 10.1109/tmag.2010.2100814. URL `http://dx.doi.org/10.1109/tmag.2010.2100814`.

[36] F. A. Cardoso, L. Rosado, R. Ferreira, E. Paz, S. Cardoso, P. M. Ramos, M. Piedade, and P. P. Freitas. Magnetic tunnel junction based eddy current testing probe for detection of surface defects. *Journal of Applied Physics*, 115(17):17E516, 2014. ISSN 0021-8979. doi: 10.1063/1.4864045. URL `http://dx.doi.org/10.1063/1.4864045`.

[37] R. J. Janeiro, L. Gameiro, A. Lopes, S. Cardoso, R. Ferreira, E. Paz, and P. P. Freitas. Linearization and Field Detectivity in Magnetic Tunnel Junction Sensors Connected in Series Incorporating 16 nm-Thick NiFe Free Layers. *IEEE Transactions on Magnetics*, 48(11):4111–4114, 2012. ISSN 018-9464. doi: 10.1109/TMAG.2012.2202887. URL `http://dx.doi.org/10.1109/TMAG.2012.2202887`.

[38] W. Zhang, Q. Hao, and G. Xiao. Low-frequency noise in serial arrays of MgO-based magnetic tunnel junctions. *Physical Review B*, 84(9):094446, 2011. ISSN 1098-0121. doi: 10.1103/PhysRevB.84.094446. URL `http://dx.doi.org/10.1103/PhysRevB.84.094446`.

[39] S. Cardoso, D. C. Leitao, L. Gameiro, F. Cardoso, R. Ferreira, E. Paz, and P. P. Freitas. Magnetic tunnel junction sensors with pTesla sensitivity. *Microsystem Technologies*, 20(4-5):793–802, 2014. ISSN 0946-7076. doi: 10.1007/s00542-013-2035-1. URL `http://dx.doi.org/10.1007/s00542-013-2035-1`.

[40] K. Fujiwara, M. Oogane, D. Kato, T. Nishikawa, H. Naganuma, and Y. Ando. Fabrication of Integrated Magnetic Tunnel Junctions for Detection of Bio-magnetic Field. 52:505, 2014. doi: 10.11239/jsmbe.52.O-505. URL `http://dx.doi.org/10.11239/jsmbe.52.O-505`.

[41] B. M. Moskowitz. Hitchhiker's Guide to Magnetism. online.

[42] M. Mendes. Micromagnetic Simulations of Spin Valve devices. Master's thesis, Instituto Superior Técnico, 2005.

[43] R. Flores. MgO Magnetic Tunnel Junction sensors in Full Wheatstone Bridge configuration for in-chip current field detection. Master's thesis, Instituto Superior Técnico, 2010.

[44] A. P. Guimarães. *Principles of Nanomagnetism*, chapter 2 and 5. Springer, 2009.

[45] A. Aharoni. *Introduction to the Theory of Ferromagnetism*. Oxford University Press, 2007. ISBN:N 978-0-19-850809-0.

[46] C. Kittel. Physical Theory of Ferromagnetic Domains. *Review of Modern Physics*, 21:541–583, 1949. ISSN 0034-6861. doi: 10.1103/RevModPhys.21.541. URL `http://dx.doi.org/10.1103/RevModPhys.21.541`.

[47] C. Andreas, S. Gliga, and R. Hertel. Numerical micromagnetism of strong inhomogeneities. *Journal of Magnetism and Magnetic Materials*, 362:7–13, 2014. ISSN 0304-8853. doi: 10.1016/j.jmmm.2014.02.097. URL `http://dx.doi.org/10.1016/j.jmmm.2014.02.097`.

[48] A. H. Morrish. *The Physical Principles of Magnetism*. Wiley-IEEE Press, 1^{st} edition, 2001. ISBN:078036029X.

[49] G. Bayreuther. Magnetic Anisotropy. PDF - Lecture Notes, 2011.

[50] S. Tumanski. *Handbook of Magnetic Measurements*, chapter 6. CRC, 2011.

[51] H. S. Nalwa. *Handbook of Thin Films, Five-Volume Set*, chapter 10. Academic Press, 2001.

[52] N. Wiese. *Coupling phenomena and scalability of CoFeB/Ru/CoFeB sandwiches*. PhD thesis, Naturwissenschaften der Fakultät für Physik der Universität Bielefeld, 2006.

[53] M. N. Baibich, J. M. Broto, A. Fert, F. N. Van Dau, and F. Petroff. Giant Magnetoresistance of (001)Fe/(001)Cr Magnetic Superlattices. *Physical Review Letters*, 61(21):2472–2475, 1988. ISSN 0031-9007. doi: 10.1103/physrevlett.61.2472. URL `http://dx.doi.org/10.1103/physrevlett.61.2472`.

[54] C. Reig, S. C. de Freitas, and S. C. Mukhopadhyay, editors. *Giant Magnetoresistance (GMR) Sensors - From Basis to State-of-the-Art Applications*, chapter 6. Springer, 2013.

[55] H. Ehrenreich and F. Spaepen, editors. *Solid State Physics*, volume 56, pages 113–237. Academic Press, 2001.

[56] B. Dieny, V. S. Speriosu, S. S. P. Parkin, B. A. Gurney, D. R. Wilhoit, and D. Mauri. Giant magnetoresistive in soft ferromagnetic multilayers. *Physics Review B*, 43(1):1297–1300, 1991. doi: 10.1103/PhysRevB.43.1297. URL `http://dx.doi.org/10.1103/PhysRevB.43.1297`.

[57] A. Johnson. *Spin Valve Systems for Angle Sensor Applications*. PhD thesis, Technische Universität Darmstadt, 2004.

[58] J. Ventura. Magnetic Nanostructures. Master's thesis, Faculdade de Ciências da Universidade do Porto, 2006.

[59] C. L. Platt, M. R. McCartney, F. T. Parker, and A. E. Berkowitz. Magnetic interlayer coupling in ferromagnet/insulator/ferromagnet structures. *Physical Review B*, 61(14):9633–9641, 2000. ISSN 1098-0121. doi: 10.1103/physrevb.61.9633. URL `http://dx.doi.org/10.1103/PhysRevB.61.9633`.

[60] J. C. S. Kools, W. Kula, D. Mauri, and T. Lin. Effect of finite magnetic film thickness on Néel coupling in spin valves. *Journal of Applied Physics*, 85(8):4466, 1999. doi: 10.1063/1.370376. URL `http://dx.doi.org/10.1063/1.370376`.

[61] C. Santos. MgO MTJ sensors in Wheatstone bridge for magnetometer devices. Master's thesis, Instituto Superior Técnico, 2010.

[62] A. V. Silva, D. C. Leitao, J. Valadeiro, J. Amaral, P. P. Freitas, and S. Cardoso. Linearization strategies for high sensitivity magnetoresistive sensors. *The European Physical Journal Applied Physics*, 72(1):10601, 2015. doi: 10.1051/epjap/2015150214. URL `http://dx.doi.org/10.1051/epjap/2015150214`.

[63] F. Cardoso. Design, optimization and integration of magnetoresistive biochips. Master's thesis, Instituto Superior Técnico, 2010.

[64] R. Coehoorn. Novel Magnetoelectronic Materials and Devices - Magnetic interactions and magnetization reversal processes. PDF Lecture Notes, 2003.

[65] V. Gehanno, P. Freitas, A. Veloso, J. Ferrira, B. Almeida, J. Soasa, A. Kling, J. Soares, and M. da Silva. Ion beam deposition of Mn-Ir spin valves. *IEEE Transactions on Magnetics*, 35(5): 4361–4367, 1999. ISSN 0018-9464. doi: 10.1109/20.799086. URL `http://dx.doi.org/10.1109/20.799086`.

[66] D.-H. Han, J.-G. Zhu, J. Judy, and J. Sivertsen. Effects of surface/interface morphology on giant magnetoresistance and magnetic field sensitivity of NiO-based spin-valves. *IEEE Transactions on Magnetics*, 33(5):3550–3552, 1997. doi: 10.1109/20.619494. URL `http://dx.doi.org/10.1109/20.619494`.

[67] E. Y. Tsymbal and I. Žutic, editors. *Handbook of Spin Transport and Magnetism*, chapter 4 and 5. CRC press, 2011.

[68] H. Ferreira. *Magnetoresistive biochips: Detection of biomolecular recognition and On-chip transport of magnetically labeled biomolecules*. PhD thesis, Instituto Superior Técnico, 2006.

[69] Harvard University. Thermal Noise. PDF Online - Lecture Notes.

[70] H. Nyquist. Thermal Agitation of Electric Charge in Conductors. *Physical Review*, 32, 1928.

[71] H. Nyquist. Thermal Agitation of Electric Charge in Conductors. *Physical Review (Series I)*, 32(1): 110–113, 1928. doi: 10.1103/PhysRev.32.110. URL `http://dx.doi.org/10.1103/PhysRev.32.110`.

[72] T. Markl. 1/f Noise, Telegraph Noise. online, November 2009.

[73] G. Liu, S. Rumyantsev, M. S. Shur, and A. A. Balandin. Origin of 1/f noise in graphene multilayers: Surface vs. volume. *Applied Physics Letters*, 105(102), 2013. doi: 0.1063/1.4794843. URL `http://dx.doi.org/10.1063/1.4794843`.

[74] K. Buschow, editor. *Handbook of Magnetic Materials*, volume 19, chapter 3. North Holland, 2011.

[75] P. M. H. P. Dutta. Low-frequency fluctuations in solids: 1/f noise. *Reviews of Modern Physics*, 53(8): 497, 1981. doi: 10.1103/RevModPhys.53.497. URL `http://dx.doi.org/10.1103/RevModPhys.53.497`.

[76] R. Van de Veerdonk, P. Belien, K. Schep, J. Kools, M. De Nooijer, M. Gijs, R. Coehoorn, and W. De Jonge. 1/f noise in anisotropic and giant magnetoresistive elements. *Journal of applied physics*, 82(12):6152–6164, 1997. doi: 10.1103/RevModPhys.53.497. URL `http://dx.doi.org/10.1103/RevModPhys.53.497`.

[77] S. Freitas. Dual-Stripe GMR and Tunnel Junction Read Heads and Ion Beam Deposition and Oxidation of Tunnel Junctions. Master's thesis, Instituto Superior Técnico, 2001.

[78] R. Ferreira. *Ion Beam Deposited Magnetic Spin Tunnel Junctions targeting HDD Read Heads, Non-volatile Memories and Magnetic Field Sensor Applications*. PhD thesis, Instituto Superior Técnico, 2011.

[79] Magnetron Sputtering Technology. Online PDF: http://www.directvacuum.com/.

[80] R. Macedo. *Spintronic Nano Devices: Nanofabrication of sub-50nm Magnetic Tunnel Junctions and Self-Powered Hybrid Sensors*. PhD thesis, Instituto Superior Técnico, 2011.

[81] G. W. Anderson, Y. Huai, and M. Pakala. Spin-valve thermal stability: The effect of different antiferromagnets. *Journal of Applied Physics*, 87(9):5726–5728, 2000. doi: 10.1063/1.372502. URL `http://dx.doi.org/10.1063/1.372502`.

[82] *Installation, Operation and Maintenance Manual - Dektak 3030ST*. Veeco Instruments.

[83] F. J. Giessibl. Advances in atomic force microscopy. *Review of Modern Physics*, 75(3):949–983, 2003. doi: 10.1103/revmodphys.75.949. URL `http://dx.doi.org/10.1103/revmodphys.75.949`.

[84] M. R. Amirzada, A. Tatzel, V. Viereck, and H. Hillmer. Surface roughness analysis of SiO2 for PECVD, PVD and IBD on different substrates. *Applied Nanoscience*, 2015. ISSN 2190-5509. doi: 10.1007/s13204-015-0432-8. URL `http://dx.doi.org/10.1007/s13204-015-0432-8`.

[85] D. Hill, X. Blasco, M. Porti, M. Nafri´a, and X. Aymerich. Characterising the surface roughness of AFM grown SiO2 on Si. *Microelectronics Reliability*, 41(7):1077–1079, 2001. ISSN 0026-2714. doi: 10.1016/s0026-2714(01)00078-6. URL `http://dx.doi.org/10.1016/s0026-2714(01)00078-6`.

[86] S. J. Fang. The Evolution of (001) Si/SiO2 Interface Roughness during Thermal Oxidation. *Journal of The Electrochemical Society*, 144(8):2886, 1997. ISSN 0013-4651. doi: 10.1149/1.1837912. URL `http://dx.doi.org/10.1149/1.1837912`.

[87] F. Martin, P. Muralt, M.-A. Dubois, and A. Pezous. Thickness dependence of the properties of highly c-axis textured AlN thin films. *Journal of Vacuum Science and Technology A Vacuum Surfaces and Films*, 22(2):361, 2004. ISSN 0734-2101. doi: 10.1116/1.1649343. URL `http://dx.doi.org/10.1116/1.1649343`.

[88] P. Coelho, D. C. Leitao, J. Antunes, S. Cardoso, and P. P. Freitas. 1/f noise in anisotropic and giant magnetoresistive elements. *IEEE Transactions on Magnetics*, 50(11):1–4, 2014. doi: 10.1109/tmag.2014.2325821. URL `http://dx.doi.org/10.1109/tmag.2014.2325821`.

[89] A. Veloso and P. P. Freitas. Spin valve sensors with synthetic free and pinned layers. *Journal of Applied Physics*, 87:5744, 2000.

Appendix A

Runsheet

Runsheet – Vertical Packaged Spinvalves

Responsible: Ricardo Varela Date: __/__/____

Sample ID:

Process 1: Substrate preparation Date: __/__/____

Machine: Wet Bench

Steps:

- Clean for 30 minutes in Alconox with ultrasounds;
- Clean with IPA (isopropyl alcohol) and water, and blow dry using compressed air gun.

Process 2: Spinvalve Package Deposition Date: __/__/____

Machines: **Nordiko 7000** > **Nordiko 3600 (soft etch)** > **Nordiko 3600 (stack deposition)**

Steps:

- Aluminum Nitride (AlN) deposition at Nordiko 7000;
- Soft etch at Nordiko 3600;
- Stack deposition at Nordiko 3600.

Repeat *N* times to create the packaged structure

Step 1: Spacer (AlN) deposition

Machine: Nordiko 7000

	Ar/N_2 flow (sccm)	**Pressure (mTorr)**	**RF Power (kW)**	**Dep. Rate (Å/s)**
Module 4	10/10	2	1	4

Thickness: _______ Å Total time:______ s Number of steps: ____

Cooldown: 700 s

Considering that each step should not have more than 80 seconds to avoid overheating of the sample.

Run #: _______

Read Values:

Module 4:

Step 2: Spacer soft-etch

Machine: Nordiko 3600

Time: 90 s Angle: 20°

Read Values:

Chamber pressure before process:_______

Chamber pressure during process:_______

Assist gun:

Step 3: Stack deposition

Machine: Nordiko 3600

Stack ID: 36SV____

Stack composition:

Read Values:

Chamber pressure before process:_______

Chamber pressure during process:_______

Deposition gun:

Stack magnetic characteristics:

MR:_________%	Hc: _________Oe
Hf: _________Oe	Hex: _________Oe

Process 3: Spinvalve definition

Date: __/__/____

Machines: **Vapor Prime > Track System (coating) > DWL > Track System (development)**

Steps:

- Vapor prime: program 0 – 5 min HMDS at 130°C;
- Track 1: program 6/2 – **coat** with 1.5 µm thick photoresist;
- DWL **exposure**;
- Track 2: program 6/2 – photoresist **development**;

Map: AMSION

Mask: rv_ind_SV

No field alignment

Energy: _____%

Focus: _____

Photoresist structures expected after development:

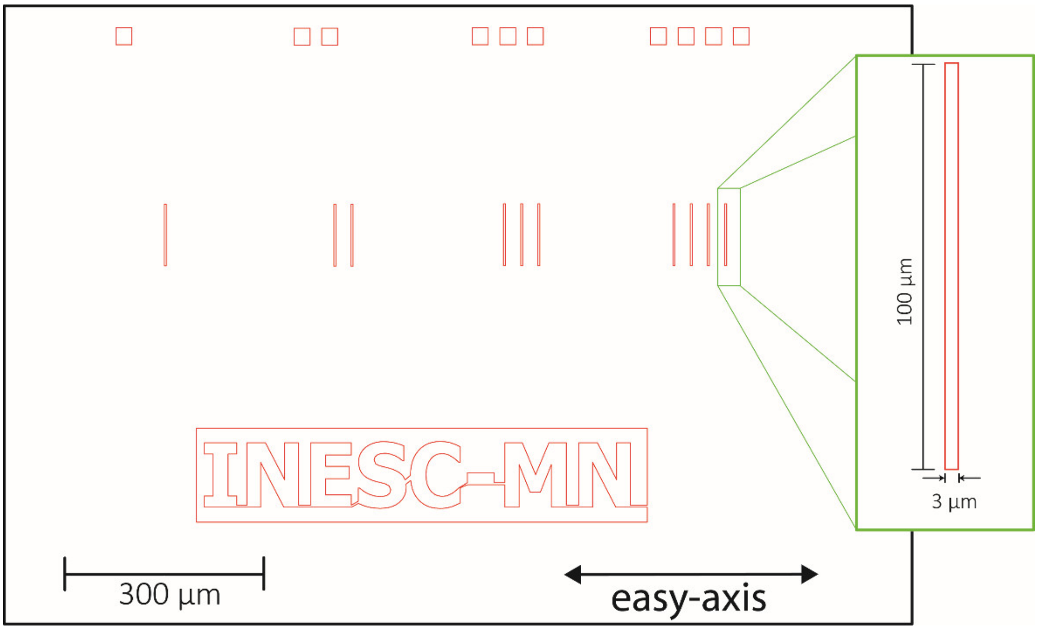

Process 4: Spinvalve etch Date: __/__/____

Machine: Nordiko 3600

Angle: 60° Etch Rate: 1.05 Å/s

Thickness: ______ Å Total time:_____ s Number of steps: ___

Cooldown: 200 s

Read Values:

Chamber pressure before process:_______

Chamber pressure during process:_______

Assist gun:

Process 5: Resist strip Date: __/__/____

Machine: Wet bench

Steps:

- Resist strip with Microstrip 3001 at 65°C with ultrasounds;
- Clean with IPA (**isopropyl** alcohol) and water, and blow dry using compressed air gun.

Time needed to complete process:_______________

Process 6: Paths definition

Date: __/__/____

Machines: **Vapor Prime > Track System (coating) > DWL > Track System (development)**

Steps:

- Vapor prime: program 0 – 5 min HMDS at 130°C;
- Track 1: program 6/2 – **coat** with 1.5 µm thick photoresist;
- DWL **exposure**;
- Track 2: program 6/2 – photoresist **development**;

Map: AMSION Mask: rv_ind_paths **X offset**: -400 µm **Y offset**: -186 µm

Energy: _____% Focus: _____

Photoresist structures expected after development:

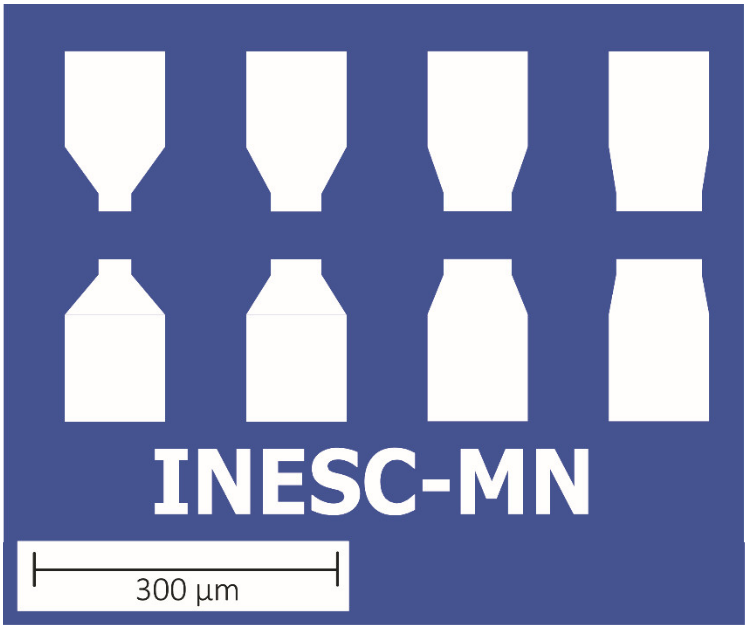

Process 7: Paths deposition

Date: __/__/____

Machine: Nordiko 7000

Sequence: **Metalization**

- **Module 2:** Soft sputtering Etch
- **Module 4:** AlSiCu (3000 Å) Deposition →
- **Module 3:** TiW(N) deposition

Some packaged structures, due to their thickness, might require thicker AlSiCu layers.

	Ar/N_2 flow (sccm)	Pressure (mTorr)	Power (kW)	Dep. Rate (Å/s)
Module 2	50/-	3	60/40	-
Module 4	50/-	3	2000	37.5
Module 3	50/10	3	500	1.25

Run #: ______

Read Values:

Module 2:

Module 4:

Module 3:

Process 8: Aluminum liftoff

Date: __/__/___

Machine: Wet bench

Steps:

- Resist strip with Microstrip 3001 at 65°C with ultrasounds;
- Clean with IPA (**isopropyl** alcohol) and water, and blow dry using compressed air gun.

Time needed to complete liftoff:_______________

Process 9: Contacts definition Date: __/__/____

Machines: **Vapor Prime > Track System (coating) > DWL > Track System (development)**

Steps:

- Vapor prime: program 0 – 5 min HMDS at 130°C;
- Track 1: program 6/2 – **coat** with 1.5 μm thick photoresist;
- DWL **exposure**;
- Track 2: program 6/2 – photoresist **development**;

Map: AMSION Mask: rv_ind_contact **X offset**: -400 μm **Y offset**: -186 μm

Energy: _____% Focus: _____

Photoresist structures expected after development:

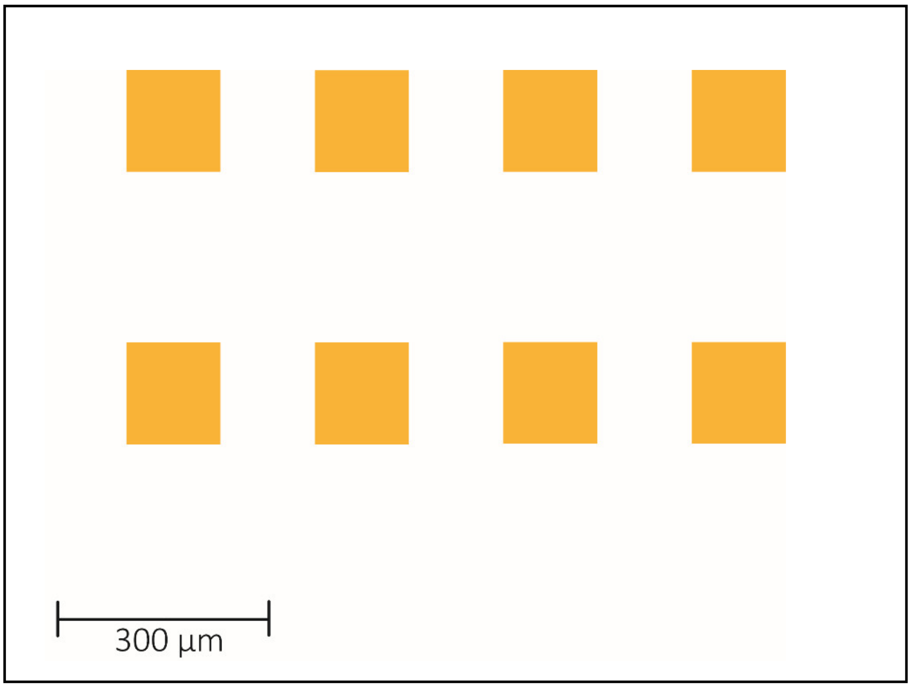

Process 10: Oxide (Al_2O_3) deposition

Date: __/__/____

Machine: UHV II

	Ar flow (sccm)	**Pressure (mTorr)**	**Power (W)**	**Dep. Rate (Å/s)**
UHV II	45	2.6	200	11

Etch Rate: 11 Å/s

Thickness: 2000 Å Total time: 182 min

Start time:________________

End time: ________________

Read Values:

Pressure before process:________

Pressure during process:________

Process 11: Oxide liftoff

Date: __/__/___

Machine: Wet bench

Steps:

- Resist strip with Microstrip 3001 at 65°C with ultrasounds;
- Clean with IPA (**isopropyl** alcohol) and water, and blow dry using compressed air gun.

Time needed to complete liftoff:________________
